The nitrogen vacancy center

in internal and external

fields

Von der Fakultät 8 Mathematik und Physik der Universität Stuttgart zur
Erlangung der Würde eines Doktors der Naturwissenschaften (Dr. rer. nat.)
genehmigte Abhandlung.

vorgelegt von

FLORIAN DOLDE

aus Nürtingen

Prof. Dr.   Jörg Wrachtrup,   Hauptberichter
Prof. Dr.   Harald Giessen,   Mitberichter
Prof. Dr.   Günter Wunner,   Prüfungsvorsitzender

Tag der mündlichen Prüfung:
18. Juli 2014

If no one comes from the future to stop you from doing it then how bad of a decision can it really be ...

Will Ferrell

Contents

Abbreviations

$\underline{X}$	vector X

$\vert 0, \pm \rangle$	electron spin eigenstates corresponding to $m_S = 0, \pm 1$
$\vert \uparrow, \downarrow \rangle$	nuclear spin eigenstates corresponding to $m_I = +1/2, -1/2$

γ_e	gyromagnetic ratio of the electron
μ_B	Bohr's magneton
g_e	electron g factor
$\hbar$	Planck's constant

NOT	NOT operation
ROT	ROT operation, spin rotation interchanging populations
CNOT	controlled NOT operation
CROT	spin rotation dependent on control spin state
PSWAP	partial SWAP gate interchanging the population between two qubit subspaces for one qutrit and one qubit
CPHASE	controlled phase operation, adding a phase dependent on the control

$\frac{\pi}{2}_{1+}$	$\frac{\pi}{2}$ pulse on the $\vert 0 \rangle \leftrightarrow \vert + \rangle$ transition on NV 1
π_{2-}	π pulse on the $\vert 0 \rangle \leftrightarrow \vert - \rangle$ transition on NV 2

FFT	fast Fourier transformation
ODMR	optical detected magnetic resonance
$NV^{0,-}$	nitrogen vacancy center in diamond, the charge states are indicated by $^{0,-}$ (i.e. neutral and negative charge states, without index, the negative charge state is attributed)
ZPL	zero phonon line

1. Zusammenfassung

Eine der größten Herausforderungen moderner Technologien im Bereich der Sensorik, der Informationsverarbeitung und der Kommunikation ist das Ausnutzen quantenmechanischer Effekte. Quantum-Metrologie ermöglicht beispielsweise sehr hohe Messgenauigkeiten, wobei das aktive Messvolumen einem einzelnen Atom entsprechen kann [1]. Aber auch bei größeren Sensoren können bzw. werden Quanteneffekte ausgenutzt, wie zum Beispiel bei Gravitationswellendetektoren (z.B. LIGO, VIRGO, GEO600 oder TAMA 300). Mit gequetschtem Licht kann das Signal-zu-Rausch-Verhältnis bei letzteren Anwendungen verbessert werden. Ein weiteres Anwendungsgebiet von Quantentechnologien ist die Computertechnik. Hierbei wird der kooperative Charakter von verschränkten Zuständen (z.B. Energieniveaus in Atomen, Polarisation von Photonen oder makroskopische Quantenzustände in supraleitenden Qubits) für die Informationsverarbeitung genutzt, um mit klassischen Computern nur schwer lösbare Probleme schneller und effizienter zu bewältigen [2, 3]. Daher sind Quantensysteme, sogenannte 'Qubits', der zentrale Aspekt dieser aufkommenden Quantentechnologie. Die Wechselwirkung dieser Qubits mit externen Einflüssen wie Temperatur, Magnetfelder oder elektrischer Felder kann dazu genutzt werden, Quantensensoren zu entwickeln, die es erlauben Felder mit atomarer Auflösung auszumessen. Die Wechselwirkung zweier Qubits ist von besonderem Interesse, da mit ihnen verschränkte Zustände erzeugt werden können. Diese sind die Schlüsselkomponenten für das kollektive Verhalten, welches sowohl für die Beschleunigung in der Quanteninformationsverarbeitung sowie für eine Skalierung der Messgenauigkeit mit der Sensorgröße jenseits des Standard-Quantum-Limits (SQL) verantwortlich ist.

Um Quantentechnologie jedoch nutzbar zu machen, müssen erst einige schwierige Herausforderungen überwunden werden. Bisherige Qubits, wie kalte Atome [4], Ionen [5] und Festkörpersysteme [6–10], funktionieren nur unter extremen Bedingungen wie niedrige Temperaturen und/oder im Vakuum [11]. Dies schließt eine breite Anwendung von Quantentechnologie weitestgehend aus. Jedoch haben erste Experimente mit dem Stickstoff-Fehlstellen-Zentrum im Diamant (NV-Zentrum) gezeigt, dass diese auch bei Raumtemperatur und Normaldruck als Qubits funktionieren und ein einzelner Elektronenspin ($S = 1$) optisch

ausgelesen werden kann (ODMR) [12]. Die herausragenden Eigenschaften des Elektronenspins des NVs mit Kohärenzzeiten in der Größenordnung mehrerer hundert Mikrosekunden [13] erlauben die Implementierung quantenmechanischer Sensoren sowie erste Schritte in Richtung eines Quantencomputers. Auch ihre minimale Größe (NV-Zentren wurden in Nanodiamanten mit weniger als 8 nm Durchmesser nachgewiesen [14]) ist ein bestechendes Argument für ein breites Anwendungsgebiet der NV-Quantenmetrologie. Deshalb werden in dieser Arbeit die Quantenanwendungen des Stickstofffehlstellenzentrums in Diamant (NV) eingehend untersucht.

Um das volle Potenzial der NV-Zentren nutzbar zu machen, müssen zuerst seine Kohärenzeigenschaften verstanden werden. Das für die Dekohärenz verantwortliche Störfeld wird in reinen Proben hauptsächlich durch das ^{13}C Kernspinbad erzeugt. ^{13}C hat einen Anteil von 1.1 % im natürlichen Isotopengemisch. Um die Kohärenzeigenschaften zu verbessern, muss der Einfluss dieses Störfeldes minimiert werden. Es wurde in vorangegangenen Arbeiten gezeigt, dass durch die synthetische Herstellung von isotopenreinen Diamanten Kohärenzzeiten auf der Millisekundenzeitskala erreicht werden können [15]. In dieser Arbeit wurde eine andere Strategie verfolgt. Durch die Nutzung dynamischer Entkopplungsprotokolle konnte die Wechselwirkung zwischen Spinbad und dem NV-Zentrum unterdrückt werden. Mit dem von Carr, Purcell, Meiboom und Gill entwickelte Multipulsprotokoll (CPMG) [16, 17] wurde eine Kohärenzzeit von $T_{2\,\text{CPMG}} = 2.44 \pm 0.44$ ms erreicht. Des Weiteren wurde mit Hilfe eines 'spinlocking' Experiments das Limit für Entkopplungsprotokolle bestimmt ($T_{1\rho} = 2.47_0.27$ ms). Da $T_{2\,\text{CPMG}}$ ungefähr denselben Wert hat wie $T_{1\rho}$, wurde somit der höchste Entkopplungsgrad vom Spinbad erreicht.

Entkopplungsprotokolle sind aber nicht die einzige Strategie, die Wechselwirkung mit dem Spinbad zu unterdrücken. Alternativ können auch die Eigenzustände des NV Elektronenspins so beeinflusst werden, dass das magnetische Dipolmoment des Elektronenspins verschwindet. Dies unterdrückt die Wechselwirkung zwischen NV und Spinbad in erster Ordnung und erlaubt somit längere Kohärenzzeiten. Die benötigten Eigenzustände können durch eine Mischung der Hochmagnetfeldeigenzustände zum Spinoperator S_z, $|\pm\rangle$, erzeugt werden. Diese Mischung der Eigenzustände wird durch geeignete Verspannungen im Kristallgitter oder elektrische Felder induziert. Für diese Eigenzustände reduzieren sich die Erwartungswerte von $\langle S_x \rangle$, $\langle S_y \rangle$ und $\langle S_z \rangle$ auf null. Durch das unterdrücken der Badwechselwirkung ist die inhomogene Linienbreite nicht mehr durch das Spinbad bestimmt ($T_2^* = 3.5 \pm 0.2$ μs), sondern durch die Suszeptibilität auf andere fluktuierende Größen wie Temperatur, elektrische Felder oder Phononen. Es wurde

eine freie Kohärenzzeit von $T_2^* = 32.4 \pm 3.6\ \mu$s gemessen, vergleichbar mit der in isotopenreinen Diamanten [15]. Da die Eigenzustände stark vom Magnetfeld beeinflusst werden, konnte ein Übergang zwischen dem verspannungsdominierten Bereich und dem magnetfelddominierten Bereich nachgewiesen werden.

Hat man die Dekohärenz durch das Kernspinbad unterdrückt, stellen die ^{13}C Kernspins eine potenzielle Ressource für Quanteninformationsverarbeitung dar. Die ^{13}C aus der nächsten Umgebung des NVs bilden ein kleines Quantenregister, das zum Beispiel den Einsatz von Fehlerkorrekturprotokollen erlaubt [18]. Um auch weiter entfernte, schwach koppelnde Kernspins zu identifizieren und somit auch für ein Quantenregister nutzbar zu machen, muss eine neue Spektroskopiemethode entwickelt werden. Hierfür wurde eine Korrelationsspektroskopie entwickelt, welche auf der Rotation des ^{13}C Kernspins in Abhängigkeit vom Elektronenspinzustand, basiert. Diese konditionelle Rotation wurde ausgenutzt, um Kernspin-Superpositionszustände zu erstellen. Nach einer freien Entwicklungszeit wurde deren Phase/Kohärenz mit einem auslesbaren Elektronenspinzustand korreliert und somit zugänglich gemacht. Die kohärente Entwicklung dieser Kernspinzustände ist nicht durch die Dekohärenz des Elektronenspins begrenzt (T_2, einige hundert Mikrosekunden). Lediglich Elektronenspinflips auf der Zeitskala einiger Millisekunden (T_1) können zu einer Dekohärenz der Kernspinzustände führen. Durch die verlängerte freie Entwicklungszeit der Kernspinzustände lässt sich deren Larmorfrequenz nun mit einer beispiellosen Präzision bestimmen und davon abgeleitet die Wechselwirkungsstärke mit dem Elektronenspin. Prinzipiell erlaubt die hier präsentierte Korrelationsspektroskopiemethode sogar die Bestimmung von dipolarer Kopplung zwischen zwei ^{13}C. Mit Hilfe des intrinsischen Kernspinspeichers (^{14}N) kann die Hyperfeinwechselwirkung an und ausgeschaltet werden. Dieses neu entwickelte Entkopplungsprotokoll hat somit das Potential die Auflösung noch über T_1 hinaus zu erhöhen. Dies würde erlauben, die Kopplungsstärke zwischen einzelnen ^{13}Cs auf eine Genauigkeit unter einem Herz zu bestimmen [19].

Ein Hauptanwendungsgebiet von NV Zentren in Diamanten ist die hochsensitive Messtechnik. Äußere Einflüsse, wie zum Beispiel magnetische [20] und elektrische [21] Felder oder die Temperatur [22], können präzise nachgewiesen werden. Für jeden dieser speziellen Fälle kann der Spin-Hamilton-Operator derart maßgeschneidert werden, dass er sensitiv auf die jeweilige physikalische Größe wird. Diese Suszeptibilitäten können genutzt werden, um hochpräzise quantenmechanische Sensoren zu entwickeln. Im Allgemeinen werden Felder oder Wechselwirkungen durch eine kohärente Entwicklung eines Quantzustands gemessen. Während der Zeit τ sammelt der Zustand eine Phase auf. Aus Phase und Zeit lässt sich

die Larmor-Frequenz bestimmen, welche am Ende abhängig von der jeweiligen zu messenden physikalischen Größe ist. Die höchste Senistivität η erreicht man für die längst mögliche Zeit τ ($\eta \propto \sqrt{\tau}$). Da letztere im Allgemeinen durch die jeweilige Kohärenzlebensdauer beschränkt ist, lohnt es sich die Kohärenzzeit durch Entkopplungsprotokolle zu verlängern.

In dieser Dissertation wurde das etablierte Magnetometrieprotokoll [20, 23] durch die Benutzung der CPMG Entkopplungssequenz verbessert. Dadurch konnte eine Verbesserung der Sensitivität gegenüber dem Hahn-Echo-basierten Protokoll mit $\eta_{\text{Hahn}} = 19.4 \pm 0.4 \frac{nT}{\sqrt{Hz}}$ auf $\eta_{\text{CPMG}} = 11.0 \pm 0.2 \frac{nT}{\sqrt{Hz}}$ erreicht werden. Das heißt, für eine Messzeit von 1 s beträgt die Messungenauigkeit ca. 11 nT.

Das aus den Magnetometrie-Experimenten gewonnene Verständnis wurde dann angewandt, um mit dem linearen Stark-Effekt des Grundzustandes [21] elektrische Felder zu messen. Um eine ausreichende Kopplungsstärke zwischen elektrischen Feldern und NV zu erreichen, müssen die Eigenzustände des NVs genau kontrolliert werden. Dafür ist das präzise Ausrichten des Magnetfeldes sehr wichtig. Eine Messgenauigkeit von $\eta_{\text{FID}} = 631.1 \pm 15.1 \frac{V}{cm\sqrt{Hz}}$ für statistische E-Felder (DC) und $\eta_{\text{Hahn}} = 142.6 \pm 3.6 \frac{V}{cm\sqrt{Hz}}$ für fluktuierende E-Felder (AC) konnte nachgewiesen werden. Das entspricht dem Nachweis einer Elementarladung in einem Abstand von 150 nm in einer Sekunde Messzeit. Der Einfluss des elektrischen Feldes auf die Spinzustände kann durch die Rotation eines waagrechten Magnetfeldes moduliert werden. In Kombination mit dem Wissen um die Orientierung des NV Zentrums im Diamantkristall ist es somit möglich den kompletten E-Feld Vektor zu bestimmen. Da in unserem Fall aber nur die Ausrichtung und nicht die Orientierung des NV Zentrums bekannt war, konnte die E-Feldorientierung nur bis auf eine Periodizität von 180° bestimmt werden.

Des Weiteren wurde die entwickelte Vektorelektrometrie angewendet, um das elektrische Feld einer einzelnen Elementarladung nachzuweisen. Hierbei wurden zwei nah beieinander liegende NV-Zentren benutzt, um einen kontrollierbaren Ladungsträger in der Nähe des Sensor-NVs zu positionieren. Der Ladungszustand eines NVs wird dabei durch Photoionisation kontrolliert, während das andere als Sensor den Wechsel des Ladungszustands aufzeichnet. Zusätzlich wurde ein magnetisches Feld ($B_\perp \approx 5.53$ mT) orthogonal zur NV Achse angelegt, um die Spinzustände sensitiv auf elektrische Felder zu machen und andere Einflüsse zu unterdrücken. Dabei wurde eine Verschiebung der Eigenenergien durch die unterschiedlichen Ladungszustände von $\nu_{\text{Stark}} = 66 \pm 7$ kHz gemessen. Mit Rotation des orthogonalen Magnetfeldes konnte die E-Feld Richtung, aber nicht dessen Orientierung, bestimmt werden.

Ein weiteres Anwendungsgebiet des NV-Zentrums liegt in der

Quanteninformationsverarbeitung. Das NV-Zentrum ist eines der wenigen Festkörpersysteme, das kohärent manipuliert werden kann [24], während es über starke Kopplung zu anderen Qubits verfügt. Deswegen ist es ein guter Kandidat für den fundamentalen Baustein eines Quantenregisters. Di Vincenzo postulierte in 2000 die fünf nötigen Kriterien für eine Quantencomputer [25]: (i) ein gut definiertes Qubit, (ii) Initialisierbarkeit, (iii) lange Kohärenzzeiten, (iv) ein 'universelles' Set von Quantengattern und (v) individuelle Auslesbarkeit.

Das Qubit (ein eindeutig definiertes Zweiniveausystem, das kohärent manipuliert werden kann) wird für das NV normalerweise im elektronischen Grundzustand definiert. Da das NV ein $S = 1$ System ist, kann das Qubit frei in den drei Energieniveaus des Grundzustandes zugeordnet werden. Die Initialisierungsgenauigkeit ist ≈ 0.972 [18], die Kohärenzzeiten sind auf der Größenordnung von Millisekunden [15], während kohärente Kontrolle bis in das Gigaherzregime möglich ist [26]. Ein 'universelles' Set an Quantengattern wird durch die individuelle Adressierung der NV Übergänge mit Mikrowellen möglich. Konditionelle Quantengatter, z.B. zwischen einem NV und einem Kernspin, werden durch ein schwaches Mikrowellenfeld realisiert, das die Hyperfeinwechselwirkung auflösen kann [27]. Individuelles Auslesen der Spins kann entweder durch 'single shot read out' der Kernspins bei Raumtemperatur [28] oder des Elektronenspins bei tiefen Temperaturen [29] realisiert werden. In den letzten Jahren gab es erste Demonstrationen von kleinen Quantenregistern mit dem NV und seinen umgebenden Kernspins [30, 31]. Selbst erste Quantenalgorithmen wurden implementiert [18, 32]. In dieser Arbeit wurde eine mögliche Skalierung des Quantenregisters demonstriert, da bisher das NV als Zentralspin nur mit ungefähr zehn Kernspins kontrollierbar individuell wechselwirken kann [18].

In den letzten Jahren gab es eine Vielzahl von Vorschlägen, wie man zwei NV Zentren kohärent koppeln kann, um ein voll funktionsfähiges Quantenregister zu erschaffen [33, 34]. Vor kurzem wurde der erste verschränkte Zustand zwischen zwei entfernten NV Zentren mit Hilfe von Messungen an verschränkten Photonen durchgeführt [35]. Hier war aber die Erfolgsrate in der Größenordnung von einem Ereignis in mehreren Minuten. In dieser Dissertation wurde die deterministische Herstellung eines verschränkten Zustands zwischen zwei NV Zentren untersucht. Hierfür wurde ein Protokoll, basierende auf dipolarer Kopplung und Entkopplungsprotokollen, entwickelt, um kohärente Wechselwirkungen zwischen zwei NV Zentren zu ermöglichen. Dies erlaubt auch eine starke Kopplung für $\frac{1}{\nu_{\text{dip}}} \approx T_2$ im Gegensatz zu $\frac{1}{\nu_{\text{dip}}} \approx T_2^*$. Da T_2 normalerweise zwei Größenordnungen größer als T_2^* ist, erlaubt dies einen größeren Abstand zwischen den NV Zentren. Trotzdem ist das Herstellen eines NV Paars mit dem nötigen kleine Abstand

für kohärente Wechselwirkung (weniger als $\approx$ 30 nm) eine nichttriviale Aufgabe. Um Produktionswahrscheinlichkeiten in einem vertretbaren Rahmen zu erreichen, wurde eine neue Implantationsmethode basierenden auf Nanokanälen in einer Glimmermaske entwickelt. Mit dieser kann eine Implantationseffizienz von bis zu 14% erreicht werden (1.97% für die Implantationsparameter in die in dieser Arbeit). Eine dipolare Kopplung von $\nu_{\text{dip}} = 4.93 \pm 0.05$ kHz konnte nachgewiesen werden. Mit der Hilfe von Doppelquantenkohärenzen (eine Kohärenz zwischen $|+\rangle$ und $|-\rangle$) wurde ein Verschränkter Zustand zwischen den beiden NV Zentren hergestellt. Eine Tomographie, basierend auf ROT Gattern und kohärenten Zeitentwicklungen, ergab eine Zustandsgenauigkeit von $F_{\text{stand}} = 0.67 \pm 0.04$. Ein alternatives Tomographiekonzept basierend auf Zweiphotonenereignissen wurde entwickelt. Die vom Elektronenspin abhängige Eigenbasis des ^{15}N Kernspins erlaubt die kohärente Manipulation des Kernspins allein durch geeignete Kontrolle des Elektronenspins. Mit Hilfe eines PSWAP Gatters konnte die Verschränkung des Elektronenspins auf dem Kernspin gespeichert werden (mit einer Effizienz von $Eff_{\text{stand}} = 0.39 \pm 0.01$). Eine Kohärenzzeit des gespeicherten Zustandes von $T_{\text{stor}} = 1.03 \pm 0.23$ ms konnte nachgewiesen werden. Diese ist nur durch die Lebenszeit des Elektronzustandes ($T_1 = 1.12 \pm 0.26$ ms) limitiert. Da die Wechselwirkung zwischen den Kernspins in der Größenordnung einiger Hertz lag und damit weit unterhalb der Dekohärenzrate, aber das Herstellen und Speichern der Verschränkung nur ein paar zehn Mikrosekunden dauerte, wurde somit zwischen zwei nicht wechselwirkenden Kernspins ein verschränkter Zustand erzeugt.

Bei dem Grad der erzeugten Verschränkung der Elektronenspins sowie der Kernspins ergab sich eine erhebliche Diskrepanz zwischen dem theoretisch möglichen ($F_{\text{theo}} = 0.849$) und dem experimentell realisierten Zustand. Als Hauptfehlerquelle erwiesen sich ungeeignete, konventionelle Mikrowellenpulse und Pulssequenzen zur Spinkontrolle. Allein durch die Hyperfeinwechselwirkung zwischen ^{15}N und dem Elektronenspin hatte bereits ein konventionelles ROT nur eine Genauigkeit von ungefähr 0.94. Das lässt sich durch eine nichtverschwindende Verstimmung der Spinübergänge gegenüber der Mikrowellenfrequenz erklären. Weitere negative Effekte treten auf, wenn Spinübergänge in spektraler Nähe ungewollt leicht angeregt werden (Nebensignaleffekte). Um wieder die volle Kontrollgenauigkeit herzustellen, wurden die Mikrowellenpulse mit dem GRAPE Algorithmus [36] numerisch optimiert. Hier werden, an Stelle von Rechteckpulsen (die Mikrowelle wird auf einen konstanten Wert angeschaltet und später wieder ausgeschaltet), die Mikrowellenpulse in kleinere Segmente mit unterschiedlichen Phasen und Amplituden unterteilt. Letztere Parameter werden dann für jedes Segment numerisch optimiert um Fehler durch die Verstimmung der Mikrowellenfrequenz

sowie Nebensignaleffekte auf anderen Spinübergänge zu unterdrücken. Mit diesen optimalen Kontrollpulsen konnte ein ROT mit einer Genauigkeit größer als 0.99 implementiert werden. Die Verschränkungssequenz konnte so auf eine Genauigkeit von $F_{\text{opt}} = 0.824 \pm 0.015$ verbessert werden, womit sie nur noch durch die Kohärenzzeiten und den Polarisationsgrad der Elektronenspins limitiert ist. Die größte Verbesserung konnte aber im Speichern des Kernspins realisiert werden. Hier wurde die Effizienz von $Eff_{\text{stand}} = 0.39 \pm 0.01$ auf $Eff_{\text{opt}} = 0.92 \pm 0.07$ erhöht. Dies erlaubt die Erzeugung eines verschränkten Zustand auf den Kernspin mit einer Genauigkeit von $F_{\text{opt nulear}} = 0.819$. Die hier demonstrierte Kontrollgenauigkeit ist nicht nur elementar für Quantumtechnologie basierend auf dem NV Zentrum, sondern kann als Lösungskonzept auch auf alle anderen auf Spin basierenden Quantensysteme übertragen werden.

2. Summary

Harnessing quantum mechanical properties is one of the key challenges in modern technology. E.g. for quantum metrology, the use of quantum mechanical evolutions yields unprecedented sensitivities with an active sensor volume corresponding to one atom [1]. With the use of large entangled or squeezed states, the cooperative behavior of ensembles can enhance the sensitivity even further [37, 38]. Not only will metrology applications benefit from quantum technology, but also computer sciences will. In the near future a new field of quantum computation will emerge, where the cooperative nature of entangled states will be used to speed up computationally hard problems [2, 3].

Therefore single quantum systems, so called 'qubits', are at the heart of these emerging quantum technologies. The study of the interaction of qubits with external influences such as temperature, magnetic and electric fields can be utilized to build the ultimate sensors on the nanoscale. Interaction between two qubits is of particular interest, since they can be used to create so called '*entangled states*', whose quantum mechanical correlations are the key ingredient for speedup in quantum information processing and sub-shotnoise scaling of measurement sensitivity.

In this work, quantum applications of the nitrogen vacancy center in diamond (NV) are investigated. The NV center is an outstanding quantum system allowing for optical read out of a single electron spin ($S = 1$) at ambient conditions (ODMR) [12]. The exceptional spin properties with hundreds of microseconds of coherence time [13] pave the way for highly sensitive quantum sensors and increased computational power.

In order to understand the interaction with noise fields limiting coherence and ultimately extending the coherence times, the interaction of the NV with a spin bath is investigated. For pure grown diamond as provided by Element six (electronic grade >5 ppb nitrogen [39]), the coherence times are limited by the interaction with the ^{13}C spin bath. Breakthrough experiments with an isotopically purified diamond (^{13}C content 0.3%) allows to diminish the spin bath and as a consequence to reach coherence times in the millisecond regime [15]. Here, instead of using a purified diamond, a sample with natural ^{13}C abundance was investigated. With dynamical decoupling, noise from the spin bath was suppressed. With a multipulse sequence

developed by Carr, Purcell, Meiboom and Gill (CPMG) [16, 17], a coherence time of $T_{2\,\mathrm{CPMG}} = 2.44 \pm 0.44$ ms was realized. A spin locking experiment [40] was used to determine the limit for dynamical decoupling sequences $T_{1\rho} = 2.47 \pm 0.27$ ms. Since $T_{2\,\mathrm{CPMG}}$ is approximately identical with $T_{1\rho}$, the highest degree of decoupling from the spin bath was realized.

Dynamical decoupling is not the only choice to suppress the interaction with the spin bath. Alternatively, tailoring of the eigenstates to have a vanishing magnetic momentum, suppresses the interaction with any magnetic field in the first order. This eigenstate tailoring can be achieved by a strain field, which mixes the high axial magnetic field eigenstates $|\pm\rangle$ (eigenstates of S_z) to be linear combinations, thereby decreasing the expectation value of $\langle S_z \rangle$ to zero. With no magnetic field interaction, the inhomogeneous linewidth does not depend on the spin bath ($T_2^* = 3.5 \pm 0.2$ μs), but on other field fluctuations such as phonons or temperature. The free evolution coherence time $T_2^* = 32.4 \pm 3.6$ μs is then comparable to values obtained in isotopically purified diamonds [15]. Since the eigenstates are strongly dependent on the dominant interaction, a transition in coherence times between the strain dominated and magnetic field dominated regime was observed.

However, the ^{13}C spin bath is not only a nuisance, but also a potential resource for quantum information processing, forming a small quantum register around an electron spin allowing for example the implementation of quantum error correction protocols [18]. Spectroscopy of the spin bath at room temperature is challenging, since the ^{13}C spin bath being in its thermal state, yields no polarization. Therefore to probe the ^{13}C spins, we developed a new correlation spectroscopy method. Here a conditional rotation of the ^{13}C spins with regard to the NV electron spin state can be used to create coherence correlated with the electron spin populations even without prior polarization of the spin bath. After evolving freely, the ^{13}C coherences can be mapped back into an observable electron spin population by reapplying the correlation sequence. Since the free evolution of the nuclear spin coherences, electron spin coherences are not relevant, the observed correlation signal decays with the electron spin relaxation time T_1. This allows one to spectroscopically resolve the hyperfine coupling between the surrounding ^{13}C and the central NV center with unprecedented resolution. Such an improved resolution can be the basis for the characterization of larger quantum registers (e.g. those needed for quantum error correction [18]). In principle, the correlation spectroscopy method allows for the resolution capable of resolving the dipolar coupling between two ^{13}C in two dimensional spectroscopy experiments. Using the NV intrinsic nuclear spin memory (^{14}N), the hyperfine interaction between ^{13}C and NV center can be switched. This in turn allows the implementation decoupling schemes with spectral resolutions beyond

the T_1 limit.

The interaction of the NV center with external influences such as temperature [22], magnetic [20] and electric fields [21] can be exploited to create high sensitivity quantum metrology devices. Here the changes of the eigenenergies with applied fields is used for detection. In order to achieve higher sensitivities η, fields are detected using a coherent evolution for a time τ, with a frequency reference given by the microwave used for spin manipulation. Thus, sensing can be combined with dynamical coupling. Since η is proportional to $\sqrt{\tau}$, an increase in the coherence time enables an increased sensitivity. In this work, we extended the established AC magnetometry protocol [20, 23] by using the CPMG sequence. We were able to demonstrate an improvement in sensitivity from a Hahn echo based sensing scheme with $\eta_{\mathrm{Hahn}} = 19.4 \pm 0.4 \frac{nT}{\sqrt{Hz}}$ to $\eta_{\mathrm{CPMG}} = 11.0 \pm 0.2 \frac{nT}{\sqrt{Hz}}$.

The knowledge gained in the magnetometry experiments was then applied to exploit the linear Stark effect of the NV center [21] for electric field measurements. In order to have sufficient coupling of electric fields to the NV centers, their eigenstates have to be tailored carefully. These eigenstates are a mixture of the high axial magnetic field eigenstates $|\pm\rangle$, which are only mixed as long as the electric field interaction is larger than the axial magnetic field interaction (strain can be treated as an electric field [41]). Therefore a careful alignment to suppress axial magnetic fields is necessary. A sensitivity η for the static electric field of $\eta_{\mathrm{FID}} = 631.1 \pm 15.1 \frac{\mathrm{V}}{\mathrm{cm}\sqrt{\mathrm{Hz}}}$ and $\eta_{\mathrm{Hahn}} = 142.6 \pm 3.6 \frac{\mathrm{V}}{\mathrm{cm}\sqrt{\mathrm{Hz}}}$ for fluctuating fields were demonstrated. This relates to the sensing of the electric field of one fundamental charge at a distance of 150 nm in about one second of average. With the application of nonaxial magnetic fields larger than the electric fields, the eigenstates become dependent on the magnetic field orientation with respect to the carbon bonds (ϕ_B), yielding an intrinsic coordinate system. This leads to an oscillatory behavior of orthogonal electric field interaction depending on its angle with respect to a carbon bond (ϕ_E) and the magnetic field orientation, which is proportional to $\cos(2\phi_B + \phi_E)$. Combined with the knowledge of the NV orientation, this allows one to determine the perpendicular electric field vector. However, since only the orientation of the magnetic field towards the crystal lattice was known, the electric field vector could only be determined up to a 180° rotational symmetry.

Using the developed vector electric field sensing technique, the electric field of a single fundamental charge in the diamond lattice was measured [42]. In order to have a controllable charge, a pair of NV centers was utilized. The charge state of one NV center was controlled using a red pumping laser while the other was used to measure the changes in the respective electric field due to charge state dynamics. In order to compensate for the axial magnetic field induced by hyperfine interaction

with the ^{15}N nuclei of the NV center, a perpendicular magnetic field was applied ($B_\perp \approx 5.53$ mT). The observed shift in eigenenergies due to the different charges was $\nu_{\text{Stark}} = 66 \pm 7$ kHz. With the rotation of $B_\perp$ the electric field vector could be determined up to a twofold symmetry.

However, the NV center is not only a prime candidate for quantum metrology, it also has a promising future in quantum information processing. The NV center is one of a few solid state systems, that can be coherently manipulated [24] while providing strong interqubit coupling. Hence it is a good candidate as a fundamental building block for quantum registers. Di Vincenzo postulated in 2000 the five necessary criteria a quantum device has to fulfill in order to build a large scale quantum computer [25]: (i) a well-defined qubit,(ii) initialization,(iii) long coherence times,(iv) a "'universal"' set of quantum gates and (v) individual read out. The qubit (a well-defined two level system which can be coherently manipulated) for the NV is defined in the spin ground state. A qubit is the quantum information processing analog of the classical bit, containing the information used for computation. Since the NV is a spin one system ($S = 1$), one can freely choose a subspace of the triplet to define the qubit, e.g. $|0\rangle$ and $|+\rangle$. The initialization fidelity of the NV is about ≈ 0.972 [18], coherence times are in the millisecond regime either by isotopic engineering [15] or by dynamical decoupling, while coherent control is possible up to the gigahertz regime [26]. A 'universal' set of quantum gates is realized by driving the microwave transitions of the NV. Conditional gates can be realized by weak driving, allowing one to spectrally resolve the hyperfine spectrum with surrounding nuclear spin qubits [27]. Individual spin read out can be either realized by single shot read out of nuclear spins [28] at room temperature or by single shot read out of the electron spin at low temperatures [29]. First demonstrations of a quantum register with the NV center as a central spin and surrounding nuclear spins (^{13}C) have been demonstrated just recently [30, 31]. Even first quantum algorithms were implemented [32], such as quantum error correction [18]. However, what is missing is a road map to scale theses quantum registers, since the central spin approach is limited to about ten nuclear spins [18].

There have been various proposals in the last years about how to couple two NV centers to allow for a fully scalable quantum register [33, 34]. Recently, the first remote entangled state using a heralded measurement of photons entangled to two NV centers was demonstrated [35]. However the event rate was in the order of five minutes, making a deterministic entanglement generation in the normal time frame of information processing (MHz to GHz) challenging. In this dissertation, the deterministic on demand creation of an entangled state between two NV centers was investigated. In order to facilitate coherent interaction between the two NV

centers, a scheme based on dipolar interaction with strength ν_{dip} and dynamical decoupling was developed (allowing for strong coupling also for $\frac{1}{\nu_{\text{dip}}} \approx T_2$ and not $\frac{1}{\nu_{\text{dip}}} \approx T_2^*$, as for using conditional rotations). Since T_2 is in general about two orders of magnitude larger than T_2^*, this allows for a larger distance between the two NV centers. However, creating a pair of NV centers at a distance required for coherent interaction (less then ≈ 30 nm) is a nontrivial task. In order to gain a sufficient success rate from the nitrogen implantation sites [43], a masked implantation method based on nano-channels in a mica sheet was developed. In doing so, an increase in efficiency up to 14% per individual implantation site (1.97% in this work) is possible. An NV pair was identified with a dipolar coupling of $\nu_{\text{dip}} = 4.93 \pm 0.05$ kHz.

With the usage of double quantum coherences (a coherence between $|+\rangle$ and $|-\rangle$), an entangled state between the two NV centers was created. A tomography measurement, based on ROT gates and coherent evolutions, yielded a fidelity of $F_{\text{stand}} = 0.67 \pm 0.04$. An alternative tomography concept using two photon correlations was developed. The electron spin state dependent eigenframe of the ^{15}N nuclei enabled a conditional coherent manipulation of the nuclear spin, using the $|0\rangle$ state as an ancilla level facilitating the nuclear spin rotation. This allowed us to use a partial swap gate (PSWAP interchanging $|\pm\rangle$ and $|\uparrow\downarrow\rangle$). With the PSWAP gate, the electron spin entanglement could be stored in the intrinsic nuclear spin memory (^{15}N, storage efficiency $Eff_{\text{stand}} = 0.39 \pm 0.01$). A storage time of $T_{\text{stor}} = 1.03 \pm 0.23$ ms, limited by the spin lifetime of the electron spin ($T_1 = 1.12 \pm 0.26$ ms), was measured. Note that the interaction between the nuclear spins is in the order of a few Hertz. Since the nuclear spins do not interact in the time frame of one measurement run, we have demonstrated a successful implementation of an electron spin bus allowing to entangle remote (non-interacting) nuclear spin registers.

Unfortunately, the fidelity of the entanglement generation yielded a discrepancy to the theoretically possible value of $F_{\text{theo}} = 0.849$, limited by the coherence times and the electron spin polarization. After further investigation it became clear that the entanglement performance was greatly reduced by a lack of control fidelity. Due to the hyperfine interaction with the ^{15}N nuclei, a simple ROT gate only has a fidelity of about 0.94 with given limitations to the microwave power. In order to achieve a high control fidelity, pulse shape engineering based on the GRAPE algorithm [36] was implemented. Here, instead of applying a square microwave pulse, the pulse is split into segments with different amplitudes and phases. The segments are then numerically optimized to compensate for detuning errors due to the hyperfine interaction as well as cross talk to other NV transitions. With these optimal control pulses, a ROT fidelity larger than 0.99 was achieved. The entanglement sequence could be improved to a fidelity of $F_{\text{opt}} = 0.824 \pm 0.015$, basically being limited by

polarization and coherence times. However, the most significant improvement could be demonstrated for entanglement storage, improving the PSWAP fidelity to yield a storage efficiency of $Eff_{\text{opt}} = 0.92 \pm 0.07$. This allows for meaningful entanglement of the nuclear spins with a fidelity of $F_{\text{opt nulear}} = 0.819$. High fidelity control even in a dense control environment is a challenging task not only for NV based quantum information processing. Every candidate relying on the spectral separability to address single qubits will have to solve this issue. Therefore, the presented work can be used as a blueprint to solve control issues in other systems.

3. Introduction

Quantum technology is on the verge of affecting our everyday lives. Quantum devices have the potential to outperform classic devices in terms of computational power or sensitivity. The promise of more computational power is based on a new class of computational operations that exploits the quantum property entanglement. An entangled state is a collective state of multiple nodes, so called qubits, which contain the information. Due to the collective coherence in an entangled state, correlated operations can be carried out in one single operation on the whole register, whereas in a classical device, each single data entry would have to be correlated to each other. This allows for a tremendous speed up in scaling, allowing for example prime factorization of numbers in polynomial time, while classical devices are believed to have exponential scaling [2]. Not only computational operations will benefit from harnessing quantum entanglement. In recent years, there has been a tremendous effort to exploit quantum correlations for high resolution metrology. With the smallest sensor volume conceivable (the size of one atom), unprecedented sensitivities per sensor volume are obtainable [1]. The use of entangled or squeezed states promise a sensitivity scaling with the sensor size beyond the shot noise limit ($\eta \propto \sqrt{N}$) with the so-called Heisenberg scaling ($\eta \propto N$).

However, despite quantum technology's promise of unprecedented computational power and sensitivity, quantum technology has yet to overcome some difficult challenges. In particular, thus far, extreme conditions like low temperatures and/or vacuum are necessary to have control of quantum effects and to harness its full potential. Especially for metrology applications, this limits the possible applications severely. Yet, first evidence suggests that the NV center in diamond might be a possible solution to this problem. With the possibility of single spin optical read out at room temperature and a size in the same order as a single atom it is a prime candidate for both improving computational power and sensitivity in quantum metrology. In this dissertation, the greater challenge of implementing quantum technology under ambient conditions is addressed by improving the NV's coherence properties, expanding the NV sensor applications to electric fields and creating a scalable quantum register in node size as well as control.

With its long spin coherence at ambient conditions it allows for unprecedented

sensitivities for metrology applications [20, 23]. This has been shown to allow for the detection of few nuclear spin [44] or a single electron spins [45]. Even the detection of a few silicon nuclear spins was possible [46], opening the new field of nanoscale MRI. With diamonds as small as 8 nm [14] and low cytotoxicity [47], quantum metrology even in biological environments like cells are feasible [48, 49]. So far, the Zeeman interaction and the temperature dependence of the NVs zero-field splitting [22] were exploited for quantum metrology. In this work, we extended the measurement capabilities to electric fields. In order to harness the Stark shift of the ground state, the eigenstates of the NV center have to be tailored by reducing any axial magnetic field to zero. The complex nature of the electric field interaction, does not, like for magnetometry, only allow the sensing of a magnetic field in one direction, but the full electric field vector can be measured using one NV center and rotating an orthogonal magnetic field. The demonstrated electric field sensitivity allows for the detection of a single fundamental charge at ambient conditions.

The developed electric field sensing scheme was then employed to detect the electric field from a single fundamental charge in a diamond matrix at ambient conditions. Since the electric field effect was about one order of magnitude larger than the magnetic dipolar coupling, it seems possible to use electric field sensing similar to nanoscale MRI to investigate the electric field environment in a scanning probe configuration.

But not only for quantum metrology, is the NV center a prime candidate. It is so far the most advanced system allowing for the implementation of quantum information processing at ambient conditions. There have been demonstrations of quantum nodes based on a central spin architecture, with the NV as the central spin coupled to a small register of bath spins in the surrounding [30, 31]. Even more advanced algorithms like quantum error corrections have been demonstrated [18]. Since these quantum nodes make the perfect building block for a large scale quantum register, we derived a spectroscopy method beyond the limitations given by the coherence times of the NV center to identify the coupling constants of surrounding nuclear spins. This paves the way to implement a small quantum register for every NV. However, when using this central spin architecture, the possible register size is limited making the register not scalable. Therefore we implemented a spin bus between two quantum nodes by dipolar coupling. This enables us to create an entangled state between two NV centers. To the knowledge of the author, this is the first demonstration of electron spin entanglement at ambient conditions. The entangled state was then stored on the intrinsic nuclear spin memory (nitrogen), creating a remote entangled state, where the interaction between the two qubits is orders of magnitude smaller than the time necessary to create the entanglement. With storing the entanglement

on the nuclear spins, entanglement lifetimes in the orders of milliseconds could be demonstrated.

Not only scalability is one of the key milestones towards a fully scalable quantum register, the control of the single quantum nodes also has to be precise. Since our quantum nodes are electron and nuclear spins addressed by microwave and radio-frequency radiation, the control fidelity so far was only about 0.95, not sufficient for more elaborate quantum algorithms. To reclaim the full potential of the NV center, optimal control pulses based on the GRAPE algorithm were implemented, allowing for control fidelities larger than 0.99. These pulses were then used to create entangled state fidelities and storage efficiencies limited only by the coherence times of the electron spin.

4. Introduction to the NV center in diamond

The Nitrogen Vacancy center (NV) in diamond, a molecular point defect with C_{3V} symmetry, consists of a nitrogen atom at a carbon lattice site and an adjacent carbon vacancy (see Fig. 4.1). Diamond has a fcc lattice with two carbons in its unit cell. The NV is orientated along the $\langle 111 \rangle$ axis giving 8 possible NV orientations (see A.7) So far, two charge states of the NV center have been observed [42, 50], a negative charge state with an electron spin of $S = 1$ and a neutral charge state ($S = \frac{1}{2}$). NV^- and NV^0 can be optically distinguished by their ZPLs (zero phonon line) at 637 nm and 575 nm, respectively, which are each accompanied by broad (~ 100 nm) phonon sidebands [51] (see
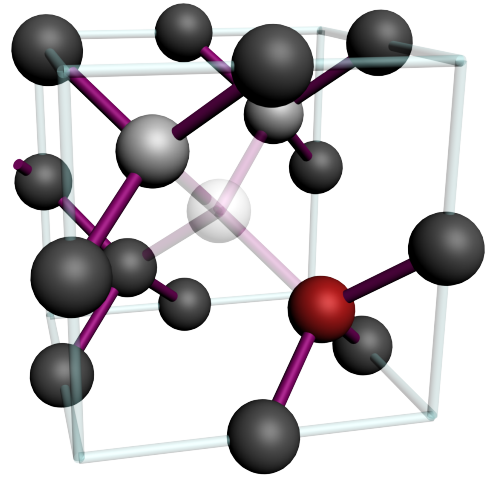
Figure 4.1.: NV center in diamond lattice The red sphere represents the nitrogen, while the translucent sphere represents the vacancy.

Fig. 4.4 and Chapter 4.2). For NV^-, optically detected magnetic resonance (ODMR) has been observed for single centers [12]. The NV energy levels are located in the band gap of the diamond semiconductor (band gap ≈ 5.5 eV). Since diamond has a very rigid lattice, almost all phonons are frozen out at room temperature (Debye temperature = 1860 K, no anti-Stokes band in Fig. 4.4), coherent spin manipulation as well as long coherence times at ambient conditions are possible. This effect is further enhanced by the weak spin-orbit coupling typical for carbon structures.

Due to the C_{3V} symmetry and the fact that the electron wave functions are highly localized at the defect site [52–54] molecular orbitals can be attributed to NV^- center making it an effective molecule in a solid state matrix. The electronic levels of the NV center are a $^3A_2$ ground state, a ^3E exited state and two metastable shelving states ^1A and ^1E (see Fig. 4.2). Ground (GS) and exited state (ES) are split by spin interaction into a triplet. The degeneracy of the ground and exited state triplet is lifted by a zero field splitting (GS: $D = 2.87$ GHz, ES: $D = 1.42$ GHz [55]). The

eigenstates of the triplet are normally given by the eigenstates of the S_z operator and are $m_S = 0, \pm 1$, denoted as $|0\rangle, |\pm\rangle$. There is an inter-system crossing (ISC) between the exited ^{3}E exited state and the ^{1}A shelving state. The ISC rates are strongly dependent on the spin state, leading to a difference in exited state life time ($\tau_{|0\rangle} = 23$ ns and $\tau_{|\pm\rangle} = 12.7$ ns[55]). The shelving states have an infrared emission band at 1046 nm. They decay to the ^{3}A ground state again via ISC with a life time of about 300 ns [56].
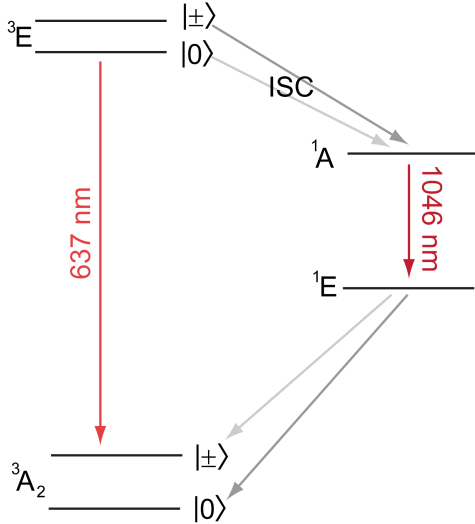
Figure 4.2.: NV$^-$ schematic The triplet ground ^{3}A$_2$ state and the exited ^{3}E state are split by the zerofield splitting ($D_{^3\text{A}_2}$=2.87 GHz, $D_{^3\text{E}}$=1.43 GHz). The intersystem-crossing (ISC) rates between ^{3}E and ^{1}A are strongly spin dependent allowing for spin polarization and read out.

A cycle through the metastable state is not spin conserving, flipping the the spin $|\pm\rangle \leftrightarrow |0\rangle$. Due to the higher ISC rate for the $|\pm\rangle$ states, the NV center is polarized into the $|0\rangle$ under illumination [57]. The long life time of the shelving state is also exploited for optical spin read out (see Chapter 4.1).

For this work, the ground state triplet was used. Its effective spin Hamiltonian is given by

$$H_{\text{NV}} = DS_z^2 + \gamma_e \underline{B}\,\underline{S} \tag{4.1}$$

where $D = 2.87$ GHz is the zerofield splitting, $\gamma_e = 28.8\ \frac{\text{GHz}}{\text{T}}$ is the electrons gyromagnetic ratio (a factor of 2π is omitted for convenience), $\underline{B}$ the magnetic field vector and $\underline{S}$ the electron spin operators. Please note, that values given in the Hamiltonian are in frequency throughout this work.

Nitrogen supplies a long lived nuclear spin, which forms an intrinsic quantum memory with a phase memory time governed by the electron spin relaxation time [30, 31, 58]. There are two stable nitrogen isotopes, the most abundant one being ^{14}N (99.6% natural abundance). ^{14}N has a nuclear spin of $I = 1$, giving the following extension to the Hamiltonian:

$$H_{\text{hf }^{14}\text{N}+\text{N}_{\text{Zeeman}}} = a_\parallel S_z I_z + a_\perp \left(S_x I_x + S_y I_y\right) + PI_z^2 - \gamma_{^{14}\text{N}}\underline{B}\,\underline{I} \tag{4.2}$$

with the hyperfine terms being $a_\parallel = -2.14 \pm 0.07$ MHz and $a_\perp = -2.70 \pm 0.07$ MHz, the quadrupole splitting $P = -5.01 \pm 0.06$ MHz [52], $\gamma_{^{14}\text{N}} = 3.077\ \frac{\text{MHz}}{T}$ as nitrogen's gyromagnetic ratio, and I as the nuclear spin operator. Since the quadrupole splitting is larger than the applied magnetic fields in this work, it defines the eigenframe of the nuclear spins being parallel to the symmetry axis. Please note,

that any spin flip-flop terms are suppressed by the large zero-field splitting (for small magnetic fields).

^{15}N is the other stable nitrogen isotope. Its natural abundance is low (0.4%), making it an ideal candidate to label the artificial creation of nitrogen vacancy centers [59]. With a a nuclear spin of $I = \frac{1}{2}$, its Hamiltonian is given by

$$H_{\text{hf}\ ^{15}\text{N}+\text{N}_{\text{Zeeman}}} = a_\parallel S_z I_z + a_\perp \left(S_x I_x + S_y I_y \right) - \gamma_{^{15}\text{N}} \underline{B}\, \underline{I} \tag{4.3}$$

with the hyperfine terms being $a_\parallel = 3.03 \pm 0.03$ MHz and $a_\perp = 3.65 \pm 0.03$ MHz [52], and a gyromagnetic ratio of $\gamma_{^{15}\text{N}} = -4.316\ \frac{\text{MHz}}{T}$. Since hyperfine interaction is the dominant term, the eigenframe is dependent on the spin state of the electron spin (for small fields) [60]. For example, this allows for the implementation of fast coherent gates with the use of $|0\rangle$ as an ancilla state (see Chapter 7.5.1).

With clean samples (a chemically vapor deposition grown type IIa diamond, < 5ppB N) the ground state spin coherence is long lived (≈ 600 μs [13], milliseconds by dynamical decoupling (Chapter 5.2,[61, 62]) or isotopic engineering [15]) making the NV an ideal test system for room temperature quantum mechanic experiments. Additionally NV$^-$ is not limited to bulk samples, but is also found in diamonds with nanometer dimensions. The smallest nanodiamond containing a NV was reported to have a size of 7 nm [14]. This allows for nanoscale quantum metrology, e.g. in biological systems such as cells [48, 49].

4.1. Optically detected magnetic resonance
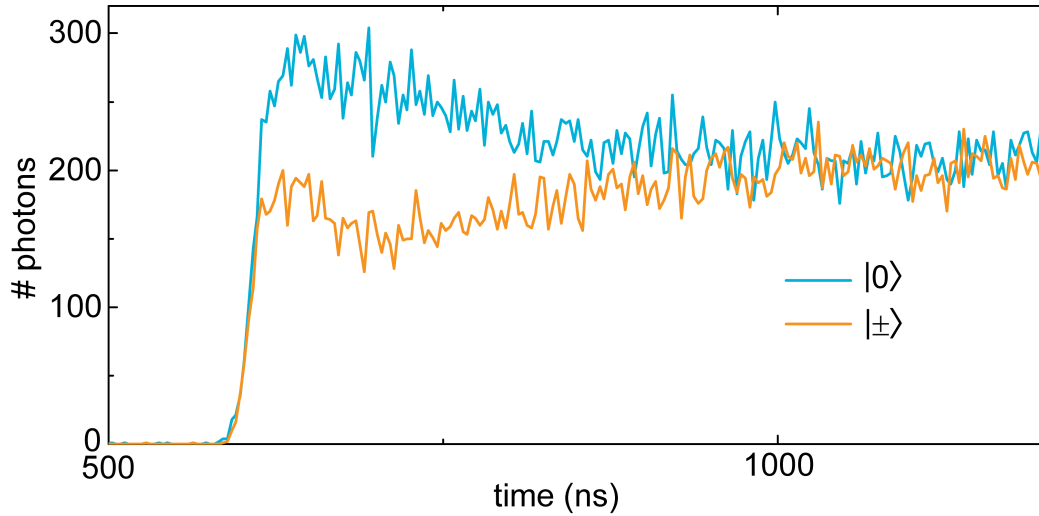
Figure 4.3.: Photon counts for different spin states. With gated laser illumination the photon counts for different spin states is detected. For $|0\rangle$ more photons are detected in the first ≈ 200 ns, since the NV is less likely to end up in the dark metastable state. Then the steady state is reached where the NV is polarized into the $m_S = 0$ state. This can be used to normalize the fluoresence counts and make the measurements comparable.

The intersystem-crossing to the shelving metastable state not only allows for spin polarization, but also for optical read out of the electron spin. Due to the long lifetime of the metastable state (≈ 300 ns [55, 56]), for $m_S = 0$ more optical cycles can be undergone as compared to $m_S = \pm 1$, where the NV ends up in the metastable state. Therefore for a gated illumination, the fluorescence signal for the first 200 - 300 ns is significantly different (Fig. 4.3). With a normalization for the steady state fluorescence (after about 1 μs laser illumination) and an integration window of 200 ns a fluoresence contrast of about 0.3 between $m_S = 0$ and $m_S = \pm 1$ is detectable.

See reference [63] and [51] for a more detailed description of the measurement process and improvement possibilities.

4.2. Charge state dynamics

The NV center exists in at least two different charge states. The neutral (NV^0) and the negatively charged state (NV^-). So far, only for NV^- ODMR has been observed. The ionization pathway between NV^0 and NV^- has been investigated by Aslam et al. [64]. There is a two-photon ionization step from NV^0 to NV^- and vice versa. First the NV has to be excited to its excited state, and then either one electron is excited to the conduction band ($NV^- \rightarrow NV^0$) or one electron from the valence band is excited to the NV level ($NV^0 \rightarrow NV^-$). Due to a two photon process, the ionization rate has a quadratic

Figure 4.4.: NV spectrum The spectrum of NV^0 and NV^- was recorded at ambient conditions. The spectral distance between the ZPL of NV^0 and NV^- is clearly visible.[1]

dependency on the excitation power below the saturation of the NV, and a linear dependence in saturation.

Since the ZPL is at 637 nm for NV^- and at 575 nm for NV^0 (see Fig. 4.4 and reference [51]), the NV charge state can be optically addressed in this wavelength window [64, 65]. While the green laser used in our experiments (532 nm) can excite both charge states, leading to a NV^0:NV^- ratio of 30:70 [65], excitation between 575 nm and 637 nm only excites NV^- (due to the lack of phonons at ambient conditions, there is no anti-Stokes absorption). This can either be used for deterministic charge pumping (see Chapter 6.5.2) from NV^- to NV^0 or, with a weak excitation, the fluorescence can be used to determine the NV charge state prior to the measurement sequence (see reference [65] and Chapter A.6).

---

[1]Data courtesy of Torsten Rendler

4.3. Coherent manipulation of the NV center
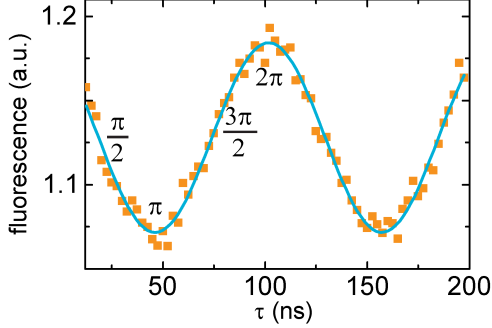
Figure 4.5.: Rabi oscilations Microwave radiation was applied in resonance with the NV transitions for a time τ.

In order to coherently manipulate the NV center, microwave radiation matching the differences in eigenenergies were applied. Please note, that in first order the allowed transitions follow the spin selection rules ($\Delta m_s = \pm 1$ or $|0\rangle \leftrightarrow |\pm\rangle$ transitions). The $|-\rangle \leftrightarrow |+\rangle$ transition is spin forbidden, only being accessible by electrical driving [66]. However in this work, only small magnetic fields were applied and therefore only the $|0\rangle \leftrightarrow |\pm\rangle$ transitions were utilized for spin control.

The interaction of a microwave field $\underline{B}_{\mathrm{mw}}$ at the frequency ν_{mw} can be described by an oscillatory term added to the Hamiltonian given by

$$H_{\mathrm{mw}} = \gamma_e \underline{B}_{\mathrm{mw}} \underline{S} \cos\left(2\pi\nu_{\mathrm{mw}}\tau\right). \tag{4.4}$$

Due to the large D, only $\underline{B}_{\mathrm{mw}}$ components orthogonal to the NV symmetry axis have an effect on the populations of the eigenstates (axial component just shift the eigenenergies periodically). Neglecting strain, electric or nonaxial static magnetic fields, the orthogonal axis can be assigned randomly, i.e. the microwave field is aligned along the x axis simplifying Eq. (4.4) to:

$$H_{\mathrm{mw}} = \gamma_e B_{\mathrm{mw}} S_x \cos\left(2\pi\nu_{\mathrm{mw}}\tau\right). \tag{4.5}$$

In matrix form the complete Hamiltonian is given by

$$H = \begin{pmatrix} D + \gamma_e B_z & \frac{1}{2}\cos\left(2\pi\nu_{\mathrm{mw}}\tau\right)\gamma_e B_{\mathrm{mw}} & 0 \\ \frac{1}{2}\cos\left(2\pi\nu_{\mathrm{mw}}\tau\right)\gamma_e B_{\mathrm{mw}} & 0 & \frac{1}{2}\cos\left(2\pi\nu_{\mathrm{mw}}\tau\right)\gamma_e B_{\mathrm{mw}} \\ 0 & \frac{1}{2}\cos\left(2\pi\nu_{\mathrm{mw}}\tau\right)\gamma_e B_{\mathrm{mw}} & D - \gamma_e B_z \end{pmatrix} \tag{4.6}$$

By transforming the Hamiltonian in the microwave frame by $\widetilde{H} = U'HU$ with $U = e^{\pm i2\pi\nu_{\mathrm{mw}}\tau S_z}$, assuming linear polarized light and applying the rotating wave approximation for σ^+ and σ^- circular polarized light [67], the effective Hamiltonian

is given by

$$
\widetilde{H} = \begin{pmatrix} D + \gamma_e B_z \pm \nu_{\mathrm{mw}} & \frac{1}{2}\gamma_e B_{\mathrm{mw}} & 0 \\ \frac{1}{2}\gamma_e B_{\mathrm{mw}} & 0 & \frac{1}{2}\gamma_e B_{\mathrm{mw}} \\ 0 & \frac{1}{2}\gamma_e B_{\mathrm{mw}} & D + \gamma_e B_z \pm \nu_{\mathrm{mw}} \end{pmatrix} \tag{4.7}
$$
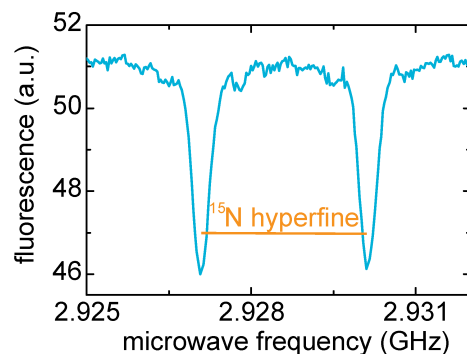
In order to drive the transition $|+\rangle \leftrightarrow |0\rangle$, the first and second main diagonal entry has to be zero. This is the case when $D + \gamma_e B_z \pm \nu_{\mathrm{mw}} = 0$, giving the resonance condition.

Under application of the microwave field, the NV population is coherently rotated between the $|0\rangle$ and the $|\pm\rangle$ states as shown in Fig. 4.5 and first demonstrated for a single NV by Jelezko et al. in reference [24]. For different lengths in τ, different rotation gates can be realized. E.g., an evolution resulting in coherent superpositions between the $|0\rangle$ and the $|+\rangle$ is called a $\frac{\pi}{2}_+$ pulse, which is equivalent to a Hadarmard gate. A π_+ pulse is rotation interchanging the population in $|0\rangle$ and $|+\rangle$ called a rotation (ROT) gate (NOT equivalent).

Please note, that the gates realized by coherent microwave radiation are only equivalent to the standard gates in quantum information technology. The rotational operations however still form a complete operational basis for quantum information processing [24].

With reducing $\Omega_{\mathrm{mw}} = \frac{1}{2}\gamma_e B_{\mathrm{mw}}$ below the coupling strength between e.g. the NV electron spin and the nuclear spin of the nitrogen, conditional gates can be realized (by driving a hyperfine resolved transition as

Figure 4.6.: Hyperfine resolved ODMR The splitting of the $|0\rangle \leftrightarrow |0\rangle$ due to the hyperfine interaction with the ^{15}N nuclei is shown.

shown in Fig. 4.6) [27]. However, for high gate fidelities, Ω_{mw} must be stronger then the inhomogeneous linewidth of the transition given by $\frac{1}{T_2^*}$. The CROT fidelity is therefore a trade off between a strong enough drive to counter the inhomogeneous linewidth while being weak enough to only affect one transition.

4.3.1. Coherent evolution and the microwave reference frame

In order to investigate the evolution of a coherent superposition state ψ_0 (created by a $\frac{\pi}{2}$ pulse), it is convenient to work in the microwave frame (Eq. (4.7)). Since any spin manipulation is applied with a phase in regard to the microwave frame,

the time evolution of a state $\psi_0 = \frac{1}{\sqrt{2}}(|0\rangle + |+\rangle)$ is given by

$$\psi(t) = e^{-i2\pi\widetilde{H}\tau}\psi_0 = e^{-2\pi i(D+\gamma_e B_z - \nu_{\mathrm{mw}})\tau}\frac{1}{\sqrt{2}}(|0\rangle + |+\rangle) = \frac{1}{\sqrt{2}}(|0\rangle + e^{-i\phi}|+\rangle) \quad (4.8)$$

with $\phi = 2\pi(D + \gamma_e B_z - \nu_{\mathrm{mw}})\tau$ being the phase between the microwave and the difference in eigenenergies (Larmor frequency). Since only population differences in $|0\rangle$ can be observed, the coherence is mapped by another $\frac{\pi}{2}$ pulse into a population difference. The observed signal S is then given by

$$S(\phi) = \left(\sin\left(\frac{\phi}{2}\right)\right)^2 \quad (4.9)$$

This is only valid, as long as the second microwave pulse stays in phase. If the second pulse is shifted by a phase ϕ_{mw}, the the phase in Eq. (4.9) is given by $\phi = \phi_{\mathrm{evo}} + \phi_{\mathrm{mw}}$. This allows for example the determination of the sign of the accumulated phase [68]. In general, pulses in phase are denoted by a x (e.g. π_x) and pulses with a 90° phase difference are denoted by a y (e.g. π_y)

5. Spin Bath

5.1. Introduction

The nitrogen vacancy center, an atom like defect in diamond has the unique potential to investigate the interaction of a central electron spin with a surrounding nuclear spin bath. With single site addressability [12], it is the perfect candidate to investigate the central spin model. For the ultra-clean samples used throughout this work (>5 ppb nitrogen impurities), the spin bath is dominated by the ^{13}C nuclear spin, which has an abundance of $\approx 1\%$. This rather thin spin bath allows for coherence times in the order of hundreds of milliseconds for the central spin [13]. Decoherence is introduced by spin flip-flop processes between the ^{13}C nuclear spins [69].

In the context of quantum technologies, the spin bath introduced decoherence is one of the largest obstacles. In order to achieve higher spin coherence times, there have been successful experiments in diluting the spin bath by isotopical engineering and thereby improving coherence properties [15]. However diluting the spin bath is not always desirable, since the nuclear bath spins are considered a resource for quantum information processing [18, 19].

With the introduction of dynamical decoupling techniques (e.g. CPMG), it will be demonstrated that the NV can be decoupled from the spin bath, allowing for coherence times not limited by the spin bath (as demonstrated for a diluted spin bath in isotropically pure ^{12}C diamond [15]). In fact, decoupling was achieved up to the limit given by the spin locking time (here the NV center is decoupled by the constant application of a microwave field).

But not only by dynamical decoupling are long coherence times accessible. By tailoring the NV eigenstates to be unresponsive to small magnetic field changes, a static decoupling from the spin bath can be achieved. Here the strain interaction has a prominent role, since it allows for the necessary mixing of the $m_S = \pm 1$ high magnetic field eigenstates.

The ^{13}C spin bath is not only a nuisance limiting the coherence times, but also yields potential applications as a quantum register [18, 30, 31]. Therefore a spectroscopy method of the bath spins independent from bath spin polarization was developed.

Here the conditional rotation of the bath spins, dependent on the electron spin state, was used to create a nuclear spin coherent state correlated to the electron spin population. These coherences were then mapped to an observable electron spin population after a free evolution time. Since the coherences are nuclear spin coherences correlated to the electron spin populations, they decay with the electron spin lattice relaxation time T_1, thus allowing for unprecedented resolution of this spectroscopy method. With storage of the electron spin population on the NV intrinsic nuclear spin memory, the hyperfine interaction between NV and bath spins becomes switchable, in principle allowing for the implementation of decoupling protocols yielding resolutions beyond T_1

5.2. Dynamical decoupling

In order to compensate for the inhomogeneous line width given by the different possible ^{13}C configurations, the coherence has to be unaffected by different bath configurations. This can be achieved by tailoring a sequence, that refocuses the acquired phase by switching the sign of the phase acquisition after half the evolution time τ. If the second evolution time is identical, an echo of the coherence can be observed. This type of decoupling scheme was first proposed and implemented in NMR by Hahn et al. in the 1950's [70]. The first implementation of the Hahn echo were designed to compensate for an inhomogeneous magnetic field distribution in an ensemble measurement.
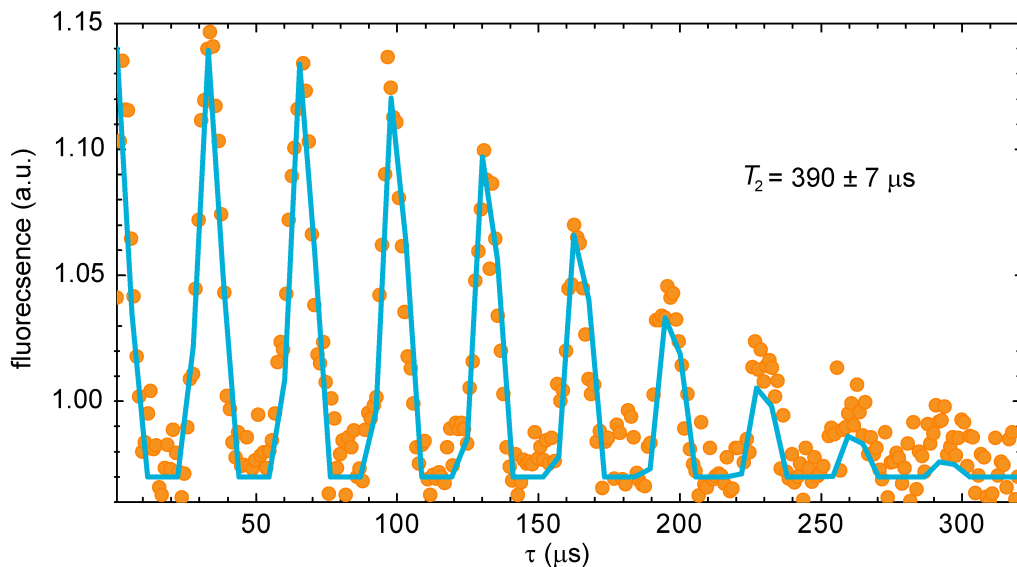
Figure 5.1.: Hahn echo measurement of a single NV center A typical Hahn echo decay is shown. The revivals due to entanglement and disentanglement with ^{13}C bath spins are clearly visible. A detailed description of this entanglement process can be found in Chapter 5.4. The decay was fitted with a Gaussian decay [13]

Nevertheless the same principle can be applied for time averaged measurements with slow fluctuations of eigenenergies. For the NV centers used in this work, these fluctuations are either given by external influences, such as the applied magnetic field, temperature and so on, as well as internal fields given by the ^{13}C spin bath. At room temperature and low magnetic fields, the spin bath is not polarized, therefore, an effective field due to the spin bath has a width given by all possible spin bath configurations. This inhomogeneous broadening can be compensated, leading to longer coherence times e.g. the Hahn echo decay shown in Fig. 5.1.

5.2.1. Basic principles
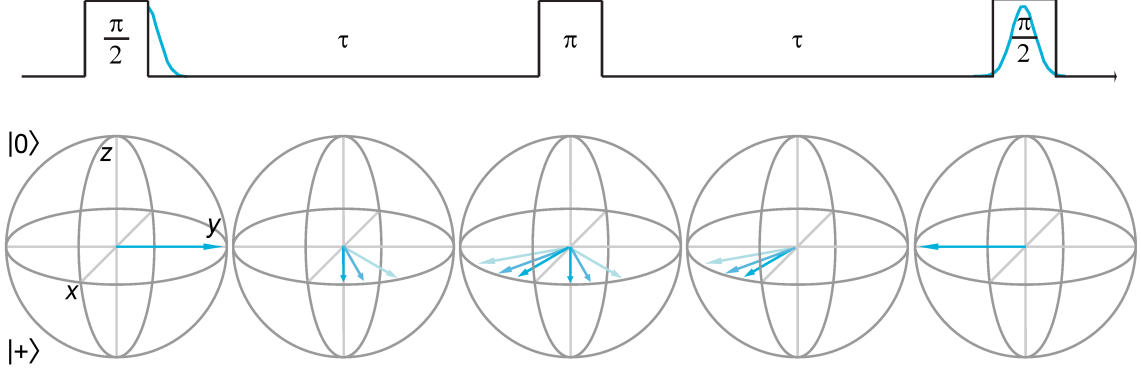
Figure 5.2.: Bloch sphere representation of a Hahn echo After initializing the coherence with a $\left(\frac{\pi}{2}\right)_x$ pulse (a $\frac{\pi}{2}$ rotation around the x axis), the spin state starts rotating around the z axis with the detuning between Larmor and microwave frequency. Since each measurement has slightly different detunings, (inhomogeneous line width), the accumulated phase for τ spreads out (dephasing). With a $(\pi)_x$ pulse (a π rotation around the x axis), the coherence is reflected on a mirror plane given by x and z, leading to a refocusing of the spin coherence after τ. Since only the population in $|0\rangle$ can be read out, the accumulated phase is mapped into a population difference by another $\left(\frac{\pi}{2}\right)_x$ pulse.

The working principle of dynamical decoupling is to tailor a sequence out of microwave pulses to refocus any accumulated phase. To first order, the interaction of the spin bath with the NV center can be described by an effective magnetic field $\underline{B}_{\text{eff}}(t)$. This classical description of the spin bath by an effective field is a Markovian model (no back action between spin bath and the NV), but allows a fairly good description of the dephasing process. The NV center Hamiltonian, neglecting hyperfine interaction, can be described as

$$H = DS_z^2 + \gamma_e \left(\underline{B}_{\text{static}} + \underline{B}_{\text{eff}}(t)\right) \underline{S}, \tag{5.1}$$

where $\underline{B}_{\text{static}}$ is the static magnetic field and $\underline{S}$ is the NV spin operator. Since the zero field splitting is $D = 2.87$ GHz, nonaxial interactions can be neglected in the first order simplifying the Hamiltonian to

$$H = DS_z^2 + \gamma_e \left(B_{z\,\text{static}} + B_{z\,\text{eff}}(t)\right) S_z. \tag{5.2}$$

A coherent superposition $\psi_0 = \frac{1}{\sqrt{2}}\left(|0\rangle + |1\rangle\right)$, created by a $\frac{\pi}{2}$ pulse, freely evolves for the time τ. Assuming resonant excitation, the rotating wave approximation simplifies Eq. (5.2) to $H = \gamma_e B_{z\,\text{eff}} S_z$. Therefore the time evolution can be described

by

$$\psi(t) = e^{-i2\pi H\tau}\psi_0 = e^{-i2\pi H\tau}\frac{1}{\sqrt{2}}\left(\left|0\right\rangle + \left|+\right\rangle\right) = \frac{1}{\sqrt{2}}\left(\left|0\right\rangle + e^{-i\phi}\left|+\right\rangle\right), \tag{5.3}$$

where ϕ is the accumulated phase given by $\phi = \int_0^\tau 2\pi\gamma_e B_{z\,\mathrm{eff}}(t)dt$. For different states of the ^{13}C bath, $B_{z\,\mathrm{eff}}$ takes different values within a Gaussian distribution. The latter is caused by the thermal state of the spin bath, yielding a even distribution over all states at room temperature [71].

In order to decouple the coherence from the $B_{z\,\mathrm{eff}}$ distribution, dynamical decoupling can be used. The simplest form of dynamical decoupling is the Hahn echo. Here a refocusing pulse is inserted after an evolution time τ, giving an echo of the spin coherence at 2τ (see Fig. 5.2). The refocusing π pulse inverts the sign of the collected phase giving a collected phase of

$$\phi = \int_0^\tau 2\pi\gamma_e B_{z\,\mathrm{eff}}(t)dt + \int_0^\tau -2\pi\gamma_e B_{z\,\mathrm{eff}}(t)dt$$
$$\xrightarrow{B_{z\,\mathrm{eff}}(t)=const.} 2\pi\gamma_e B_{z\,\mathrm{eff}}\tau - 2\pi\gamma_e B_{z\,\mathrm{eff}}\tau = 0. \tag{5.4}$$

Therefore a Hahn echo can be used to refocus static fields, e.g. the inhomogeneous line broadening due to different spin bath configurations [67, 70].
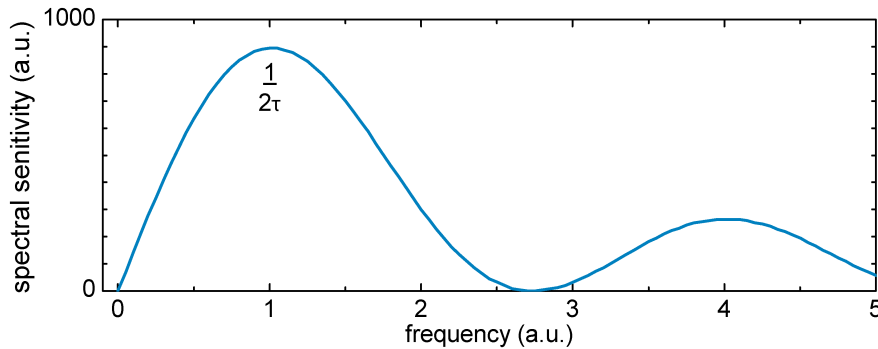
Figure 5.3.: Hahn echo spectral response The blue line shows the spectral sensitivity S of the Hahn echo sequence. For a longer τ the peak spectral sensitivity is shifted to lower frequencies.

However fluctuations on shorter time scales are not refocused. With the sensitivity function $S(t)$, describing the sign of the accumulated phase, this can be analyzed. For a Ramsey type free evolution experiment the sensitivity is given by

$$S_{\mathrm{FID}}(t) = 1, \tag{5.5}$$

while for a Hahn echo it is given by

$$S_{\text{Hahn}}(t) = \begin{cases} 0; & t < 0 \\ 1 - 2\Theta(t - \tau); & 0 < t < 2\tau \\ 0; & t > 2\tau \end{cases} , \qquad (5.6)$$

where $\Theta(t - \tau)$ is the Heaviside function. A Fourier transformation of the sensitivity function reveals the spectral sensitivity S of the NV decoherence under dynamical decoupling. The numerical result is shown in Fig. 5.3. The key feature is, that S is zero at $\nu_{\text{noise}} = 0$, and its maximum is at $\nu_{\text{noise}} = \frac{1}{2\tau}$. Please note that the other maxima correspond to the odd numbered higher harmonics of $\nu_{\text{noise}} = \frac{1}{2\tau}$.

The noise spectrum of a nuclear spin bath can be approximated by $N = \frac{1}{\nu_{\text{noise}}^2}$ [62]. Since the maximum of F is inversely proportional to τ, a longer τ results in a stronger noise and therefore dephasing of NV coherence.

The classical description of the spin bath by an effective field is incomplete. Since the magnetic moment of the NV is dependent on the electron spin state (zero for $|0\rangle$, nonzero for $|\pm\rangle$), the local field $\underline{B}_{\text{local}} = \underline{B}_z + \underline{B}_{\text{hyperfine}}$ at the position of the ^{13}C is dependent on the electron spin state. If there is an angle between the Zeeman and hyperfine field, B_{local} has two spin dependent orientations. This leads to two different eigenframes for the ^{13}C (if the hyperfine interaction is in the same order as the nuclear Zeeman effect). A fast operation on the electron spin (nonadiabatic for the ^{13}C), generates a coherence in the new eigenframe that rotates with the ^{13}C Zeeman interaction $\nu_{^{13}\text{C Zeeman}}$. The state dependent evolution causes the NV to entangle and disentangle with the ^{13}C bath spins, if the electron spin is in a superposition state. Revivals of coherence can be observed when the spin bath is disentangled for $\frac{1}{\tau} = \nu_{^{13}\text{C Zeeman}}$ [13] (see Fig. 5.1). This effect will be exploited to spectroscopy the ^{13}C spin bath (see Chapter 5.4). With adjusting τ to be multiples of $1/\nu_{^{13}\text{C Zeeman}}$, these bath dynamics can be refocused and the coherence times analyzed.

5.2.2. Single spin CPMG
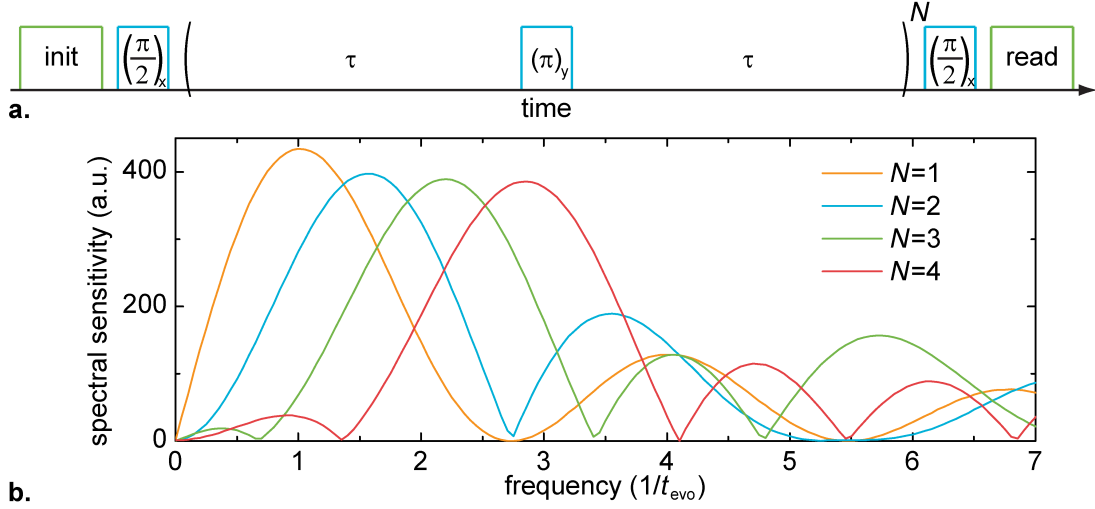
Figure 5.4.: Schematic of the CPMG sequence. a. In the CPMG sequence the free evolution and the refocusing pulse $(\pi)_y$ is repeated N times, N giving the order of the CPMG sequence. A 90° phase shift between the $\left(\frac{\pi}{2}\right)_x$ pulse and the $(\pi)_y$ pulse compensate for pulse errors in x direction. **b.** The spectral sensitivity of different orders of CPMG was calculated for the same total evolution time t_{evo} ($\tau = \frac{t_{\text{evo}}}{2N}$). One clearly sees, that the maximum sensitivity is moved to higher noise frequencies for higher orders of decoupling.

The decoupling protocol developed by Carr, Purcel, Meiboom and Gill (CPMG) [16, 17] is an extension of the spin echo developed by Hahn [70]. In order to achieve a better decoupling from the noise field, more refocusing pulses are added. As shown in Fig. 5.4a, the pulses are added equidistant from the spin echo, giving a pulse sequence $\left(\frac{\pi}{2}\right)_x - \left(\tau - (\pi)_y - \tau\right)^N - \left(\frac{\pi}{2}\right)_x$, where N is the CPMG order (N=1 is a Hahn echo). As shown in Fig. 5.4b, for the same total evolution time ($2N\tau$) the peak in the spectral sensitivity is shifted to higher frequencies, thereby reducing the accumulated noise due to the lower noise intensity (assuming a Lorentzian noise model [62]). This allows for a longer total phase evolution time t_{evo} for the same amount of accumulated decoherence, resulting in a longer phase memory time T_2. CPMG, however, does not compensate the conditional rotations of the ^{13}C bath spins dependent on the electron spin state. Therefore as for the Hahn echo (see Fig. 5.1 and reference [13]), revivals of the coherence with $\tau = \frac{1}{\nu_{13\text{C Larmor}}}$ can be observed (see Fig. 5.5). In order to compensate for this bath dynamics, τ was chosen to match the first revival at $\tau = \frac{1}{\nu_{13\text{C Larmor}}} = 27 \ \mu$s. With this, the coherence time of the NV center was probed by increasing the order of N in every measurement step. With increasing the pulse number and keeping τ constant, unlike for a Hahn echo where τ is increased, the peak in the spectral sensitivity (given by $\frac{1}{4\tau}$), in the first order, remains unaffected by a longer evolution time and does not move to lower
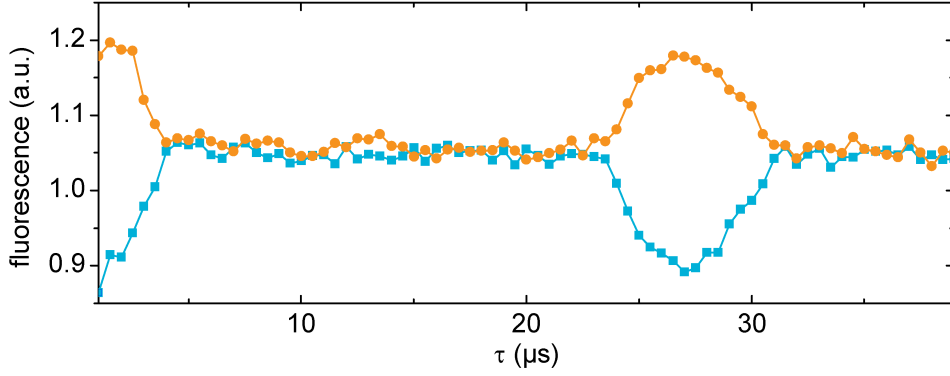
Figure 5.5.: Electron spin coherence revivals for CPMG CPMG in the order $N = 2$ was implemented. The blue data uses a $\left(\frac{\pi}{2}\right)_x$ pulse to map the coherence to a observable population difference while the orange data uses a $\left(\frac{3\pi}{2}\right)_x$ pulse. This allows to see the coherence at the full contrast. For $\tau = \frac{1}{\nu_{13\text{C Larmor}}}$, a revival of the NV coherence can be observed.

frequencies (unlike when increasing τ in a Hahn echo). This leads to a significantly longer measured coherence time $T_{2\text{ CPMG}} = 2.44 \pm 0.44$ ms (see Fig. 5.6) than for a Hahn echo $T_{2\text{ Hahn}} = 370 \pm 7$ μs (see Fig. 5.1).

With spin locking $\left(\left(\frac{\pi}{2}\right)_x - \text{mw}_y(\tau) - \left(\frac{\pi}{2}\right)_x\right)$ [40], the maximal achievable decoupling from the noise channels was measured to be $T_{1\rho} = 2.47 \pm 0.27$ ms. Here the spin coherence is "locked" in a coherent superposition by the 90° phase shifted microwave field, which is applied during the whole evolution time [67]. Spin locking can be considered the limit for pulse based decoupling, since the accumulated noise is collected during the application of the microwave field.

The spin relaxation time was $T_1 = 5.93 \pm 0.7$ ms (see Fig. 5.6 and A.9). $T_{2\text{ CPMG}} \approx T_{1\rho} \approx \frac{1}{2}T_1$ indicates, that a noise floor was reached and the system has been decoupled from dephasing sources as well as possible and the spin-lattice relaxation T_1 process is now governing the coherence times.

Please note, that the CPMG sequence as described here only compensates for pulse error in the real part of the coherence (x). In order to preserve the full coherence, a more elaborate sequence like CPMG$_{xy}$ with alternating pulses in x and y can be implemented [62, 72].
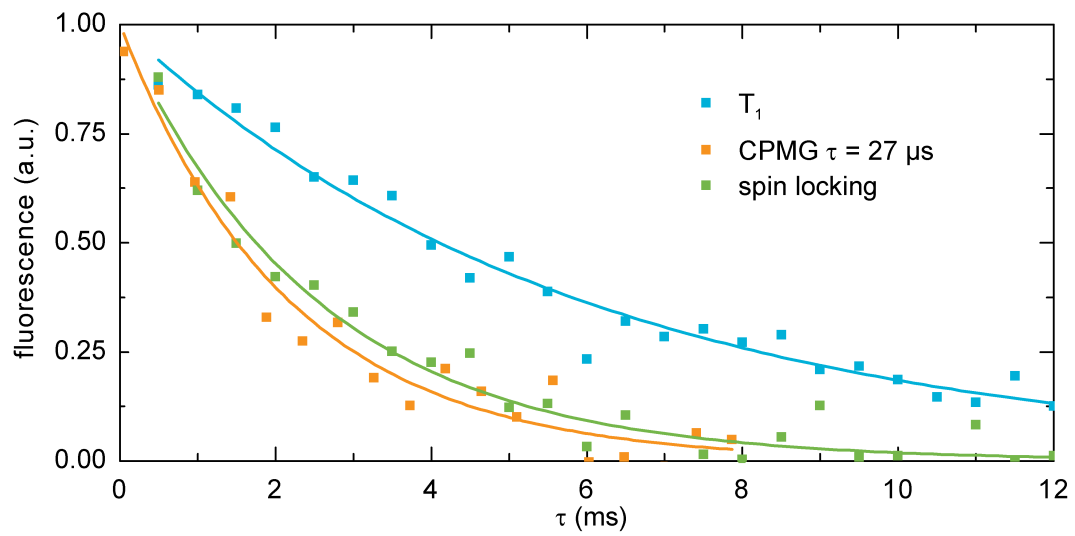
Figure 5.6.: Coherence times using CPMG. Here the spin life time $T_1 = 5.93 \pm 0.7$ ms is shown in blue. In orange the spin coherence lifetime $T_{2\,\text{Hahn}} = 370 \pm 7$ μs and in green the spin locking lifetime $T_{1\rho} = 2.47 \pm 0.27$ ms are shown. The lines are exponential fits of the measured data.

5.3. Decoupling by eigenstate tailoring
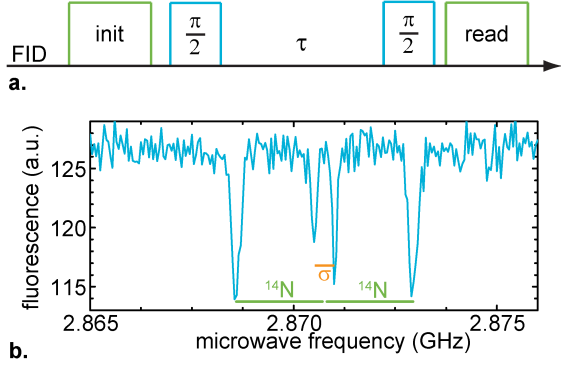
Figure 5.7.: Spectrum and measurement sequence. a. Ramsey measurement sequence to determine T_2^* **b.** Hyperfine resolved spectrum at $B_z \approx 0$. The splitting due to the hyperfine interaction as well as the strain splitting for $m_I = 0$ is clearly visible.

The inhomogeneous line broadening, limiting the free spin evolution coherence time T_2^*, is normally given (for a clean sample) by the thermal distribution of the ^{13}C spin bath [73]. As demonstrated by Balasubramanian et al. in reference [15], engineering a sample with depleted ^{13}C content can increase coherence times tremendously. Here we want to discuss another avenue to increase T_2^*. Instead of depleting the spin bath, the interaction between the NV center and magnetic fields is switched off in the first order by tailoring the proper eigenstates.

We first look at the effective spin Hamiltonian, omitting hyperfine interaction and electric fields:

$$H = DS_z^2 + \gamma_e \underline{S} \ \underline{B} + \sigma \left(S_x^2 - S_y^2 \right). \tag{5.7}$$

Where D is the crystal field splitting, γ_e is the electrons gyromagnetic ratio, $\underline{B}$ is the magnetic field vector, σ is the transverse crystal strain field and $\underline{S}$ is the spin operator. Omitting transverse magnetic fields (B_x and B_y leads to mixing of $|0\rangle$ and $|\pm\rangle$, which is suppressed by D), this simplifies to

$$H = DS_z^2 + \gamma_e S_z B_z + \sigma \left(S_x^2 - S_y^2 \right) = \begin{bmatrix} D + \gamma_e B_z & & \sigma \\ & 0 & \\ \sigma & & D - \gamma_e B_z \end{bmatrix} \tag{5.8}$$

The diagonalization of the Hamiltonian gives the eigenenergies of the electron spin.

$$\begin{bmatrix} D + \sqrt{\left(\gamma_e B_z\right)^2 + 4\sigma^2} & & \\ & 0 & \\ & & D - \sqrt{\left(\gamma_e B_z\right)^2 + 4\sigma^2} \end{bmatrix} \tag{5.9}$$

If $\gamma_e B_z \gg 2\sigma$ the eigenstates of the Hamiltonian are also eigenstates of S_z $|0, \pm 1\rangle$. However for $\gamma_e B_z \ll 2\sigma$, state mixing leads to a superposition of $|\pm 1\rangle$, suppressing the axial Zeeman effect. The eigenstates of the strain dominated regime are given in Chapter 6.4.1.

Therefore by tailoring the spin eigenstates, the interaction with the magnetic spin bath is controllable. Please note, that the coupling of a linearly polarized microwave field (as used in this work) becomes dependent on strain orientation ϕ_σ [66].

The coherence properties were investigated using a NV center with $\sigma = 189$ kHz. In order to avoid any effects due to hyperfine interaction with the ^{14}N nucleus, the measurements were conducted in the $|m_I = 0\rangle$ subspace. Here the hyperfine interaction is zero due to the vanishing magnetic moment of nuclear spin state allowing the observation of the strain splitting (see Fig. 5.7b).
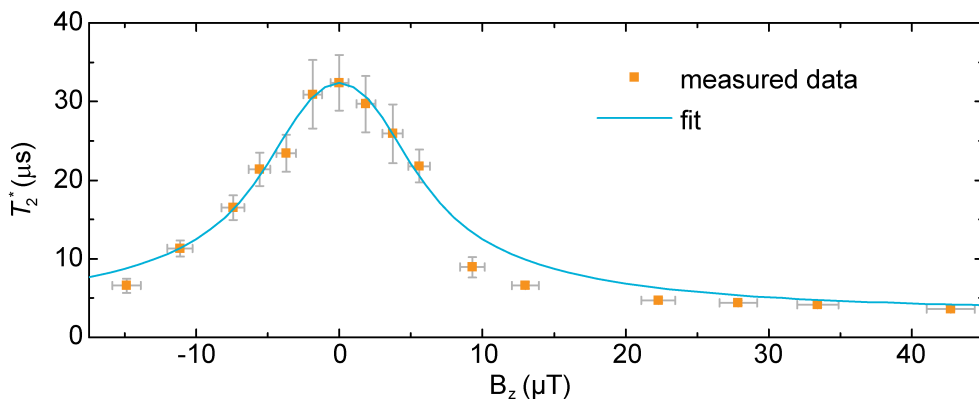
Figure 5.8.: Dependence of T_2^* on the eigenstates. The phase memory time T_2^* was measured for different axial magnetic fields, using the measurement scheme shown in Fig. 5.7.

T_2^* for different axial magnetic fields was measured, using a Ramsey experiment (see Fig. 5.7a). The dependence of T_2^* on B_z is shown in Fig. 5.8. In order to fit the observed dependence on the magnetic field interaction, we assumed a model with Gaussian magnetic field distribution given by $T_{2\,\text{high field}}^*$ and a magnetic field independent noise field (e.g. temperature, phonons, ...). The inhomogeneous linewidth was simulated numerically by integrating over the possible detunings weighted by a Gaussian distribution given by $T_{2\,\text{high field}}^*$ and $T_{2\sigma}^*$. By a numerical minimization of the mean square deviation, the data was fitted using only $T_{2\,\text{high field}}^*$ and $T_{2\sigma}^*$ as free parameters. The measured data and the fit is shown in Fig. 5.8.

The numeric optimization yield $T_{2\,\text{high field}}^* = 3.0$ μs and $T_{2\sigma}^* = 35.1$ μs. The highest observed coherence time is $T_{2\,\text{max}}^* = 32.4 \pm 3.5$. $T_{2\,\text{high field}}^*$ yields the same values as measured for the high field case. The discrepancy between $T_{2\sigma}^*$ and $T_{2\,\text{max}}^*$ can be understood by considering that the magnetic field noise from the spin bath is only suppressed in first order. Nevertheless, the observed maximal coherence time of $T_{2\,\text{max}}^*$ is comparable to the values obtained in isotopically purified samples (^{13}C spin bath is depleted to 0.1% [15], Chapter 7.3).

5.4. Correlation spectroscopy of the spin bath
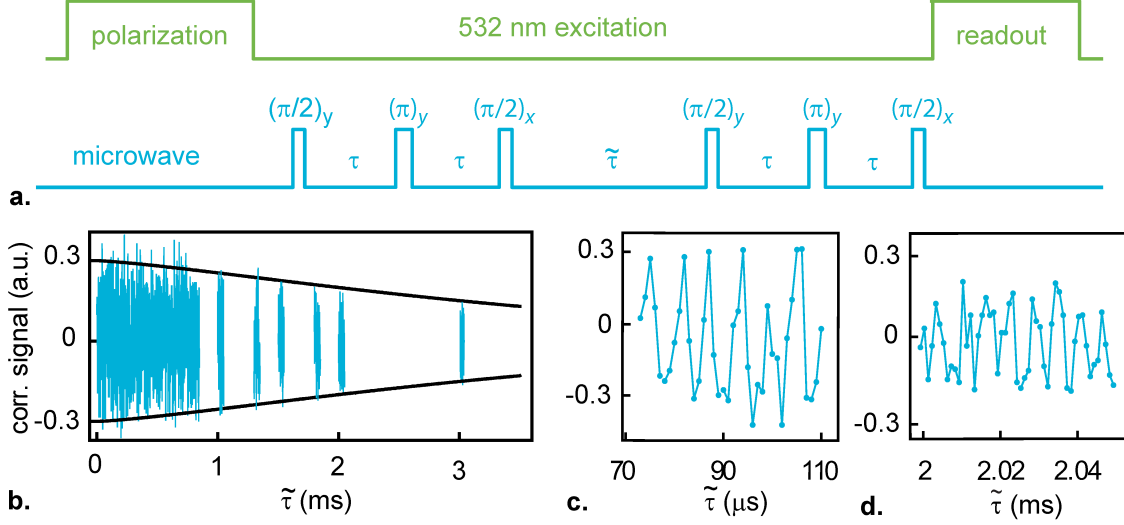
Figure 5.9.: ^{13}C correlation sequence. a. Pulse sequence schematic b. Correlation signal of NV 1 with $B_z = 15.6$ mT and a ^{13}C Larmor frequency of $\nu_C = 167$ kHz. Due to measurement time restrictions, the signal was measured only for short intervals for $\widetilde{\tau}$ greater than 1 ms. $\tau = 3$ µs was kept constant. c. Zoom in on the correlation data for short $\widetilde{\tau}$. d. Zoom in for longer $\widetilde{\tau}$. The correlation signal has a life time larger than 3 ms.

Various implementations of quantum information processing as well as quantum metrology are based on the interaction of the central NV electron spin with a register of surrounding ^{13}C spins, e.g. phase flip quantum error correction [18]. The identification and spectroscopy of a large number of weakly coupled ^{13}C spins remains challenging [74, 75]. A new spectroscopic method was developed, to investigate the ^{13}C spin bath surrounding a central NV center. Here the state of the spin bath is stored in the NV electron spin by a conditional evolution, and then after an evolution time $\widetilde{\tau}$ the evolved state of the spin bath is correlated with the stored information. During $\widetilde{\tau}$, the ^{13}C nuclear spins undergo an evolution due to their Larmor frequency ν_{Larmor}. Since the Larmor frequency is dependent on the electron spin state due to hyperfine interaction, the coupling between NV and its surrounding bath spins can be investigated. Because the information is stored in the electron spin state and weak homo-nuclear coupling, the spectroscopy resolution is limited by the the electron spin relaxation time T_1, but can be in principle be extended by repolarization [19].

The correlation spectroscopy is based on creating a coherence on the ^{13}C which are conditional on the electron spin state. Ideally a state of the form $|+\rangle \otimes (|\uparrow\rangle + |\downarrow\rangle)$ or $|0\rangle \otimes (|\uparrow\rangle - |\downarrow\rangle)$ would be created and read out. However, due to the thermalization of the nuclear spins at room temperature, no coherence can be created by driving the nuclear spins directly. Therefore, we employ a method based on conditional

nuclear spin rotations. Here, the different eigensystems dependent on the electron spin state are used to facilitate coherent spin rotations [60] (like the nuclear spin control introduced in Chapter 7.5.1). Please note, that in this chapter the magnetic field was always applied along the symmetry axis of the NV.

In order to understand the rotations due to the different eigensystems, the Hamiltonian containing the hyperfine coupling has to be analyzed. For one additional ^{13}C it is given by
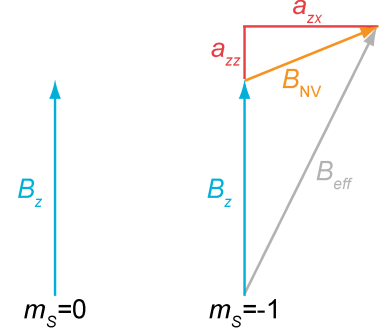
$$H = DS_z^2 + \gamma_e B_z S_z + a_{zz} S_z I_z + a_{zx} S_z I_x + \gamma_I B I_z, \quad (5.10)$$

where I_z and I_z are nuclear spin operators, $\gamma_I = 10.71 \frac{\text{MHz}}{\text{T}}$ is the ^{13}C's gyromagnetic ratio [13] and a_{zz} and a_{zx} are the hyperfine coupling terms between NV and ^{13}C. Please note, that for simplicity we considered the ^{13}C to be in the x, z plane. a_{zz} and a_{zx} are dependent on the position of the ^{13}C with regard to the NV center and given by the dipolar interaction. Since the dipolar field of the NV electron spin is in most cases not parallel to B_z at the position of the ^{13}C, a a_{zx} hyperfine term has to be introduced (see Fig. 5.10).

Figure 5.10.: Electron spin dependent ^{13}C eigensystem. The eigensystem is along the interaction. While for $m_S = 0$ only $\underline{B}_z$ yields an interaction giving the axis of the eigensystem, for $m_S = -1$, the magnetic field from the dipolar interaction B_{NV} has to be added giving a new axis with $\underline{B}_{eff} = \underline{B}_z + \underline{B}_{\text{NV}}$.

a_{zx} is responsible for a different axis of the ^{13}C eigensystem for $|-\rangle\langle-|$. If analyzing the Hamiltonian with the eigenframe along the NV symmetry axis (S_z), a_{zx} rotates the ^{13}C spin for $|-\rangle\langle-|$. The population transfer becomes maximal, when the $|0\rangle\langle0|$ nuclear spin eigenframe and $|+\rangle\langle+|$ eigenframe are orthogonal ($a_{zz} = \gamma_I B_z$ and $a_{zx} \neq 0$). For simplicity, we will further analyze that case. The correlation sequence, as shown in Fig. 5.9a, is $\left(\frac{\pi}{2}\right)_y - \tau - (\pi)_y - \tau - \left(\frac{\pi}{2}\right)_x$. Applying the pulse sequence to a polarized electron spin state and a nuclear thermalized state yields the following state:

$$\rho_{\text{cor}} = \begin{bmatrix} \frac{1}{4} + \frac{1}{8}\sin(a)^2\sin(b) & \frac{1}{8}\left(1 - e^{ib}\right)\sin(2a) & 0 & 0 \\ \frac{1}{8}\left(1 - e^{-ib}\right)\sin(2a) & \frac{1}{4} - \frac{1}{8}\sin(a)^2\sin(b) & 0 & 0 \\ 0 & 0 & \frac{1}{4} - \frac{1}{8}\sin(a)^2\sin(b) & \frac{1}{8}\left(e^{ib} - 1\right)\sin(2a) \\ 0 & 0 & \frac{1}{8}\left(e^{-ib} - 1\right)\sin(2a) & \frac{1}{4} + \frac{1}{8}\sin(a)^2\sin(b) \end{bmatrix}$$

$$(5.11)$$

with $b = 2\pi\gamma_I B_z\tau$ and $a = \pi a_{zx}\tau$. Please note that the pure electron spin coherences are set to zero, due to dephasing during $\widetilde{\tau}$. Also ρ_{cor} is written in the reduced basis given by $|0\rangle, |-\rangle, |\uparrow\rangle$ and $|\downarrow\rangle$.

Please note, that created coherence and the observed signal becomes maximal for $\tau = \frac{1}{2\nu_C}$ (see Fig. 5.13d.). Therefore, $\tau = \frac{1}{2\nu_C}$, with $\nu_C = \gamma_I B_z$ as the ^{13}C nuclear Zeeman energy, was used. This corresponds to center of the Hahn echo spin envelope modulation (revivals are periodic with ν_C) [13]. With $\tau = \frac{1}{2\nu_C}$, ρ_{cor} simplifies to

$$
\rho_{\text{cor}} = \begin{bmatrix}
\frac{1}{4} & \frac{1}{4}\sin(2a) & 0 & 0 \\
\frac{1}{4}\sin(2a) & \frac{1}{4} & 0 & 0 \\
0 & 0 & \frac{1}{4} & -\frac{1}{4}\sin(2a) \\
0 & 0 & -\frac{1}{4}\sin(2a) & \frac{1}{4}
\end{bmatrix}. \tag{5.12}
$$

The generated nuclear spin coherences have become maximal and are only dependent on a_{zx}. This gives rise to second a resonance condition. For $a_{zx} = \frac{1}{4\tau}$, the coherence has a maximal value. Therefore by choosing the right magnetic field, and hence the right τ, the correlation sequence can be made selective to certain hyperfine couplings, allowing to individually address different ^{13}C with varying a_{zx} coupling strengths.
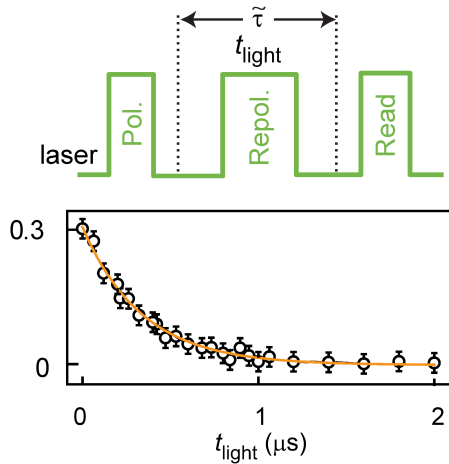
Figure 5.11.: Correlation signal under repolarization. upper panel In order to probe the dependence on the correlation between ^{13}C and the electron spin, the electron spin was repumped turing $\widetilde{\tau}$. **lower panel** The correlation signal decays exponentially with increasing laser pupming time t_{light}.

After creating the nuclear spin coherence, the ρ_{cor} evolves freely for the time $\widetilde{\tau}$. There is a total phase accumulated depending on the state of the electron spin. For the $|0\rangle\langle 0|$ electron state, a phase of $\phi_0 = 2\pi\nu_C$ is collected, while for the $|-\rangle\langle -|$ electron state, the phase accumulation is governed by $\phi_- = 2\pi\nu_{\text{hyperfine}}$, where $\nu_{\text{hyperfine}} = \sqrt{a_{zx}^2 + (a_{zz} - \gamma_e B_z)^2}$. Using the correlation sequence a second time, the phases ϕ_0 and ϕ_- are mapped into an observable population difference.

Such a correlation spectroscopy is shown in Fig. 5.9. Since nuclear spin correlations are created and read out, the signal is not decaying with the electron spin coherence time, but with the phase memory time of the ^{13}C nuclei $T_{2\,^{13}\text{C}}^*$ and the spin lifetime of the electron spin $T_{1\,\text{electron}}$. Due to the weak homonuclear coupling, $T_{2\,^{13}\text{C}}^*$ is given by $T_{1\,\text{electron}}$ [30]. Therefore, the hyperfine spectrum can be investigated with a frequency resolution of $1/T_{1\,\text{electron}}$, allowing for unprecedented accuracy. In order to sample the full hyperfine spectrum, the magnetic field B_z, and thereby τ, is swept and a correlation

spectroscopy recorded. By adjusting τ, the sequence becomes sensitive to different hyperfine couplings. Since the creation of the correlation is dependent on electron spin coherences, the smallest detectable hyperfine a_{zx} coupling is limited by the electron spin coherence time T_2. However, T_2 can be improved to reach values limited by the spin lifetime $\frac{1}{T_{1\,\text{electron}}}$ using higher order dynamical decoupling such as CPMG (see Chapter 5.2.2).

Please note, that the correlation of the electron spin state to the nuclear spin coherences is essential. In Fig. 5.11 the correlation signal is plotted, if during $\widetilde{\tau}$ a weak laser field is applied for the time t_{light}. The correlation signal decays exponentially, as more and more of the electron spin correlation is polarized into $|0\rangle$.
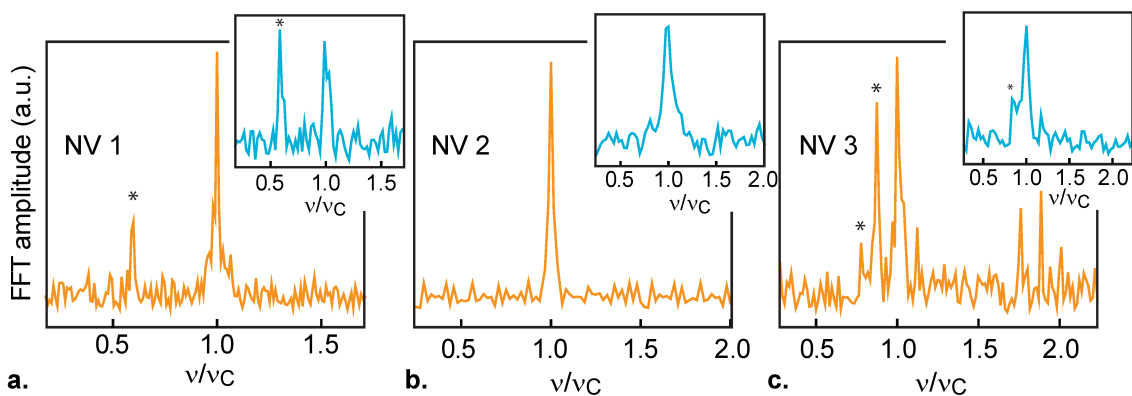
Figure 5.12.: Correlation spectra for different NV. Fourier transformations of the correlation signal for different NVs shown. The horizontal axis is normalized to the corresponding Larmor frequency ν_C and $\tau = \frac{1}{2\nu_C}$ is chosen. The inserts show the corresponding Fourier transformation of the Hahn-echo signal. The asterisk marks peaks resulting from spectral folding. For **a.**, the applied magnetic field was $B_z = 15.6$ mT, for **b.** $B_z = 16.8$ mT and for **c.** $B_z = 18.7$ mT.

Using the correlation spectroscopy sequence, different NV centers are investigated for coupling to ^{13}C nuclei. In Fig. 5.12, the correlation spectra for different NV centers are analyzed. For example NV 2, shows only one peak at ν_C, meaning that $\nu_{\text{hyperfine}}$ for the observed ^{13}C is too small to be detected with the chosen interval of $\widetilde{\tau}$. While for NV 3 several different ^{13}C are addressed by the chosen τ leading to multiple frequencies in the spectrum.

A detailed theoretical analysis will be found in the Ph.D thesis of Christian Burk.

5.4.1. Magnetic field dependence
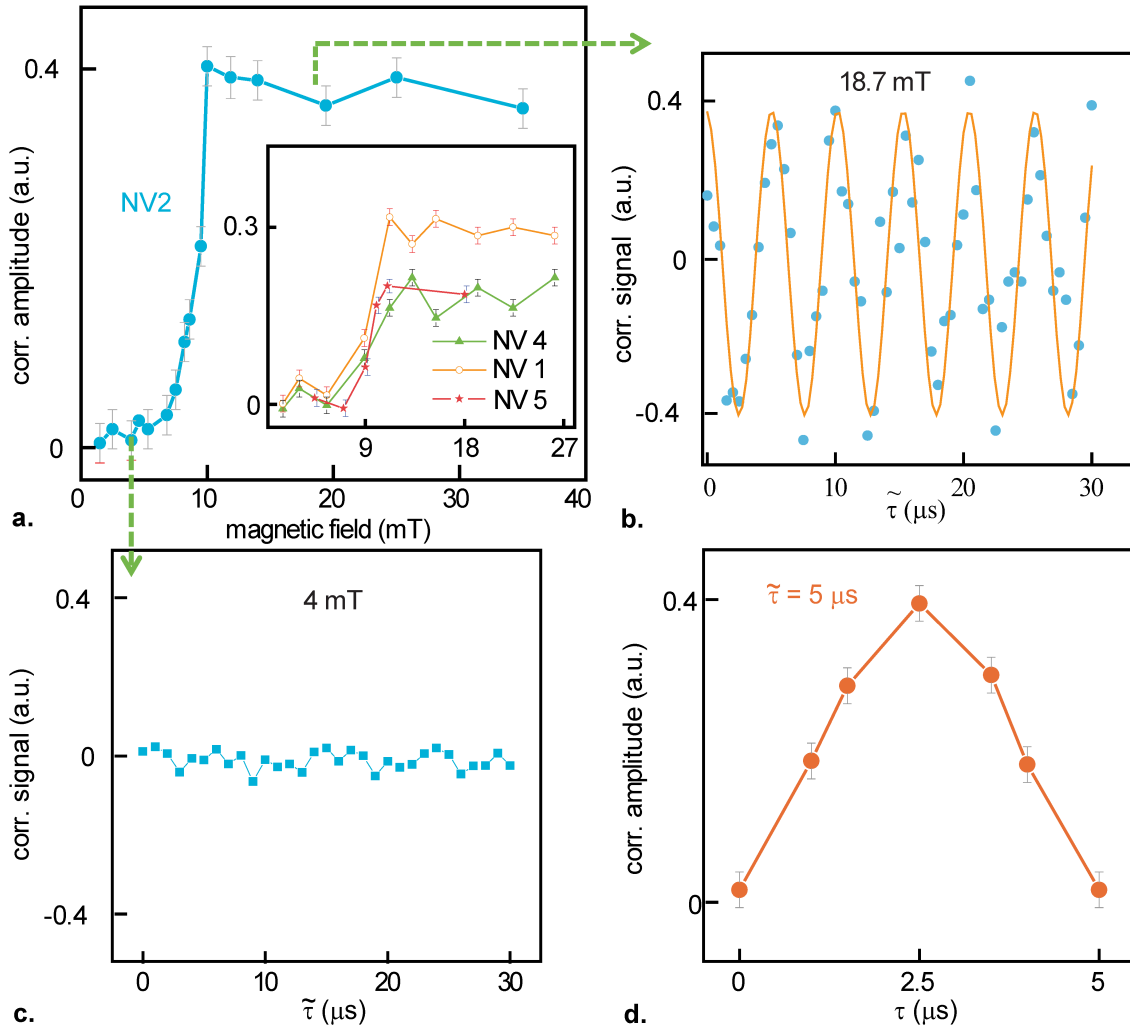
Figure 5.13.: Correlation spectrum visibility vs. B_z. a. Signal amplitude as a function of the applied magnetic field B_z. The insert shows similar curves for other NV centers. **b.** Correlation signal for $B_z = 18.7$ mT. The sinusoidal solid line, here serving only as a reference, exposing the signal periodicity at ν_C. **c.** Correlation signal for $B_z = 4$ mT. In **a.** through **c.**, $\tau = \frac{1}{2\nu_C}$. **d.** Here the signal amplitude with a fixed $\tilde{\tau} = 5$ μs and varying τ is shown.

The correlation signal could only be observed for magnetic fields larger than $B_c \approx$ 10 mT. Below B_c no correlation signal could be observed. This trend is shown in Fig. 5.13. Numerical simulations based on the cluster expansion method [76] by Christian Burk showed a similar trend but could not replicate the steep rise of the correlation signal. Also not for every NV a correlation spectrum was observed. At this point, the nature of the magnetic field dependence remains an open question.

5.4.2. Interaction switching by the NV state

The evolution during $\widetilde{\tau}$ is governed by the electron spin populations. Since after the first correlation sequence the the NV population is evenly distributed between $|0\rangle\langle 0|$ and $|-\rangle\langle -|$, the evolution is governed by ν_C as well as $\nu_{\text{hyperfine}}$.

This has two possible applications. First the NV spin can be considered a gradient magnet, allowing for a spatial mapping of the surrounding ^{13}C nuclei with sub-lattice site precision. In order to gain full control of the gradient field, the NV spin has to be polarized again. Since this would destroy the correlation stored in the electron spin population, first the population has to be stored in a nuclear spin memory. Here we used the ^{14}N nucleus to store the correlation. With working at 41.2 mT (close to the exited state level anti-crossing at 51.2 mT), not only is the electron spin polarized by illumination, but the host ^{14}N is also polarized into the $|m_I = +1\rangle$ state[77]. Therefore a partial swap operation (PSWAP) between the $|0, -\rangle$ electron spin levels and the $|m_I = 0, +1\rangle$ nuclear spin levels allows for storing the information while repolarizing the electron spin. With spin rotations of the electron spin, the hyperfine interaction becomes switchable.

Due to the interaction of the electron spin with the nuclear spin, the coherence times of the ^{13}C is governed by the lifetime T_1 of the electron spin. It has been demonstrated by Maurer et al. in reference [19] that by introducing a fast dynamic on the electron spin state, the nuclear spin can be decoupled allowing for coherence times in the order of seconds. In this first demonstration, the dynamics were introduced by strong laser pumping of the NV$^0 \leftrightarrow$NV$^-$ dynamic. However in our experiments, it would be sufficient to constantly repolarize the NV center with a weak light field or driving the NV spin transitions fast enough (assuming a magnetic field large enough to suppress electron-nuclear spin flip flops close to the exited state level anticrossing [28]). This would in principle allow for spectral resolution not limited anymore by T_1, but by the coherence times of the ^{13}C coupling to much weaker noise sources.

**pswap gate for population storage in the ^{14}N nuclear spin memory**
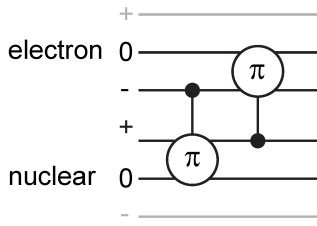
Figure 5.14.: PSWAP schematic.

Since only the states $|0\rangle$ and $|-\rangle$ are used in the correlation experiment, only a partial swap gate (PSWAP) is necessary to store the full information on a memory spin. With the use of the ^{14}N nuclear spin ($I = 1$), a PSWAP gate interchanging $|0, -\rangle$ and $|m_I = 0, +1\rangle$ was designed. The PSWAP gate can be further simplified, assuming the nuclear spin being completely polarized in $|m_I = +1\rangle$ before every measurement.

The pulse sequence used consists of one controlled nuclear spin rotation (control: $|-\rangle$) followed by a controlled electron spin rotation (control: $|m_I = +1\rangle$) as shown in Fig. 5.14. Please not that by addition of an additional controlled nuclear spin rotation the PSWAP gate is complete. However due to the polarized nuclear spin (^{14}N polarization larger then 0.9), the shorter pulse sequence is sufficient.

With a non-selective spin rotation, the electron spin can then be rotated into any desired spin state. In order to retrieve the stored information, the PSWAP gate has to be applied in reverse fashion.

Control implementation
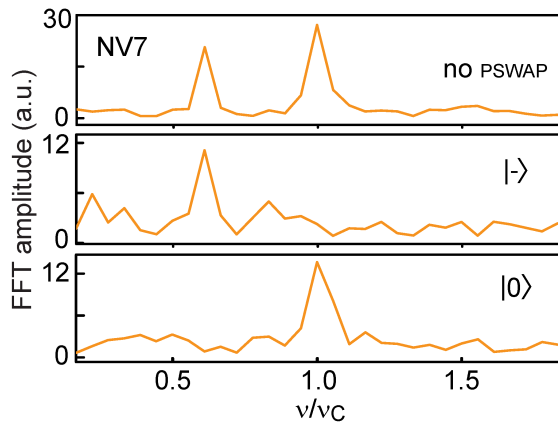
Figure 5.15.: Correlation evolution for different electron spin states. Without storing the information in the nuclear spin memory, two distinctive peaks at ν_C and $\nu_{hyperfine}$. With storage the evolution can be tailored to either $\nu_{hyperfine}$ for the electron being in the $|-\rangle\langle-|$ and ν_C for the $|0\rangle\langle0|$ state.

With the use of the PSWAP gate, now the electron spin population containing the bath information can be stored on the ^{14}N nuclear spin memory. The sequence for such a measurement is then given by $init - cor - pswap - (\pi) - \widetilde{\tau} - (\pi) - pswap^{-1} - cor - read$. The PSWAP is designed as such, that the NV electron spin is in the $|-\rangle\langle-|$ state after the PSWAP gate is applied. With optional electron spin rotation (π) the electron spin state can be controlled as desired.

In Fig. 5.15, the correlation spectrum of NV7 is shown. Without the PSWAP gate, two distinctive peaks given by the ^{13}C nuclear Zeeman effect ν_C for $|0\rangle\langle0|$

and $\nu_{hyperfine}$ for $|+\rangle\langle+|$. With PSWAP gate, the electron spin state is $|+\rangle\langle+|$, therefore a frequency of $\nu_{hyperfine}$ is observed. With an additional π pulse, $|0\rangle\langle0|$

leads to the an observed frequency of ν_C. This demonstrates the full control over the hyperfine interaction, allowing one to switch the interaction between ν_C and $\nu_{\text{hyperfine}}$ with electron spin rotations.

5.5. Conclusion

In this chapter, the interaction of the NV center with its surrounding spin bath was investigated. Here ultra clean samples provided by Element six were used, containing almost no other spin impurities besides ^{13}C [39]. Therefore the coherence properties are governed by the interaction with the ^{13}C spin bath. The inhomogeneous line width due to time averaging is given by the thermal occupation of all possible states of the spin bath, giving rise to $T_2^* \approx 3~\mu$s. If a simple decoupling protocol (Hahn echo) is used, the static inhomogeneous line width can be refocused, and the dephasing time $T_2 \approx 400 - 500~\mu$s becomes dependent on the ^{13}C spin flip-flop processes [13, 69, 71]. Alternatively, by isotopical engineering, the ^{13}C can be lowered, diluting the spin bath and allowing one to extend the coherence time to tens of microseconds for T_2^* and milliseconds for T_2 [15].

We first investigated the decoupling of the NV center from its spin bath. As a first approach, higher order dynamical decoupling protocols were implemented. With the use of the CPMG sequence, it was possible to suppress the spin noise to a high degree. This enhances T_2 from $T_{2\,\text{Hahn}} = 370 \pm 7~\mu$s to $T_{2\,\text{CPMG}} = 2.44 \pm 0.44$ ms. Please note, that the dephasing time achieved by dynamical decoupling is then comparable to that in isotopically purified samples. With a measured spin locking time of $T_{1\rho} = 2.47 \pm 0.27$ ms, giving the limit for dynamical decoupling, the maximal decoupling efficiency from the the spin bath was achieved. With a NV spin life time of $T_1 = 5.93 \pm 0.7$ ms, a decoupling ratio of $T_{2\,\text{CPMG}} = T_{1\rho} = \frac{1}{2}T_1$ was achieved, hinting at a limitation by the spin relaxation time.

But refocusing the spin noise is not the only option available to extend the coherence times. We also investigated tailoring the eigenstates of the NV center, such that they are not susceptible to magnetic fields in the first order. This is achieved by the mixing of the high field eigenstates $|\pm\rangle$ for a regime where strain σ is the dominant interaction ($\sigma \gg \gamma_e B$). In this case the interaction with magnetic field is vanishing in the first order and the NV is decoupled from magnetic field noise, such as the spin bath. A transition between the high strain regime with $T_{2\,\sigma}^* = 35.1~\mu$s and the high magnetic field regime $T_{2\,\text{high field}}^* = 3.0~\mu$s was observed. The enhancement of T_2^* by an order of magnitude is again comparable to isotopically pure samples. T_2^* is therefore not limited by the spin bath anymore, but instead by other noise sources, such as temperature, electric fields or phonons.

The demonstrated expansion of coherence times will have great impact in quantum metrology and quantum information applications. Longer coherence times can be directly translated into higher sensitives ($\eta \propto 1/\sqrt{T_{\text{coh}}}$, see Chapter 6.3.1). For quantum information processing, longer coherence times enable coherent coupling

to weakly coupled spins, allowing for larger distances between single nodes (see Chapter 7.2).

However, for quantum technologies, the spin bath does not necessarily have to be seen as a nuisance, but can be a resource as well. E.g. a nuclear spin register consisting of three nuclear spin with one central NV electron spin has been used to implement quantum error correction [18]. The use of weakly coupled ^{13}C would potentially extend the applications even further, e.g. making quantum error correction feasible on any NV. Unfortunately spectroscopy of distant ^{13}C nuclear spins is a nontrivial task [74, 75]. Therefore we developed a spectroscopy method based on creating a quantum coherence on the bath spin which are correlated to the electron spin state. We utilize electron spin dependent eigenframes of the ^{13}C to create controlled rotations on the nuclear spin, allowing us to create coherences even from a thermal state of the spin bath. These correlations can then, after a free evolution time, be mapped back into a detectable signal on the electron spin. During the free evolution period, the nuclear spin accumulates an electron spin dependent phase, allowing the determine the hyperfine spectrum. Since nuclear spin coherences correlated to electron spin states are used, the spectral resolution of this method is limited by the coherence time of the nuclear spin (limited by the electron spin relaxation time T_1). This allows in principle for a full spectroscopy of the spin bath. With the implementation of a simple PSWAP gate, the electron spin correlation was stored on the ^{14}N nuclear spin memory, allowing switching of the hyperfine interaction. With the use of decoupling schemes, like one demonstrated by Mauerer et al. in reference [19], the nuclear spin coherence time can be decoupled from the electron spin life time and making accuracies beyond T_1 possible.

6. Quantum metrology

6.1. Introduction

Nanoscale sensing is one of the most demanding tasks faced in modern sensing techniques. In order to achieve increasingly improved resolutions, sensor size has been reduced dramatically in recent years. As a consequent extrapolation of this trend, single atoms should yield the ultimate sensing resolution [1]. The fundamental interaction between magnetic fields (Zeeman effect) and electric fields (Stark effect) could be used to measure fields at the nanoscale.

Since atoms are notoriously difficult to handle, artificial atoms in a solid state matrix offer a reasonable substitution. Here the NV center in diamond is an exceptional system, due to the possibility of ground state ODMR with exceptionally long coherence times [61, 78]. Since the wave function of the electrons is believed to be distributed around the defect site [53, 54], one can in fact consider the NV center as an artificial molecule. The optical read out of a single NV [12], allows for unprecedented local field measurements with a position accuracy of a few angstroms. It is operational at ambient conditions, thus not limiting sensing applications to more exotic sensing environments like low temperature or vacuum. The long coherence time of the ground state spin (a few ms [15, 61]), in comparison to optical transitions (in the order of ns), allows for one to use even weak interactions and still gain high precision measurements. Here the interaction of the ground state electron spin ($S = 1$) with external fields yields a shift in the eigenenergies, which can be detected by spectroscopic means. E.g. the strong Zeeman interaction (almost identical to a free electron 28.8 GHz/T) can be exploited for magnetic field sensing [23, 79]. Either a direct observation of the line shift in an ODMR spectrum or a measurement based on a quantum phase evolution is used to determine the energy shift. The quantum phase evolution detects, similar to optical interferometry, a phase difference between a reference signal (microwave) and the Larmor frequency of the NV. Changes in the eigenenergies (i.e. a change in the applied field/temperature) can be detected by the phase of a coherent evolution. Since phase evolutions can be combined with dynamical decoupling (see Chapter 6.3.1), longer evolution times can be used to obtain higher sensitivity (similar to the Mach-Zehnder interferometer in optics).

But not only can the Zeeman interaction be exploited for precision measurements, but it is also possible to use the much weaker Stark effect for detection of electric fields. Due to the C_{3V} symmetry of the NV, the electron spin state is, in the first order, decoupled from electric fields, only spin-orbit coupling allows for a small electric field interaction (the LS coupling parameter is $\approx 10^{-4}$ [57]). This is still sufficient, since the charge of an electron at a nanoscale distance yields a line shift of 66 ± 7 kHz (see Chapter 6.5) while the magnetic dipolar interaction only yielded $\nu_{\mathrm{dip}} = 4.93 \pm 0.05$ kHz.

Therefore the NV center is multipurpose sensor allowing to measure nanoscale temperature, electric and magnet fields. Breakthrough experiments in the recent years in scanning probe magnetometry [79] lead to a well-established field for scanning probe magnetometry based on single NV centers [45, 80–82]. The low cytotoxicity of nanodiamonds [47] even allows the insertion into cells for sensing applications. Diffusion experiments with the nanodiamond as nonbleaching marker [48] as well as temperature measurements [49] have been carried out in cells. Also bulk measurements for low field NMR [83] as well as wide-field magnetic imaging [84, 85] were implemented. In order to increase the dynamic range, quantum phase estimation algorithms were implemented [86]. Measurements using nanodiamonds in cells [48, 49] promise a wide field of application in sub- cellular biology.

In this work, dynamical decoupling is introduced to magnetic field sensing, enhancing the sensitivity to be effectively limited by T_1 (see Chapter 6.3.1). The sensing capabilities were extended to electric fields (see Chapter 6.4) leading to the detection of a single fundamental charge at ambient conditions (see Chapter 6.5).

6.2. Concept of field measurements

The general concept of sensing using an artificial atom like the NV center is to detect the energy shift of eigenstates due to fundamental interactions, e.g. the Zeeman interaction can be used to detect magnetic fields. For the NV center, the ground state is the preferred state for this kind of analysis, due to its spin life time on the order of milliseconds, allowing for higher resolution (as explained below). The most basic sensing technique is to take an ODMR spectrum and thereby directly observe the energy difference between $|0\rangle$ and $|\pm\rangle$ as shown in Fig. 6.1. This technique has been used in the first scanning probe demonstration [79] and has been improved since then by feedback frequency control [87], multifrequency approaches [82] as well as other techniques. If the full spectrum is recorded the amplitude of B_z and $B_\perp$ can be determined absolutely. However the sensitivity is ultimately limited by the inhomogeneous broadening of the ESR transition given by T_2^*.
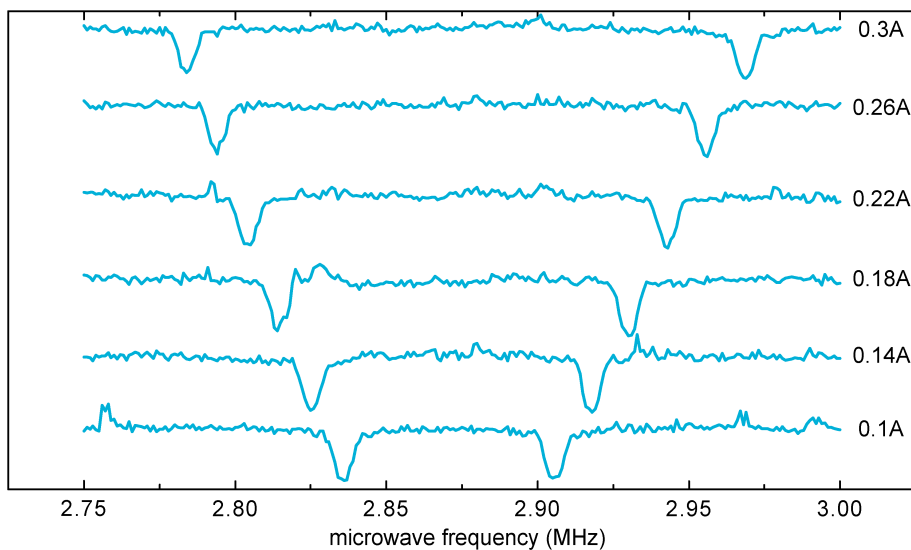
Figure 6.1.: Line shift example. ODMR spectra of the transition frequencies when a coil is placed close to the NV and its current linearly increased

A more advanced method to measure the energy level shift was introduced by Maze et al. in reference [23, 69]. Here the full quantum nature of the NV center is utilized to detect the line shift. For this a coherent superposition of the ground state spin triplet is utilized, e.g. created with a $\frac{\pi}{2}_+$ pulse applied on the polarized state $\psi_0 = |0\rangle$:

$$\psi(0) = \frac{1}{\sqrt{2}} \left(|0\rangle + |+\rangle \right). \tag{6.1}$$

Under free evolution for the time τ the coherent state evolves in the microwave

frame (see Chapter 4.3.1) is as:

$$\psi(t) = e^{-i2\pi\widetilde{H}\tau}\frac{1}{\sqrt{2}}\left(|0\rangle + |+\rangle\right) = \frac{1}{\sqrt{2}}\left(|0\rangle + e^{-i\phi}\,|+\rangle\right), \qquad (6.2)$$

where $\widetilde{H}$ is the ground state Hamiltonian in the microwave frame. Assuming a diagonal time-dependent Hamiltonian and the eigenenergy difference between $|0\rangle$ and $|+\rangle$ being $\nu_{\mathrm{Larmor}}(t)$, the phase ϕ is given by

$$\phi_{\mathrm{FID}} = 2\pi \int_0^\tau \nu_{\mathrm{Larmor}}(t) - \nu_{\mathrm{mw}}\, dt = 2\pi \int_0^\tau \Delta(t)\, dt \qquad (6.3)$$

Since ν_{Larmor} is directly proportional to the difference in eigenenergies, shift in the eigenenergies are detectable. The sensitivity of this Ramsey type sensing scheme is still limited by the inhomogeneous line broadening T_2^*.
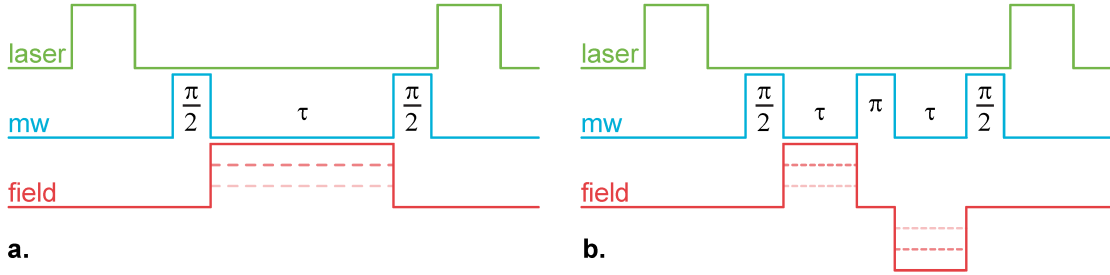
Figure 6.2.: Pulse sequences used to detect fields. a. FID based **b.** Hahn echo based. The field to sense is applied in phase with the detection sequence.

In order to achieve longer sensing times and therefore higher sensitivities, dynamical decoupling can be integrated into the phase measurement sequence [23, 69]. The fundamental working principle of dynamical decoupling is however, to decouple the observed coherence from inhomogeneous broadening by refocusing static energy shifts (see Chapter 5.2). Therefore the sensing sequence becomes insensitive to static interactions (DC) and is only susceptible to fluctuating interactions (AC) that are locked to its detection frequency given by the pulse sequence (see Fig. 6.2). The accumulated phase can be described for the simplest dynamical decoupling sequence (Hahn echo) by

$$\phi_{\mathrm{Hahn}} = 2\pi \int_0^\tau \Delta_{\mathrm{mw}}(t)\, dt - 2\pi \int_\tau^{2\tau} \Delta_{\mathrm{mw}}(t)\, dt. \qquad (6.4)$$

Static shifts are now not detectable anymore and only frequencies locked to the decoupling sequence are observable [88].

However decoupling allows for significantly longer phase accumulation times increasing the detection sensitivity significantly (see reference [23, 78] and

Chapter 6.3.1). Additionally the decoupling allows for tailoring the sensitivity profile, that lock-in detection of an external signal is possible. This lock-in technique has recently been used to detect hydrogen outside of diamond either by locking the detection frequency to driven spin dynamics of the hydrogen [89] or by tuning the lock-in frequency to the hydrogen Larmor frequency [44] enabling nanoscopic MRI experiments outside of diamond. Also in Chapter 7.4.1, the lock-in detection is used to apply dynamical decoupling while still having a coherent phase evolution due to the other spin, enabling high fidelity entangled states.

In order to compare the NV sensor to other systems, the sensitivity has to be analyzed. For NV based sensors, the minimal detectable line shifts are ultimately governed by photon shot noise of the spin state detection [20, 23]. A single transition energy can be determined with arbitrary accuracy. Since the desired information is encoded in photon intensity and photon detection is a stochastic process, the precision scales with $\eta \propto 1/\sqrt{N_{\mathrm{photon}}}$ (photon shot noise limit), where N_{photon} is the number of detected photons. Therefore, the accuracy improves with the number of measurements N_{meas} by $\eta \propto 1/\sqrt{N_{\mathrm{meas}}}$ [20, 23]. With the improvement of the photon detection efficiency (e.g. by using solid immersion lenses [90] or nano-pillars [81]) the sensitivity scales as $\eta \propto 1/\sqrt{countrate}$. For quantum metrology schemes, the sensitivity is also dependent on the phase accumulation time τ. Since the detected phase scales linearly with τ, but the measurement repetition rate is inversely proportional to the square root of τ_{evo}, $\eta \propto 1/\sqrt{\tau_{\mathrm{evo}}}$. τ_{evo} is limited by the coherence time τ_{coh}, giving a maximal sensitivity scaling of $\eta_{\mathrm{max}} \propto 1/\sqrt{\tau_{\mathrm{coh}}}$. By using the double quantum state (see A.8) the sensitivity can be enhanced by $\sqrt{2}$ [91] (the same phase is collected in half the time, coherence times are half as well). Also the utilization of a small quantum register with single shot read out capabilities [28] should increase the achievable sensitivities.

The use of ensembles can improve the measurement accuracy by $\eta \propto 1/\sqrt{N_{\mathrm{NV}}}$, since more photons per measurement are collected. Using entangled or squeezed states, the sensitivity increases linearly [37, 38, 92].

6.3. Magnetometry

For magnetometry, the Zeeman effect of the electron spin ground state is utilized. The interaction Hamiltonian, neglecting strain and hyperfine interaction, is given by

$$H = DS_z^2 + \gamma_e \underline{B}\,\underline{S} \tag{6.5}$$

If the zero field splitting D is known, a measurement of the transition energies allows for the calculation of the axial magnetic field B_z as well as the orthogonal magnetic field $B_\perp$. This makes the NV an absolute magnetometer, allowing the determination of the magnetic field as an absolute value. Please note that, while giving the absolute value, the direction of the magnetic field cannot be obtained without ambiguity. The ambiguity can be lifted by applying three non-parallel know calibration magnetic fields.

The simplest form of magnetometry is a plain ODMR spectrum, where the response of the NV center is measured by scanning a CW microwave field to probe the transition frequencies. The contrast and speed can be further improved by applying a pulsed scheme, where the microwave is switched on for the length of a π pulse maximizing the contrast signal and negating line broadening due to the laser power [63, 93]. The pulse scheme is $(\pi - t_{\text{laser}} - t_{\text{wait}})^\infty$, where $t_{\text{laser}} = 300$ ns is the laser illumination time containing the spin state information (see Chapter 4.1) and $t_{\text{wait}} = 1.5\ \mu$s is the waiting time required for depopulation of the metastable shelving state. This pulse sequence speeds up the spectroscopy by orders of magnitude (by standard CW means a hyperfine resolved spectrum is taken in the course of several tens of minutes while for the pulsed scheme a spectrum can be obtained in a few seconds). A typical spectrum based measurement is shown in Fig. 6.1, which was used to calibrate the magnetic field coils of the setup. Spectrum based meteorology with fitting of the Hamiltonian (with the knowledge of D) was used throughout this work to determine the local magnetic field amplitude in the axial and nonaxial direction.

6.3.1. Magnetic field measurement with dynamical decoupling

With pulsed schemes, the sensitivity of magnetic field measurements can be enhanced. Dynamical decoupling methods like CPMG [16, 17] allows for the extension of the coherence time to $T_{1\rho}$ (see Chapter 5.2.2). Since the sensitivity improves with longer coherence times as $\eta \propto \sqrt{T_{\mathrm{coh}}}$, higher sensitivities are expected using dynamical decoupling.
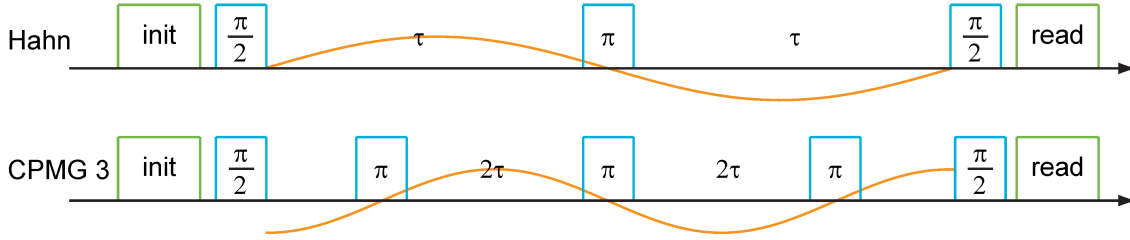
Figure 6.3.: AC magnetometry pulse sequences. The AC magnetic field (indicated by the orange line) is matching the evolution time τ in phase and frequency.

$D = 2.87$ GHz is generally orders of magnitudes larger than magnetic field interactions. Therefore, in the first order, only magnetic fields along the NV axis B_z are detected ($B_\perp$ only leads to a small quadratic shift). The detuning of the eigenenergies are given by $\delta\nu = \gamma_e \delta B_z(t)$. Therefore the collected phase is given by

$$\delta\phi_{\mathrm{FID}} = 2\pi \int_0^\tau \delta\nu dt = 2\pi\gamma_e \int_0^\tau \delta B_z(t)dt \tag{6.6}$$

and

$$\delta\phi_{\mathrm{Hahn}} = 2\pi\gamma_e \left(\int_0^\tau \delta B_z(t)dt - \int_\tau^{2\tau} \delta B_z(t)dt \right) \tag{6.7}$$

With higher order CPMG sequences (see figure 6.3) the collected phase is given by

$$\delta\phi_{\mathrm{CPMG}} = 2\pi\gamma_e \Big(\int_0^\tau \delta B_z(t)dt + \sum_{N=1,3,5,\dots} \int_{(2N-1)\tau}^{(2N+1)\tau} \delta B_z(t)dt$$
$$- \sum_{N=2,4,6,\dots} \int_{(2N-1)\tau}^{(2N+1)\tau} \delta B_z(t)dt + (-1)^N \int_{(2N+1)\tau}^{(2N+2)\tau} \delta B_z(t)dt \Big)$$

Where N is the order of the CPMG sequence (see Chapter 5.2.2). As discussed in Chapter 5.2, dynamical decoupling refocuses static fields. Therefore, only fluctuating fields (AC) can be sensed using dynamical decoupling. In order to detect the strongest signal, phase and frequency of the applied AC magnetic field has to match $\frac{1}{2\tau}$ for a Hahn echo and $\frac{1}{4\tau}$ for higher orders of CPMG (see Fig. 6.3). Since dynamical decoupling allows for two to three orders of magnitude longer coherence times, the expected sensitivity ($\eta \propto \sqrt{\tau_{\mathrm{evo}}}$) is increased.
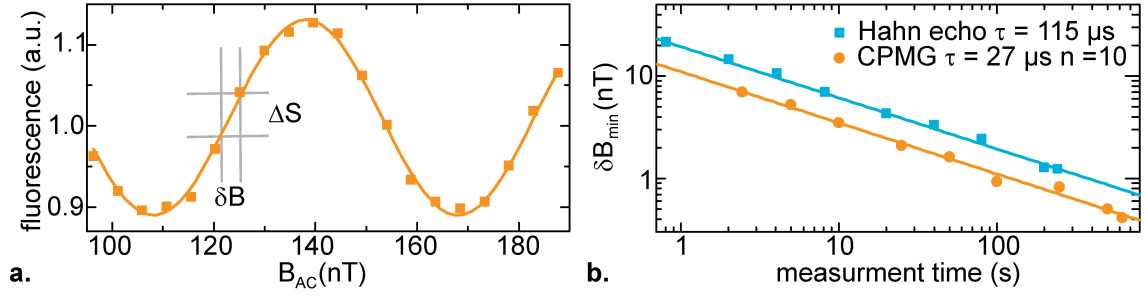
Figure 6.4.: Shotnoise noise limited sensitivity. a. Typical fluorescence response for the decoupling based magnetic field sensing and a ramped magnetic field. The highest sensitivity can be obtained at the maximum slope. **b.** δB_{min} as a function of the total measurement time per data point is shown (Hahn echo blue squares and CPMG orange circles). The lines are fits with the shot noise limit $\delta B_{min} = \frac{\eta}{\sqrt{t}}$.

In order to investigate the sensitivity η, the measurement accuracy given by the smallest detectable magnetic field difference δB_{min} has to investigated in regards to total measurement time. δB_{min} is determined by the change of the measured signal in regard to a magnetic field change and the measurement error of the signal S. The steepest change in the signal is considered for maximum sensitivity. The error in the signal amplitude S is given by the shot noise limitation of the collected photons. δB_{min} can be calculated by

$$\delta B_{min} = \frac{\sigma_{sn}}{\delta S} \tag{6.8}$$

where σ_{sn} is the uncertainty in the measured data point (determined by the standard deviation) and $\delta S = \frac{\Delta S}{B}$ is the derivative of the signal (see Fig. 6.4a). The dependence of δB_{min} on σ_{sn} is depicted in Fig. 6.4b. $\tau = 115$ μs was chosen for the Hahn echo based method. For the CPMG detection scheme $N = 10$ and $\tau = 27\mu s$ was used. Unfortunately, increasing the number of pulses above ten did not improve the sensitivity, probably due to fluctuations in the applied AC magnetic field. Nevertheless with the CPMG technique we were able to significantly reduce δB_{min} (see Fig. 6.4). The fit of the shot noise limit $\delta B_{min} = \frac{\eta}{\sqrt{t}}$ yields a sensitivity of $\eta_{Hahn} = 19.4 \pm 0.4 \frac{nT}{\sqrt{Hz}}$ and $\eta_{CPMG} = 11.0 \pm 0.2 \frac{nT}{\sqrt{Hz}}$. The minimal detected δB_{min} is then $\delta B_{min}^{Hahn} = 1.2$ nT and $\delta B_{min}^{CPMG} = 0.4$ nT.

In summary we have demonstrated that by increasing the coherence time of a single NV center with help of CPMG, improved sensitivity compared to the Hahn echo method is possible. Additionally CPMG allows to tailor the detection frequency ($\nu_{\text{detect}} = \frac{1}{4\tau}$), allowing for look-in detection methods, i.e. to detect external nuclear spins like hydrogen [44].
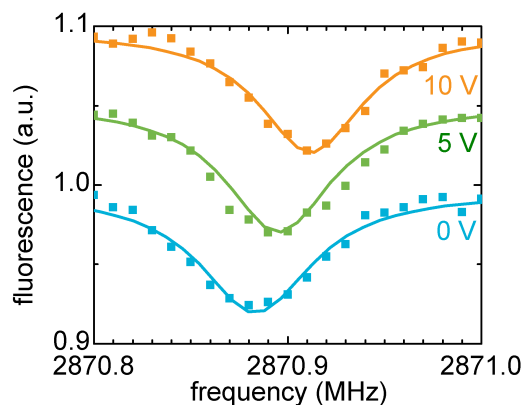
6.4. The NV as a nanoscale electrometer

Detecting electric fields with a nanoscale probe such as the NV center at ambient conditions yield a broad field of potential applications. Existing methods so far are limited to low temperatures, e.g. single-electron transistors [94–96], electrostatic force or capacity based scanning probes [97–99] and scanning tunneling microscopy [100]. Here the NV center is a unique system, allowing for multidimensional sensing not only of magnetic fields [15, 20, 23, 44, 101] and temperature [22, 49, 102, 103], but also electric fields. A linear Stark effect in the ground state

Figure 6.5.: Electric field response of the NV. Here an ODMR signal is shown while increasing the voltage at the electrodes. The linear energy shift of the ODMR transition in response to the applied electric field is clearly visible.

[104], first demonstrated in an ensemble measurement by Van Oort et al. [21], is used to detect electric fields. The electric field coupling constants are given by

$$k_\perp = 0.17 \pm 0.03 \ \frac{\text{Hz m}}{\text{V}}, \ k_\parallel = 0.0035 \pm 0.0002 \ \frac{\text{Hz m}}{\text{V}}, \qquad (6.9)$$
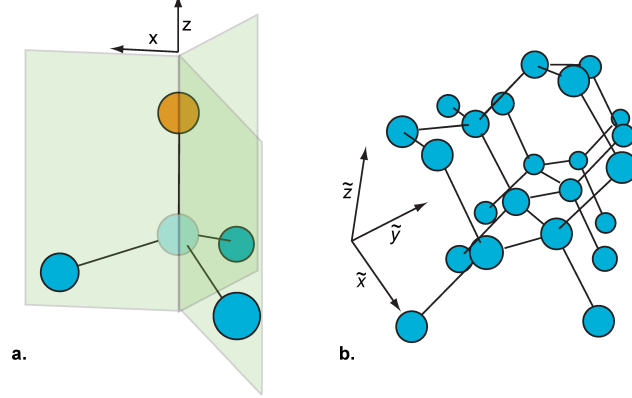
where $k_\perp$ is the coupling constant for electric fields orthogonal to the NV symmetry axis and $k_\parallel$ for the parallel ones. The coupling of electric fields to the NV ground state is rather weak, however electric fields of a fundamental charge are large in comparison to the magnetic field of the attributed spin (see Chapter 6.5). Therefore electric field sensing with potentially single charge resolution at ambient conditions have a wide range of applications in biology or material science applications.

Here we demonstrate the sensing of electric fields utilizing the long coherence times of the NV center. For this proof of principle experiment, we used a CVD grown bulk sample with low nitrogen content (>4 ppb) and natural ^{13}C concentration. Electrodes were fabricated by lithographic means on top of the diamond surface allowing for a controlled application of an electric field. In Fig. 6.5 the line shift of an NV resonance for different electric fields is shown. Magnetic field coils were placed around the setup.

6.4.1. The electric field Hamiltonian

Figure 6.6.: NV coordinate systems. a. The NV coordinate system where z is along the symmetry axis and x along one carbon bond. The blue spheres symbolize carbons, the orange nitrogen and the faded sphere stands for the vacancy. **b.** Lab coordinate frame used for a (100) sample, as used in this work. Due to the crystal orientation the NV coordinate axis y corresponds to the $\widetilde{x}$ or $\widetilde{y}$ lab coordinate axis (dependent on the NV orientation).

Pure spin states are, in the first order, not susceptible to electric field changes. Only spin-orbit coupling allows for a detectable Stark effect [104]. For the NV center, the large Stark effect of the optical transition [41], is coupled with a weak spin orbit coupling to give rise to a linear Stark effect of the ground state electron spin state [105]

The electric field Hamiltonian was derived from molecular orbit theory by Doherty et al. in reference [57]. It is equivalent to the established effective spin Hamiltonian for the C_{3V} point symmetry group [21, 104]:

$$H_E = (D + k_\parallel \Pi_z)S_z^2 + \gamma_e \underline{S} \cdot \underline{B} - k_\perp \Pi_x (S_x^2 - S_y^2) + k_\perp \Pi_y (S_x S_y + S_y S_x) \quad (6.10)$$

where $\underline{S}$ are the $S = 1$ electron spin operators, γ_e is the gyromagnetic ratio and $\underline{B}$ is the magnetic field. Strain $\underline{\sigma}$ and the electric field $\underline{E}$ can be treated as an effective field $\underline{\Pi} = \underline{E} + \underline{\sigma}$ [41]. The spin coordinate system is defined such, that the z coordinate axis coincides with the center's trigonal symmetry axis and the x axis is contained in one of the center's mirror planes (along a carbon bond, see figure 6.6).

If a high axial magnetic field is present ($\gamma_e \underline{B} \gg k_\perp \underline{\Pi}_\perp$), the eigenstates of the NV Hamiltonian correspond to the eigenstates of the S_z operator and are labeled $|0\rangle$ and $|\pm\rangle$ for $m_S = 0, \pm 1$. In the absence of an axial magnetic field ($\gamma_e \underline{B} = 0; k_\perp \underline{\Pi}_\perp > 0$),

the NV eigenstates change to

$$|E_0\rangle = |0\rangle$$
$$|E_\pm\rangle = \tfrac{1}{\sqrt{2}} \left(e^{-i\frac{\phi_\Pi}{2}} |+\rangle \pm e^{i\frac{\phi_\Pi}{2}} |-\rangle \right) \tag{6.11}$$

with $\phi_\Pi = \tan\left(\frac{\Pi_y}{\Pi_x}\right)$. The linear combination of the S_z eigenstates leads to a vanishing expectation value for the spin operator $\langle S_z \rangle$, suppressing Zeeman interaction in the first order as long as $k_\perp \underline{\Pi}_\perp \gg \gamma_e B_z$ is valid. This leads to different decoherence regimes as demonstrated in Chapter 5.3.

For electric field detection, the nonaxial Stark effect is preferable to the axial, due to the stronger interaction constant ($k_\perp \approx 50 k_\parallel$). Therefore the Hamiltonian is analyzed in regard to $\Pi_\perp$. Considering fixed magnetic and strain fields, the change in the Larmor frequency $\delta\nu$ due to a small change of the electric field $\underline{E}$ is given by perturbation theory

$$\delta\nu_\pm = k_\parallel E_z \pm [f(\underline{B}, \underline{E}, \underline{\sigma}) - f(\underline{B}, 0, \underline{\sigma})] \tag{6.12}$$

with

$$f(\underline{B}, \underline{E}, \underline{\sigma}) = \left[(\gamma_e B_z)^2 + (k_\perp \Pi_\perp)^2 - \frac{\gamma_e^2 B_\perp^2}{D} k_\perp \Pi_\perp \cos\left(2\phi_B + \phi_\Pi\right) + \frac{\gamma_e^4 B_\perp^4}{4D^2} \right]^{\frac{1}{2}} \tag{6.13}$$

and $\Pi_\perp = \sqrt{\Pi_x^2 + \Pi_y^2}$, $B_\perp = \sqrt{B_x^2 + B_y^2}$ and $\phi_B = \tan\left(\frac{B_y}{B_x}\right)$.

Assuming no perpendicular magnetic field ($B_\perp = 0$), Eq. (6.12) simplifies to

$$f(\underline{B}, \underline{E}, \underline{\sigma}) = \left[(\gamma_e B_z)^2 + (k_\perp \Pi_\perp)^2 \right]^{\frac{1}{2}} \tag{6.14}$$

Only if the effective electric field interaction is larger than the axial magnetic field interaction, a reasonable line shift due to electric fields is detectable. Therefore it is essential that B_z is precisely controlled in order to have the maximal Stark effect (measurements are shown in Chapter 6.4.3). Additionally, for high strain color centers, the magnetic field compensation becomes less imperative, since the effective field $\underline{\Pi}_\perp$ is responsible for the suppression of B_z. With high strain, the electric field is projected on the strain axis allowing only detection electric fields along this axis.

Another interesting sensing regime is no axial magnetic field ($B_z = 0$) and a perpendicular magnetic field larger than the effective electric field ($\gamma_e B_\perp \gg k_\perp \Pi_\perp$). Here, only considering the dominant interaction given by $B_\perp$, the eigenstates of the

NV are given by

$$|B_0\rangle = n_1 \left(-e^{2i\phi_B} \, |+\rangle + \frac{i(D + \sqrt{4b^2 + D^2})e^{i\phi_B}}{\sqrt{2B^2}} \, |0\rangle + |-\rangle \right)$$

$$|B_-\rangle = n_2 \left(e^{2i\phi_B} \, |+\rangle + |-\rangle \right) \tag{6.15}$$

$$|B_+\rangle = n_3 \left(-e^{2i\phi_B} \, |+\rangle + \frac{i(-D + \sqrt{4b^2 + D^2})e^{i\phi_B}}{\sqrt{2B^2}} \, |0\rangle + |-\rangle \right)$$

where $n_{1,2,3}$ are normalization factors, $b = \gamma_e B_\perp$, and the eigenenergies are $\frac{D - \sqrt{4b^2 + D^2}}{2}$, D and $\frac{D + \sqrt{4b^2 + D^2}}{2}$.

Analyzing Eq. (6.13) for $\gamma_e B_\perp \gg k_\perp E_\perp$ and $B_z = 0$ and omitting the line shifts purely due to the magnetic field, the electric field interaction becomes dependent on the the electric ϕ_E and the magnetic field ϕ_B orientation given by $f \propto \cos(2\phi_B + \phi_\Pi)$.
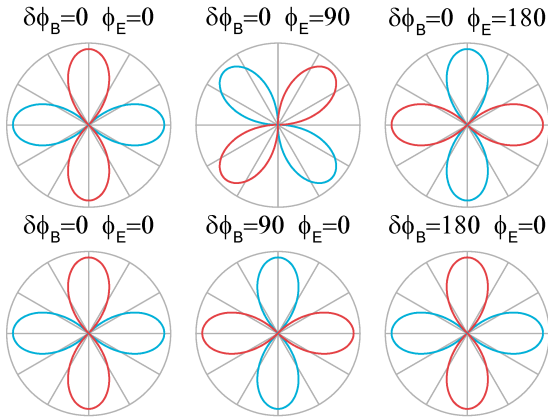

Figure 6.7.: **Theoretical calculation of electric field susceptibility vs.** $\underline{B_\perp}$ **orientation.** A large $B_\perp$ is rotated around the symmetry axis by $\phi_B = \delta\phi_B + \theta$, where $\delta\phi_B$ is the angle between the NV coordinate system and the rotation coordinate system θ. The electric field orientation is considered constant and given by ϕ_E. The blue lines correspond to a positive shift and the red lines to a negative.

This allows, in principle, the sensing of all components of the electric field vector using one NV center. A magnetic field rotation produces a characteristic 'four-leaf' pattern (see Fig. 6.7). However without knowledge of the crystal structure, i.e. the directions of the carbon bonds, only a relative change in the electric field orientation is obtainable. With knowledge of the alignment of $B_\perp$ towards the carbon bonds, which is the case if the diamond lattice orientation in the laboratory frame is known, the orientation of $E_\perp$ can be determined up to a 180° unambiguity. Knowing the transverse orientation of $B_\perp$ with respect to the trigonal structure of the NV center allows the determination of the transverse orientation of ϕ_E completely [68, 106].

6.4.2. Measurement implementation and photon shot noise limited sensitivity
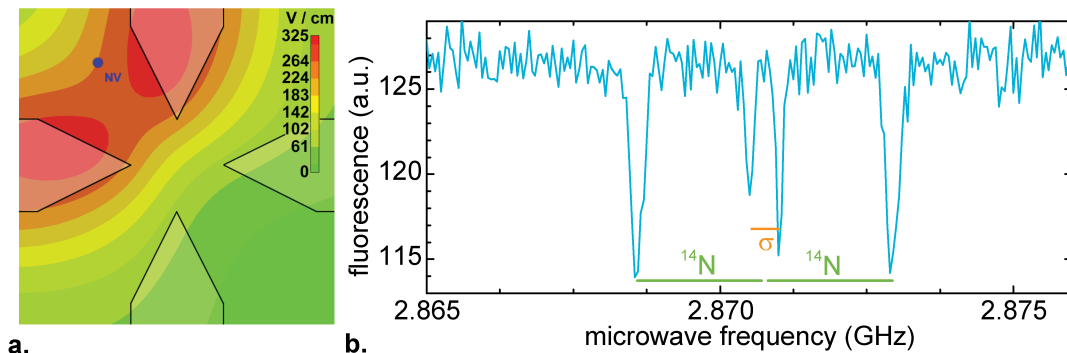
Figure 6.8.: Measurement configuration. a. Simulated electric field amplitude for 1 V voltage difference between the tips at a depth of the NV (6 μm). **b.** ODMR spectrum at ≈ 0 B_z. The spectrum is split by hyperfine interaction with ^{14}N by approx. 2.2 MHz. For $m_I = 0$ the strain σ is not suppressed by the hyperfine interaction and becomes visible.

Since $k_\perp$ is about fifty times larger than $k_\parallel$, we will try to detect the electric field component perpendicular to the symmetry axis. As discussed in Chapter 6.4.1, the nonaxial electric field interaction is highly susceptible to the NV spin state. Only eigenstates commuting with the electric field term show significant interaction. Since the S_z type axial magnetic field interaction suppresses these eigenstates, it is imperative to work at zero axial magnetic fields. As shown in Fig. 6.8b the hyperfine interaction with the ^{14}N also has a strong $a_\parallel$, component suppressing electric field interaction (i.e. strain) for $m_I = \pm 1$. But for $m_I = 0$, the electric field interaction is not suppressed and a strain of $\sigma = 189$ kHz becomes visible. In order to negate the effect of the hyperfine interaction, we only work with the spin subspace corresponding to ^{14}N being in $m_I = 0$. This reduces the signal by a factor of three and thereby also the achievable sensitivity. However with the application of nonaxial magnetic fields or higher strain, the hyperfine interaction can be suppressed and the full sensitivity reclaimed (see Chapter 6.4.3 and 6.5.1).
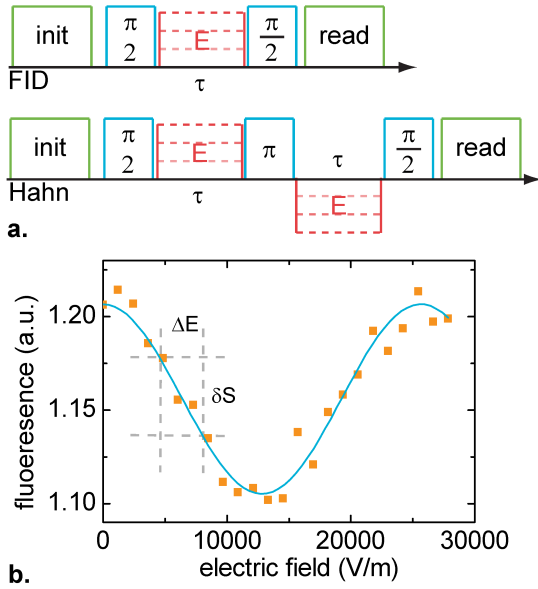
We performed the electric field measurements with coherent evolutions of superposition states (e.g. $|0\rangle + |1\rangle$) for a time τ. As described in Chapter 6.2, the collected phase for a free evolution is given by

$$\phi_{\text{E FID}} = 2\pi \int_0^\tau \delta\nu_{\text{Larmor}}(t)dt = 2\pi \int_0^\tau k_\perp \delta E_\perp(t)dt \qquad (6.16)$$

for a DC type Ramsey experiment and

$$\phi_{\text{E Hahn}} = 2\pi \int_0^\tau k_\perp \delta E_\perp(t)dt - 2\pi \int_\tau^{2\tau} k_\perp \delta E_\perp(t)dt \qquad (6.17)$$

for an AC Hahn echo measurements assuming $\underline{B} = 0$. The evolution time τ was kept constant and the applied electric field $\underline{E}$ was increased in linear steps (by increasing the voltage difference between the tip electrodes, lithographically fabricated on-top of the diamond see A.2). In Fig. 6.9, the change of the phase (signal $\propto \cos(\phi)$) with raising electric field with $\tau = 80$ μs is shown. The observed signal corresponds well with numerical simulations of the tip structutre at the depth of the NV center (depth≈ 6 μm) shown in Fig. 6.8. Please note that a change of the total electric field ($\underline{\Pi}_\perp = \underline{\sigma}_\perp + \underline{E}_\perp$) is observed if no nonaxial magnetic field is present. Only the amplitude of the electric field vector is detected. In case of our measurement, luckily $\underline{\sigma}_\perp$ and $\underline{E}_\perp$ showed a similar alignment (the observed maximal response of the NV center to an applied electric field was almost identical with and without nonaxial magnetic field).

Figure 6.9.: Electric field measurement sequence and signal. a. Measurement sequence used to detect electric fields. For a constant τ the applied electric field is increased. The FID scheme is used for DC fields while the Hahn echo sequence is used to measure AC fields. **b.** A coherent state is evolving for a time $\tau = 80$ μs. During τ rising electric fields are applied. The linear response of the phase (signal $\propto \cos\phi$) is clearly visible.

Therefore the zero magnetic field regime can be used to determine the electric field sensitivity. As described in Chapter 6.3.1, we determine the minimal detectable field $\delta E_{\min}$ at the most sensitive point (steepest point of the detected signal) for the evolution time τ giving the highest sensitivity (DC: $\tau = 8$ μs, AC: $2\tau = 160$ μs) given by the coherence time ($T_2 = 304 \pm 36\mu$ s). $\delta E_{\min}$ is given by

$$\delta E_{min} = \frac{\sigma_{sn}(t)}{\delta S_{max}} \qquad (6.18)$$

where δS_{max} is given by the maximal change of the signal $S = \frac{\delta S}{\delta E}$ (see Fig. 6.9) and σ_{sn} is the measurement accuracy given by the photon shot noise limit.

To investigate the time dependence of δE_{min} a measurement was run continuously while storing the measured data in a periodic interval (30 s). In order to determine $\sigma_{sn}(t)$, the data set with the longest measurement time was fitted to obtain a reference curve. This fit was then used to calculate $\sigma_{sn}(t)$ as the standard deviation for different measurement durations. With equation 6.18

the minimal detectable electric field was calculated as shown in figure 6.10. As a reference, the AC sensitivity allows the detection of a single elementary charge at a distance of 35 nm with a signal to noise ratio better than 1000 for an averaging time of 100 seconds.
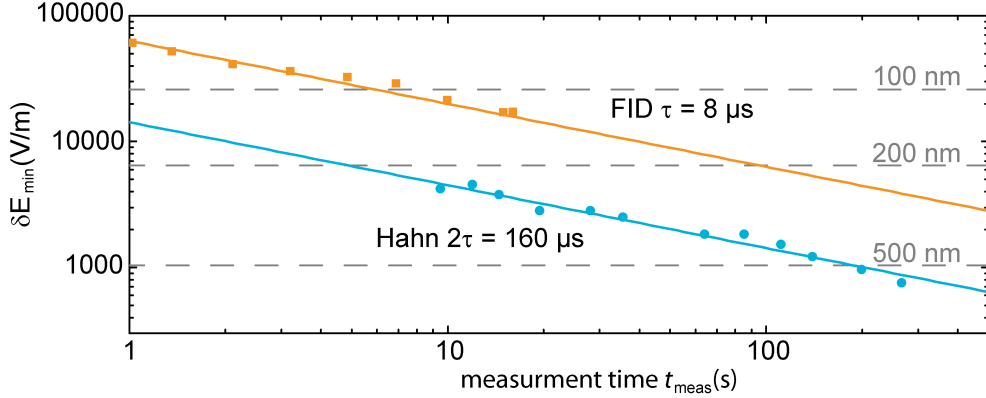
Figure 6.10.: Shot noise limited accuracy. Here the minimal detectable electric fields scaling with the measurement time is shown. The orange data correspond to the DC measurement using a FID scheme while the blue data is the AC measurement using a Hahn echo. The straight lines represent the fit with the photon shot noise limit. The grey dashed lines are the electric fields of a single fundamental charge at the indicated distance.

With fitting the photon shot noise limit

$$\delta E_{min} = \frac{\eta}{\sqrt{(t_{\mathrm{meas}})}} \tag{6.19}$$

where η is the achieved sensitivity and t_{meas} is the total measurement time per data point, the sensitivity η can be determined. For the investigated NV center a DC electric field sensitivity, using a FID based measurement scheme, of $\eta_{\mathrm{FID}} = 631.1 \pm 15.1 \, \frac{\mathrm{V}}{\mathrm{cm}\sqrt{\mathrm{Hz}}}$ was demonstrated. For AC electric fields, with a Hahn echo based measurement, a sensitivity of $\eta_{\mathrm{Hahn}} = 142.6 \pm 3.6 \, \frac{\mathrm{V}}{\mathrm{cm}\sqrt{\mathrm{Hz}}}$ was measured. Similar to magnetometry, the AC electric field can be further improved by using cleaner samples [78], by increasing the photon collection efficiency or using more advanced pulse sequences like CPMG as demonstrated for magnetometry in Chapter 6.3.1.

6.4.3. Electric field interaction and axial magnetic fields

As stated in Chapter 6.4.1 the eigenstates suitable for electric field detection are highly susceptible to axial magnetic fields B_z. If in Eq. (6.13) only B_z, a finite strain $\underline{\sigma}_\perp$ and a nonaxial electric field $\underline{E}_\perp$ are considered, Eq. (6.13) simplifies to

$$f(B_z, \underline{E}, \underline{\sigma}) = \left[(\gamma_e B_z)^2 + (k_\perp \underline{\Pi}_\perp)^2 \right]^{\frac{1}{2}} \tag{6.20}$$

In order to probe the interaction strength dependence on the magnetic field, a Hahn echo based electric field measurement was conducted. The frequency of the detected oscillation (see Fig. 6.9) was used as to investigate the interaction strength (normalized to the highest frequency).
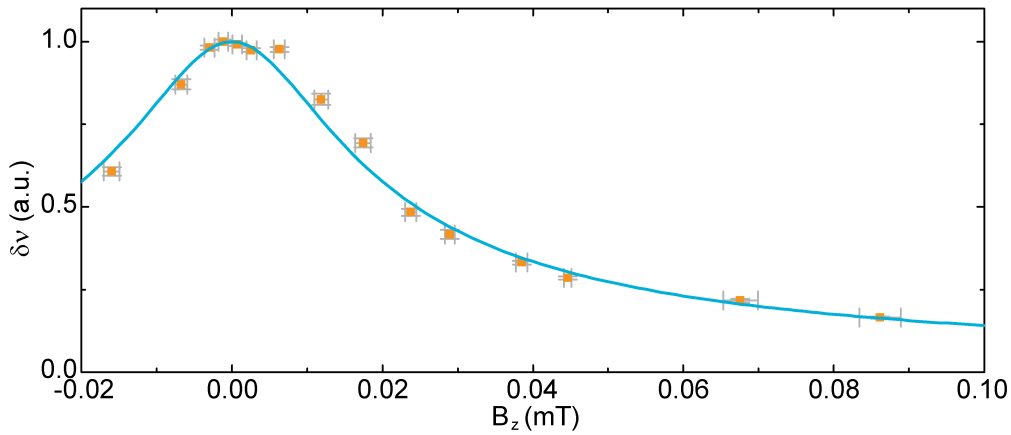
Figure 6.11.: Electric field interaction strength vs. axial magnetic field. Measured interaction dependence between an orthogonal electric field and an applied B_z field. The orange squared are measured data points and the blue line is data derived from simulating the electric field interaction with the measured magnetic field and strain.

In figure 6.11 the interaction dependence on the magnetic field is shown. With the measured strain of σ=187 kHz, the interaction coefficient was simulated. From the data one can see it is imperative to align the magnetic field carefully to avoid axial components. Otherwise the nonaxial electric field effect is suppressed.

However the amplitude of the absolute electric field $\underline{\Pi}_\perp$ governs the decay of the susceptibility. Therefore with higher strain (e.g. in nanodiamonds a strain of a few MHz is common), residual magnetic fields such as the earth's magnetic field $B_{\text{earth}} \approx 60 \ \mu\text{T}$ can be suppressed. An interpretation of such data is challenging since with $\underline{\Pi}_\perp = \underline{E}_\perp + \underline{\sigma}_\perp$, a large strain would define the sensing axis and from a weak electric field only the projection on this axis will be detectable.

6.4.4. Interplay between electric and nonaxial magnetic fields

If a strong nonaxial magnetic field $\underline{B}_\perp$ is applied, the eigenstate susceptibility to electric fields becomes dependent on the magnetic field orientation $\tan(\phi_B) = \frac{B_y}{B_x}$ and the electric field orientation $\tan(\phi_E) = \frac{E_y}{E_x}$. The x axis is defined along a bond to one of the three adjacent carbons.

Assuming no axial magnetic field ($B_z = 0$), Eq. (6.13) simplifies to

$$f(\underline{B}, \underline{E}, \underline{\sigma}) = \left[(k_\perp \Pi_\perp)^2 - \frac{\gamma_e^2 B_\perp^2}{D} k_\perp \Pi_\perp \cos\left(2\phi_B + \phi_\Pi\right) + \frac{\gamma_e^4 B_\perp^4}{4D^2} \right]^{\frac{1}{2}}. \qquad (6.21)$$

With a strong axial magnetic field ($\gamma_e B_\perp \gg k_\perp \Pi_\perp$), the interaction strength becomes proportional to $\delta f(\underline{B}, \underline{E}, \underline{\sigma}) \propto \cos\left(2\phi_B + \phi_E\right)$. This allows for the detection of the orientation of the electric field vector $\underline{E}_\perp$. Please note, that for these measurements $\underline{\sigma}$ was constant and therefore only changes in $\underline{E}_\perp$ were detected.

The detection scheme used is based on a Hahn echo ($\frac{\pi}{2}_x - \tau - \pi_x - \tau - \frac{\pi}{2}_x$), so only the amplitude of the field change is detected. This is due to the fact that the observed signal is proportional to $\cos\phi$ ($\cos\phi$ being symmetric to $\phi = 0$). As demonstrated by Michl et al. [68], this can be compensated by shifting the phase of the last $\frac{\pi}{2}$ pulse by 90°, making the signal proportional to $\sin\phi$, enabling the sign detection of the energy shift.

In order to investigate the electric field orientation ϕ_E, the interaction strength was probed at different magnetic field orientations ϕ_B. Here the laboratory coordinate system θ was defined such that for $\theta = 0$, $B_\perp$ is aligned along the NV (100) surface and therefore along $\pm y$ in the NV coordinate system. With rotating $B_\perp$ around the NV axis, a "four-leaf" pater was recorded. The measured pattern is shown in Fig. 6.12.
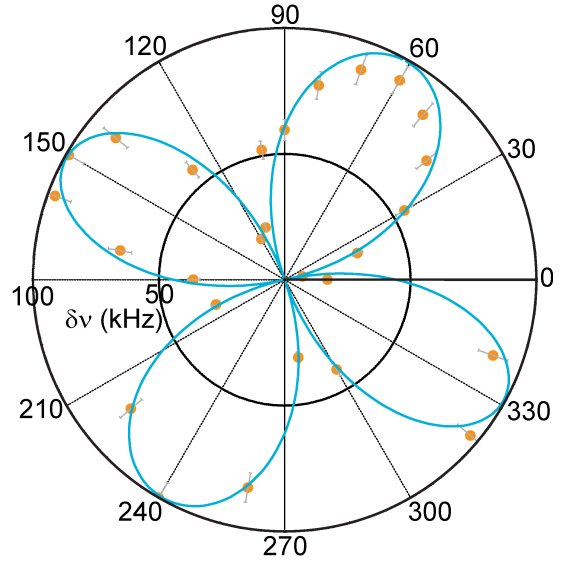

Figure 6.12.: Measured electric field susceptibility vs. $\underline{B}_\perp$ orientation. For a constant $\underline{E}_\perp$ a large $\underline{B}_\perp = 2.36 \pm 0.15$ mT is rotated around the NV axis. Due to the phase angle of zero between the $\frac{\pi}{2}$ pulses (see Fig. 6.9), only the absolute magnitude of the electric field effect is detected. $\underline{B}$ is rotated in the laboratory frame, where an angle of zero corresponds to $\underline{B}$ being in the (100) surface plane. In NV coordinates this corresponds to the y axis.

With knowledge of the NV axis orientation [68], the full vector of the electric field is determinable. Even without knowing the NV orientation, information on the

electric field alignment is obtainable if the crystal lattice orientation in the laboratory coordinate system is known. For measurements in a bulk crystal, normally the crystal lattice orientation is known. Therefore by fitting the observed rotational pattern a Stark shift of $k_\perp E_\perp = 81.6 \pm 1.7$ kHz and an electric field angle of $\phi_E = 62 \pm 2°$. Since the orientation of the NV coordinate system with regard to the lab coordinate system θ is only known up to a $180°$ ambiguity, θ_E is given by $\theta_E = \phi_E \pm 90°$. The observed electric field amplitude and angle agree well with a simulation of the electric field from the tips (see Fig. 6.8a)

Therefore the sensing of a complete electric field vector is possible using one NV center. Since we did not obtain the NV crystallographic orientation, we determined the electric field orientation up to a $180°$ ambiguity. Without knowledge of the NV orientation in regards to the crystal lattice and the external magnetic fields, only a change of the electric field vector is detectable.

6.5. Single charge detection at ambient conditions
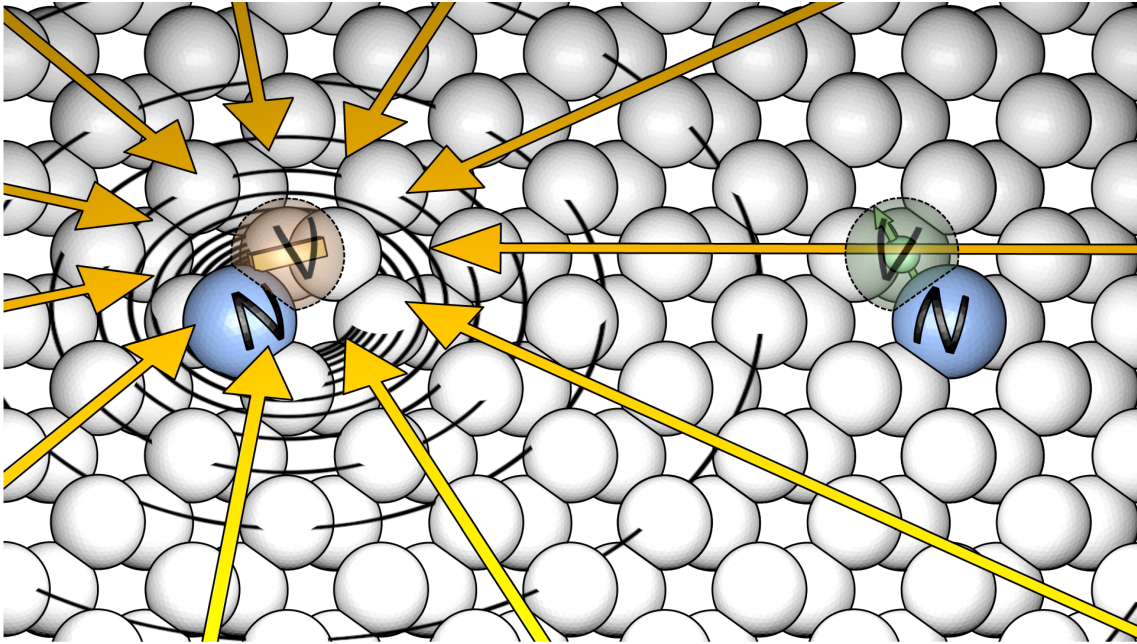
Figure 6.13.: Single charge detection configuration. A pair of NV centers is used for the single charge detection scheme. One NV center is used as sensor, while the other NV provides a stable charge, which can be deterministically switched with laser ionization.[1]

Single charge detectors with nanoscale spatial resolution operating at ambient conditions have diverse interdisciplinary applications as probes of physical phenomena [94, 95, 97], components of quantum and nano-devices [96, 107], and as high-performance sensors of chemical and biological species [108, 109]. The detection of elementary charges is a long-standing endeavor, with a number of low temperature/pressure techniques available, including single-electron transistors [94–96], scanning probe microscopy [97, 98, 110] , electric field-sensitive atomic force microscopy [111], electromechanical resonators [99, 112] and nanowire field-effect transistors [113]. Yet, few techniques are available that operate under both ambient temperature and pressure and can detect small numbers of elementary charges [114]. None of which currently shows nanoscale resolution.

However, as demonstrated in the previous section (Chapter 6.4), the NV center is capable of detecting a single charge at a distance of ~ 150 nm within one second of averaging. For these experiments, a NV pair separated by a nanoscale distance was created by ion implantation (see Chapter 7.2.2). One NV center is used as a sensor NV. The other NV provides the fundamental charge by its different charge state $NV^{0/-}$. In order to allow for electric field susceptible eigenstates, a magnetic field of ≈ 5.5 mT was applied perpendicular to the sensor-NV axis. This leads to a

---

[1]Image courtesy of Ingmar Jacobi.

suppression of residual axial magnetic fields and the hyperfine interaction with the ^{15}N nucleus (see Chapter 6.5.1). Additionally the interaction with the spin bath is suppressed, in combination with an isotopically purified sample (C_{13C}=0.001) expanding the coherence times to $T_2^* = 58.9 \pm 9.2$ μs allowing for an FID based measurement scheme.

a.

b.
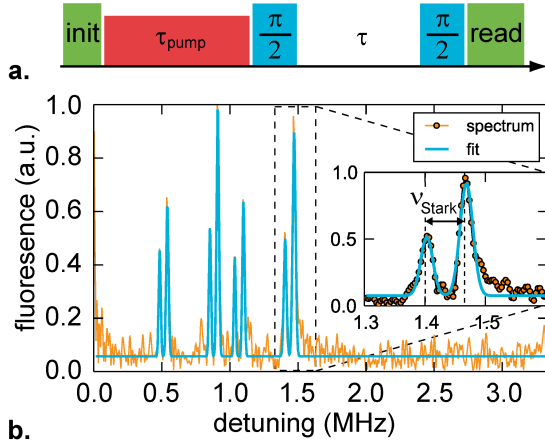
Figure 6.14.: Single charge detection. a. detection sequenc.e After initialization the charge-NV center is pumped by a red laser into the desired charge state which is then probed by a Ramsey sequence on the sensor NV. **b. FFT of the Ramsey experiment.** Here the frequency spectrum of the Ramsey experiment is shown. The single transition energy is split into four due to hyperfine interaction with ^{15}N. These are then, as shown in the inlay split by the electric field due to the fundamental charge.

With laser pumping, the charge NV can be deterministically transferred from the NV$^-$ to NV^0 [64], allowing to switch a fundamental charge on demand (see Chapter 6.5.2). Therefore the detection sequence consists of an initialization green laser pulse (532 nm) polarizing the sensor NV into the $|0\rangle$ state and resetting the charge-NV's charge state. With a red laser (638 nm) the charge-NV is ionized to achieve the desired charge ratio, depending on the pump time τ_{pump}. A Ramsey experiment on the sensor NV is then used to probe the charge ratio (see Fig. 6.14a). A typical spectrum obtained by an FFT of the Ramsey experiment is shown in Fig. 6.14b. Please note, that the transition is split into four lines by the hyperfine interaction with the ^{15}N (see

Chapter 6.5.1 for more details). These four lines are then split by the Stark effect of $\nu_{\text{Stark}} = 66 \pm 7$ kHz due to the fundamental charge of the charge NV.

Interpreting the observed electric field shift as being due to the displacement of a single electron at the charge NV position to a distant location, the transverse distance to the electron from the sensor NV can be calculated using the electric field from a point source given by

$$\underline{E}(\underline{r}) = \frac{1}{4\pi\epsilon_0\epsilon_r} \frac{e}{|r|^3}\underline{r} \tag{6.22}$$

where e is the electron charge, $\epsilon_r = 5.7$, ϵ_0 is the vacuum permittivity and $\underline{r}$ is the positon vector with the sensor-NV as origin. Since the distance is consistent with the distance allowed by the dipolar coupling $\nu_{\text{dip}} = 4.93 \pm 0.02$ kHz (see Fig. 6.18b.)

and there exists substantial evidence supporting the NV charge state assignments, we conclude that we have detected a single electron. Additionally we can conclude that the electron is not simply transferred to a close by charge trap, but is moved at least 40 nm farther away from the sensor NV. This suggests that the electron is ionized into the conduction band of diamond and there are most likely no proximity charge traps.

6.5.1. Hyperfine interaction vs. electric field detection

a.

b.
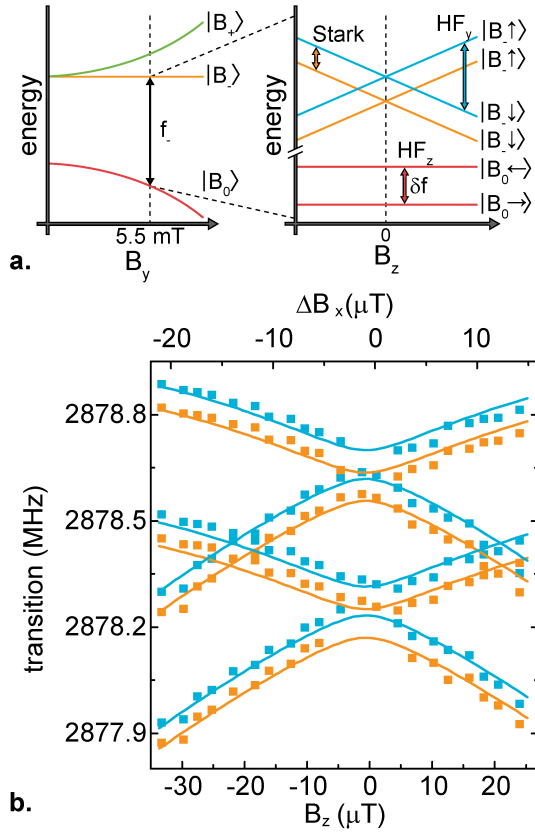
Figure 6.15.: Spectra for a sweeping field. a. Left: Energy diagram with increasing nonaxial magnetic field B_y. Right: Effect on the energy levels of hyperfine (HF) coupled electron spin nuclear spin pair due to additionally applied electric and axial magnetic fields (Stark and B_z). **b.** Afield of $B_y \approx 5.53$ mT was applied in the y direction while a magnetic field in the x, z plane was swept (x in the laboratory frame). The blue data is for a negative charge state and the orange data is the corresponding neutral charge state of the charge NV. Due to the large $B_\perp$, there is almost no change in the Stark effect due to an applied small B_z.

Since the observed electric field shifts are smaller than the ^{15}N magnetic hyperfine interaction with the ground state electron spin, it is necessary to account for the hyperfine structure of the electron spin resonances. The hyperfine interaction is described by the addition of the following term to the electron spin-Hamiltonian [57]

$$H_{\mathrm{hf}} = a_\parallel S_z I_z$$
$$+ a_\perp (S_x I_x + S_y I_y) - \gamma_{^{15}\mathrm{N}} \underline{B}\,\underline{I} \quad (6.23)$$

where $\underline{I}$ are the $I = 1/2$ nuclear spin operators, $a_\parallel = 3.03 \pm 0.03$ MHz, $a_\perp = 3.65 \pm 0.03$ MHz are the ^{15}N hyperfine parameters [52] and $\gamma_{^{15}\mathrm{N}}$ the nitrogen's gyromagnetic ratio.

As described in Chapter 6.4.1, in the presence of a transverse magnetic field, the $|B_-\rangle$ electron spin state is an equal mixture of the $m_s = \pm 1$ spin projections. Consequently, there is no first-order magnetic hyperfine splitting of the $m_I = \pm 1/2$ sub-levels of the $|B_-\rangle$ electron spin states. At second-order, the nuclear spin projections remain degenerate for $|B_-\rangle$, whilst they become equally mixed for the $|B_0\rangle$ electron spin state and split by $\delta f = 2a_\perp B_\perp / D$. Hence, the $|B_0\rangle \leftrightarrow |B_-\rangle$ electron spin resonances both split into two hyperfine resonances separated by δf (see Fig. 6.15a.). If a small B_z component is introduced to the magnetic field, the $|B_-\rangle$ electron spin state is no longer equal mixtures of the $|\pm\rangle$ states and thus, $|B_-\rangle$ gains a first-order magnetic hyperfine splitting. Since the nuclear spin projections are still mixed in the $|B_0\rangle$ electron spin state, microwave transitions are allowed between each of the hyperfine levels of $|B_0\rangle$ and $|B_-\rangle$. Thus,

in this case, the $|B_0\rangle \leftrightarrow |B_-\rangle$ electron spin resonances are both split into four hyperfine resonances. The hyperfine structure and its dependence on B_z is shown in Fig. 6.15.

The transverse electric field shift $k_\perp E_\perp$ at the sensor-NV due to the change in charge at the charge-NV was determined by least squares fitting the observed spin resonances as functions of magnetic field using numerical solutions to the complete spin-Hamiltonian $H + V_{\text{hf}}$ yielding $\nu_{\text{Stark}} = 66 \pm 7$ kHz. The zero-field splitting parameter $D = 2870.61 \pm 0.01$ MHz of the sensor-NV was independently determined using ODMR measurements with an applied field.

6.5.2. Laser pumping of the detected charge transition

The charge state of the NV can be controlled by laser irradiation. A red laser between 575 nm (ZPL NV^0) and 637 nm (ZPL NV$^-$) allows for a selective excitation of NV$^-$. As described in Chapter 4.2, the charge transition is governed by a two photon absorption process. If only NV$^-$ is excited, the NV center can be deterministically pumped to NV^0. In this experiment we employed a 638 nm laser to change the charge state ratio of the charge-NV. However the pumping laser not only affects the charge-NV, but the sensor-NV charge state is also affected, decreasing the detected signal. This can be compensated by analyzing the relative ratio of the NV^0 and NV$^-$ peaks (see Fig. 6.17),
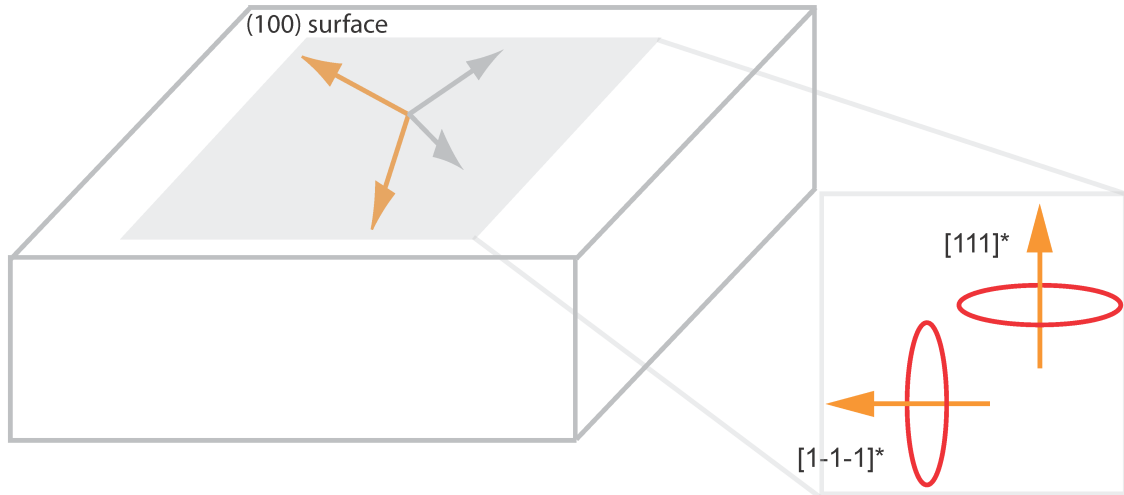

Figure 6.16.: NV orientation and laser polarization. The circular absorption profile orthogonal to the NV axis is projected to an ellipsoid shape on the diamond surface, allowing a higher absorption efficiency of one NV if polarized light is rotated to match its absorption maximum. * are the projections of the respective NV orientations on the (100) surface.

Additionally the NV center orientation can be exploited to enhance the sensor-NV signal. The NV center has two optical transition dipoles orthogonal to the NV axis (i.e. in the x, y plane). Therefore, the absorption cross section is equal for any linear polarization direction if the illumination light is directed along the NV symmetry axis ($\langle 111 \rangle$). However, since the used sample has a (100) surface the NV centers' symmetry axes are not orthogonal to the surface, but are tilted by half the tetrahedral angle (i.e. $\theta = 54.7°$). In the latter case, the absorption cross section σ depends on the direction of the linear light polarization α according to

$$\sigma(\theta, \alpha) = (1 - \sin\theta \sin\alpha)\, \sigma_{\mathrm{max}}.$$

Due to the two photon ionization process [64], the ionization ratio for red light aligned with one NV center is significantly higher than for the nonaligned case (if working below saturation). This allows for unequal charge state pumping of the NV centers, thereby allowing the ODMR measurement of sensor NV to be relatively unperturbed.
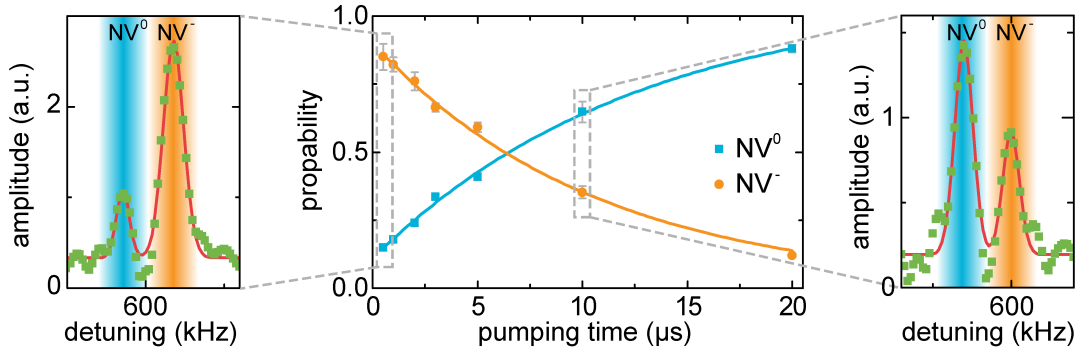
Figure 6.17.: Charge state vs. $\tau_{\mathbf{pump}}$. For longer pumping times τ_{pump} the charge state is pumped to NV$^-$. On the left a charge state ratio for $\tau = 0.5$ μs and on the right for $\tau = 10$ μs is shown. The charge state pumping is clearly visible in the relative amplitude of the peaks.

In Fig. 6.17 the NV^0/NV$^-$ ratio for constant pumping power in relation to the pumping time τ_{pump} is shown. Even though the charge transfer is a two photon process, with constant pumping power a constant pumping rate is given [64]. The data shown in Fig. 6.17 fits this exponential model. This is additional proof that the NV dark state reached by red laser pumping [50, 115] is indeed NV^0.

6.5.3. Directional sensing using a rotating magnetic field

a.

b.
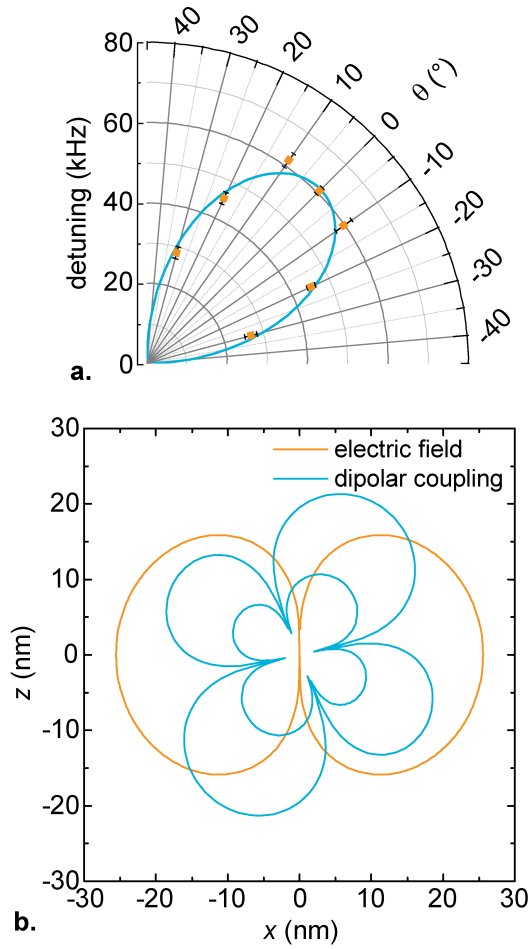
Figure 6.18.: Directional charge sensing. a. Measurement of the Stark shift with rotating $B_\perp$ around the NV axis. The angle is given in the laboratory coordinate system and corresponds to $\phi_B + 90°$ **b.** possible NV positions given by the Stark shift (orange) and the dipolar coupling $\nu_{\mathrm{dip}} = 4.93 \pm 0.05$ kHz (blue). The line intersections give the 8 possible NV positions.

As shown in Chapter 6.4.4, with orthogonal magnetic field $B_\perp$ rotating around the NV axis, the direction of the electric field can be determined if the NV orientation is known [68, 106]. For the NV pair, unfortunately only the alignment of the NV centers and not its orientation is known (see A.7). However since the crystal axis with respect to the external magnetic fields are known, measuring the Stark shift with a rotating magnetic field $B_\perp$, allows to determine the orientation ϕ_E up to a 180° unambiguity.

In Fig. 6.18a a magnetic field rotation measurement is shown. Due to the sign unambiguity of the electric field interaction the absolute value of the shift is shown. The magnetic field angle θ is given in the laboratory frame, where an angle of 0° coincides with a magnetic field in y direction. A fit of the lobe yields an electric field orientation in the NV reference frame of $\phi_E = 1 \pm 4°$. Therefore the two NV pairs are almost in the same $x - z$ plane (in the laboratory as well as NV coordinate system). We therefore determined the alignment of the electric field from a single charge.

Fig. 6.18b shows the possible x and z distances of the NV pair in the reference frame of the sensor-NV. The line intersection of the distances given by the Stark effect ($\nu_{\mathrm{Stark}} = 66 \pm 7$ kHz, orange lines) and the dipolar coupling ($\nu_{\mathrm{dip}} = 4.93 \pm 0.05$ kHz, blue lines) are the possible NV positions. There are eight possible distances in four groups (± 1.9 nm, ± 10.5 nm), (± 15.2 nm, ± 15.2 nm),(∓ 3.6 nm, ± 12.8 nm) and (∓ 1.0 nm, ± 8.6 nm).

6.6. Conclusion

Nanoscale sensing is right at the frontier of modern metrology applications. With the NV center, as a single quantum object, it is now possible to exploit the vast knowledge gained in quantum physics to achieve the most sensitive nanoscale detectors so far. With its exceedingly long coherence times [15, 61] and optical spin read out [12] it is a prime candidate for quantum metrology. With stable NV centers in nanodiamonds in the single digit nanometer range (7 nm smallest containing NV measured so far [14]), it provides a quantum sensor at the length scales of conventional dye and sensor molecules, however with very low cytotoxicity and no photo bleaching [47]. Using the long coherence times, quantum sensing schemes (i.e. a coherent phase evolution) can be utilized to detect magnetic fields similar to interferometric measurements in optics. A shift of the eigenenergies is used to detect, e.g. magnetic fields (Zeeman interaction) The obtained maximal sensitivity $\eta_{\max}$ is inversely proportional to the coherence time ($\eta_{\max} \propto \frac{1}{\sqrt{T_{\mathrm{coh}}}}$). By direct measurements of the spectrum or Ramsey-type experiments static field shifts can be detected. Refocusing schemes such as a Hahn echo allows to tailor the sensing frequency to detect fluctuating fields while extending the coherence time to the pure dephasing regime T_2 [23].

In this chapter, the detection scheme was extended using dynamical decoupling protocols (CPMG) to extend the coherence time to $T_{\mathrm{coh}} = \frac{1}{2}T_1$ improving the sensitivity from $\eta_{\mathrm{Hahn}} = 19.4 \pm 0.4 \frac{nT}{\sqrt{Hz}}$ to $\eta_{\mathrm{CPMG}} = 11.0 \pm 0.2 \frac{nT}{\sqrt{Hz}}$. This brings the sensitivity to the limit of spin-lattice relaxation of the NV center. Additionally dynamical decoupling allows to tailor the magnetic susceptibility of the NV to a certain detection frequency, e.g. allowing lock in detection of external hydrogen nuclei demonstrated by Staudacher et al.[44].

Not only magnetic fields (Zeeman effect) can be detected using the methods developed for the NV center, but also the linear Stark effect can be exploited for field sensing [21]. We investigated the applications of electric field sensing using a single NV center. In order to have the highest susceptibility to electric fields, the NV eigenstates have to be tailored to commute with the electric field Hamiltonian. This is the case as long as the electric field effect is larger than effects from the axial magnetic field. An electric field sensitivity for DC fields of $\eta_{\mathrm{FID}} = 631.1 \pm 15.1 \frac{\mathrm{V}}{\mathrm{cm}\sqrt{\mathrm{Hz}}}$ and $\eta_{\mathrm{Hahn}} = 142.6 \pm 3.6 \frac{\mathrm{V}}{\mathrm{cm}\sqrt{\mathrm{Hz}}}$ for AC fields was demonstrated. The AC field sensitivity corresponds to the sensing of a single fundamental charge at a distance of about 250 nm in 10 seconds measurement time. With the application of nonaxial magnetic fields, a nontrivial interplay between the electric field and magnetic field orientation allows to detect the full electric field vector using a single NV. This

allows for the detection of the orientation and magnitude of an electric field created by micro-electrodes on the diamond surface.

In order to demonstrate the exceptional sensitivity of electric field measurements, we devised an experiment to detect single fundamental charge. As a stable, controllable charge we choose another charge-NV center at a distance of about 10 to 20 nanometers. With optical charge state pumping, the charge of the charge-NV could be controlled and the change in electric field observed with the sensor-NV. With the use of nonaxial magnetic fields the orientation of the electric field vector was determined. This is not only one of the few demonstrations of nanoscale detection of a fundamental charge at ambient conditions, but also gave valuable insight into the charge dynamics and yielded additional proof that the NV^0 should be assigned a different charge state than NV^- [50].

The electric and magnetic field sensing demonstrated in this work pave the way for the application of quantum metrology in material sciences as well as life sciences. The electric field interaction $\nu_{Stark} = 66 \pm 7$ kHz from a fundamental charge is about an order of magnitude larger than the dipolar coupling $\nu_{dip} = 4.93 \pm 0.05$ kHz of the corresponding spin. Therefore electric field sensing could replace nanoscale NMR [44, 89] and instead of detecting spin densities measure the charge distribution in a molecule for structure determination. For the application in life sciences, there has been an tremendous effort in the last years studying e.g. cell intake [116] or labeling of nanodiamonds [117]. It is expected that in the coming years all pieces come together and quantum metrology will start to have a large impact on life sciences allowing the simultaneous detection of electric fields, magnetic fields and temperature and their corresponding dynamics [85, 118].
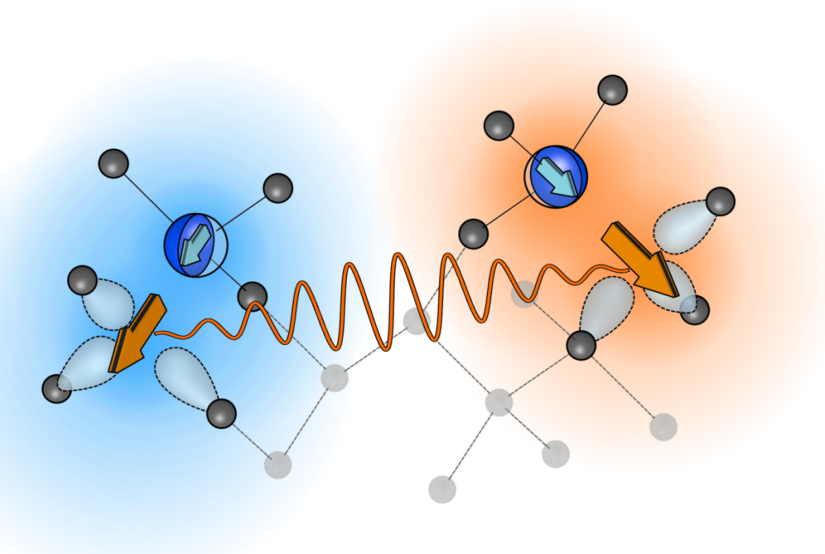
7. Quantum register

Figure 7.1.: Schematic of NV pair[1]

7.1. Introduction

Entanglement is a cornerstone phenomenon of quantum physics. Once considered a counter-intuitive property of quantum theory [119] it has developed into the most central element of quantum technology providing speed up to quantum computers, a path towards long distance quantum cryptography and increased sensitivity in quantum metrology.

An entangled state is a coherent superposition state between two or more entities with at least a two-level system (qubit). For two qubits, Bell formulated the two basic entangled states, the $\Phi_\pm$ states $(\Phi_\pm = \frac{1}{\sqrt{2}}(|00\rangle \pm |11\rangle))$ and the $\Psi_\pm$ states $(\Psi_\pm = \frac{1}{\sqrt{2}}(|01\rangle \pm |10\rangle))$. The non-local correlation between the qubits leads to fascinating properties of an entangled state. By a projective measurement of one qubit, the state of the other qubit is determined. The nonlocal coherence of the

---

[1]Image courtesy of Ingmar Jacobi.

entangled state evolves not for each qubit individually, but as a sum or difference of the local phases (phase on qubit would acquire).

Quantum information processing and communication use the collective nature of the entangled state to either have the equivalent of multiple classical operations in one measurement step (e.g. Shor's algorithm for number factorization [2] or the Grover algorithm for faster database search [3]) or ensure secure communication using a quantum channel. The collective coherent behavior is considered a resource for quantum metrology, where the collective phase accumulation promises an enhancement in sensor sensitivity beating the shot noise limit. Recently a new field emerged, where a larger number of well controlled entangled qubits is used to simulate other quantum systems, e.g. simulating the energy landscape of small molecules [120].

There has been a number of experimental demonstrations of entanglement between photons [121], atoms [4], ions [5] as well as solid state systems like spins or quantum dots [6, 7, 30], superconducting circuits [8, 9] and macroscopic diamond [10]. However, a fleeting achievement for the field is the scalability of the quantum registers (allowing for an entangled state with a large number of qubits).

The NV center in diamond is an exceptional qutrit. It allows read out and control of its ground state manifold of the electron spin at room temperature [12], has coherence times in the order of milliseconds [15, 61, 122]. Apart from NOT and CNOT gates, which are commonly used in theoretical quantum information processing (QIP), a straight forward implementation of a universal set of quantum gates is achieved by ROT and CROT gates. The main difference between a CROT gate and a CNOT gate, is an additional phase factor, but both can be used to build a universal set of gates [27]. With the implementation of optimal control (see Chapter 7.6), in principle any unitary gate can be synthesized.

For the NV center a quantum register has been realized with the electron spin as a central electron spin allowing for single shot read out of the surrounding nuclear spins ($^{14/15}$N and ^{13}C) [28, 30, 31] achieving a quantum register containing 4 qubits [18]. Phase flip quantum error correction has been achieved recently by Waldherr et al. [18] for this quantum register. This allows to use theses quantum registers as quantum repeater and in combination with the nuclear spin coherence reaching seconds at room temperature [19] as quantum memory.

In order to scale the register, it is necessary to create coherent interactions between the electron spins of different NV centers (an electron spin quantum bus [123]), where the nuclear spins will then be used as memory units (every NV center has an intrinsic memory given by the $^{14/15}$N nuclear spin). There have been different proposals to achieve this quantum interaction. There are proposals to use a mechanical

transducer (the electron spin is coupled to a mechanical resonator by a magnetic field gradient) to either couple two NV centers directly [124] or by capacitive channel [34]. Similar proposals want to harness the spin phonon interaction in a nano-beam to create a coherent interaction [125]. Also hybrid devices between superconducting resonators and NV center electron spins yield the possibility for coherent communication channel [126–128].

Also a photon mediated entanglement channel is possible with spin-photon entanglement [129]. A first heralded realization based on a two photon interference experiment was successful, but yielded only one entanglement event every few minutes [35]. The main hindrance for a high probability entanglement channel is the low photon collection efficiency. Nanostructures like photonic crystal cavities [130, 131] yield the potential to achieve success probabilities allowing for photon mediated entanglement in the lifetime of the nuclear spin memory (seconds [19]).
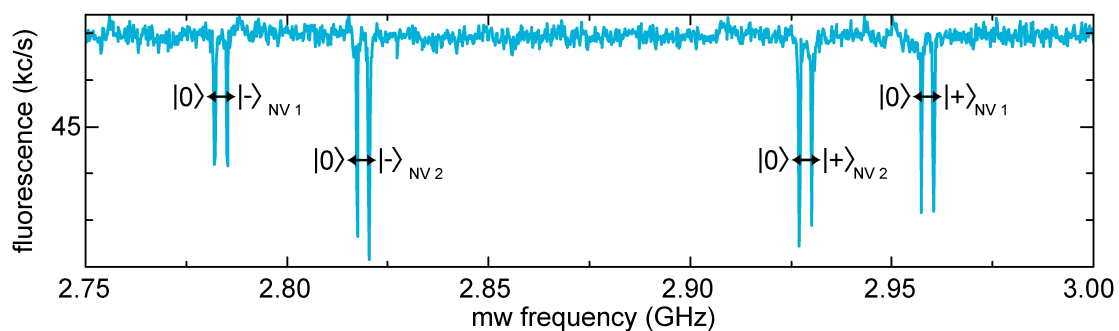
Figure 7.2.: ODMR spectrum. The ODMR spectrum of the NV pair reveals four different transition energies (split again by the hyperfine interaction with ^{15}N). The different crystallographic orientation of the NVs allows with the application of a magnetic field for individual addressing of the NV center transitions and therefore individual spin control.

For room temperature, so far the only scaling proposals so far are based on dipolar interactions between electron spins. The most straightforward approach is to place the NV centers sufficiently close to each other [132, 133]. Since strong coupling is required for coherent interaction, the minimal dipolar coupling is given by $\nu_{\text{dip}} = \frac{1}{T_{\text{coh}}}$. Therefore the effective magnetic dipolar interaction range is limited by the coherence lifetime (here: $\sim 2\,\text{ms}$ [78]) to about ~ 100 nm for electron spins and ~ 5 nm for nuclear ones. With optical super-resolution techniques individual optical spin readout with nanometer-scale resolution can be facilitated [134]. Since microwaves cannot be focused down to these length scales, individual spin addressability via magnetic resonance can be achieved by separating the spins' resonance frequencies, for example, by applying local magnetic field gradients ($\approx 2\mu\text{T/nm}$), or by exploiting different crystal field directions (see Fig. 7.2). Coherent

control of individual electron and nuclear spins is then conducted via resonant mw and rf fields. The nuclear spins (for ^{15}N and ^{13}C) can be additionally controlled via their hyperfine interaction with the neighboring electron spin. Effectively, the electron spin state sets the axis and speed of nuclear Larmor precession allowing for coherent control [60].

In this chapter, a first step towards the scaling of an NV center-based quantum register by dipolar interaction is demonstrated. An implantation method is developed allowing for the creation of NV pairs with a reasonable success rate (Chapter 7.2.2). In order to harness the pure dephasing time T_2 (for the NV, T_2 is normally two orders of magnitude larger than T_2^*), an entanglement scheme is developed using dynamical decoupling and a coherent spin dependent phase evolution (Chapter 7.4.1). This led to the first room temperature demonstration of entangled electron spins in a solid state matrix (Chapter 7.4). The nuclear spin memory was used to store the electron spin entanglement for milliseconds (Chapter 7.5) leading to a remote entangled state of the NV's nuclear spins (Chapter 7.6.7).

The unavoidably crowded spectrum leads to non-negligible control crosstalk and reduces the fidelity of local gates. Consequently, it becomes challenging to perform strictly local operations. While all these are minor issues for standard spectroscopy techniques, the fidelity of quantum operations can be drastically affected, especially for repeated gate application. This problem was addressed by implementing optimal control based on the gradient ascent pulse engineering algorithm (GRAPE). High fidelity local operations (Chapter 7.6.4), electron spin entanglement (Chapter 7.6.6) as well as entanglement storage and nuclear spin entanglement (Chapter 7.6.7) was implemented. In principle, optimal control allows for an implementation of any unitary operation of the quantum register. Also the high fidelity local and nonlocal operations demonstrated here will be essential for all scaling schemes for spin based quantum registers.

7.2. Sample creation and characterization
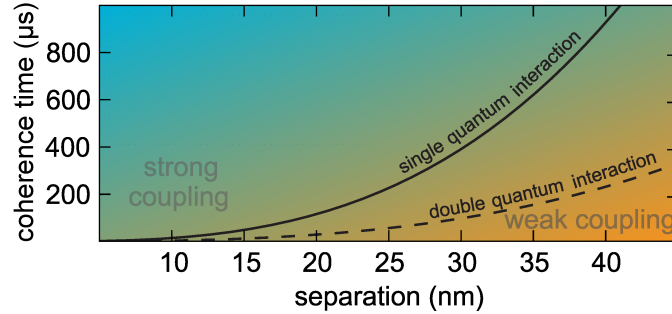
Figure 7.3.: Strong coupling limit. The necessary coherence times for strong coupling vs. the NV-NV separation is shown. The NV-NV separation is given for the average interaction strength.

In order to create an electron spin quantum register, the dipolar coupling ν_{dip} has to be larger than the inverse of the relevant coherence time $1/T_{\mathrm{coh}}$ (strong coupling regime). For a controlled operation based on dipolar coupling resolved driving of the NV transitions, the inhomogeneous line width T_2^* governs the minimal coupling strength [27], thus limiting the minimal dipolar coupling to $\nu_{\mathrm{dip\ min}} = 1/T_2^* \approx 1/30\mu$s ≈ 33 kHz for isotopically engineered samples available [15]. In Chapter 7.4.1 an entanglement sequence based on CPHASE gates is developed, allowing for dynamical decoupling and thereby increasing the relevant coherence time to T_2 pushing the strong coupling limit down by two orders of magnitude to $\nu_{\mathrm{dip\ min}} = 1/T_2 \approx 1/2$ms ≈ 0.5kHz either by using a simple Hahn echo in an isotopically pure diamond [15] or by applying a more elaborate decoupling scheme [61, 62].

However even with the relaxed strong coupling requirements, the probability of finding two NV centers in a sample dilute enough to resolve single NVs with a confocal microscope is tiny (a distance of smaller ca. 30 nm is reasonable for strong coupling with coherence times in the order of milliseconds). Therefore a strategy to create a desired pair of NV centers with manageable probability is necessary. To date, two methods of creating NV centers are commonly used. First the implantation of high energy nitrogen ions creating vacancies with subsequent annealing is widely used to obtain high quality NV centers. The implantation of nitrogen ions has proven to be very versatile allowing for targeted implantation either by focusing the implantation beam (approx. 500 nm beam diameter for MeV ion energies)[135] or by a mask implantation approach similar to standard techniques in semiconductor production (e-beam lithography allows for mask diameters of about 10 nm) [132, 136]. However mask implantation methods so far only allowed for low implantation energies. The proximity to the surface reduced the coherence times

drastically [137]. With the use of ^{15}N with a natural abundance of ca. 0.4% it is possible to discriminate between implanted and intrinsic NVs [59]. Additionally only ion implantation allows the deterministic implantation of single nitrogen ions [138].

In order to have the necessary coherence times to implement entanglement protocols, a high enough implantation energy is necessary to create NV pairs deep enough in the diamond lattice [139]. Since the available ion beams had widths of $\approx$500 nm for MeV implantation energies [43], implantations without a mask would not be sufficient for a high success rate. On the other hand, conventional mask technology such as e-beam lithography [132] are only suitable for low energy implantations (a few keV) due to the limited thickness of the photo-resist. Therefore a high energy ion implantation technique based on a nanochannels in a thick mica mask was developed, allowing for 1 MeV implantation energies with a point source like ion distribution yielding a success rate of $\approx$ 3%. With a prescreening using the super-resolution method ground state depletion microscopy (GSD) [140, 141], allowing to preselect possible candidates, and a subsequent double electron electron resonance experiment (DEER, see Chapter 7.3.1) to measure the dipolar coupling ν_{dip}, a NV pair in the strong coupling regime was identified.

Recent advances in diamond fabrication, such as the growth of NV delta-doped layers [142] as well as orientation preferential incorporation of NV centers [68] will, in combination with nano-structuring, open up new possibilities to create arrays of NV centers.

7.2.1. Ion implantation basics
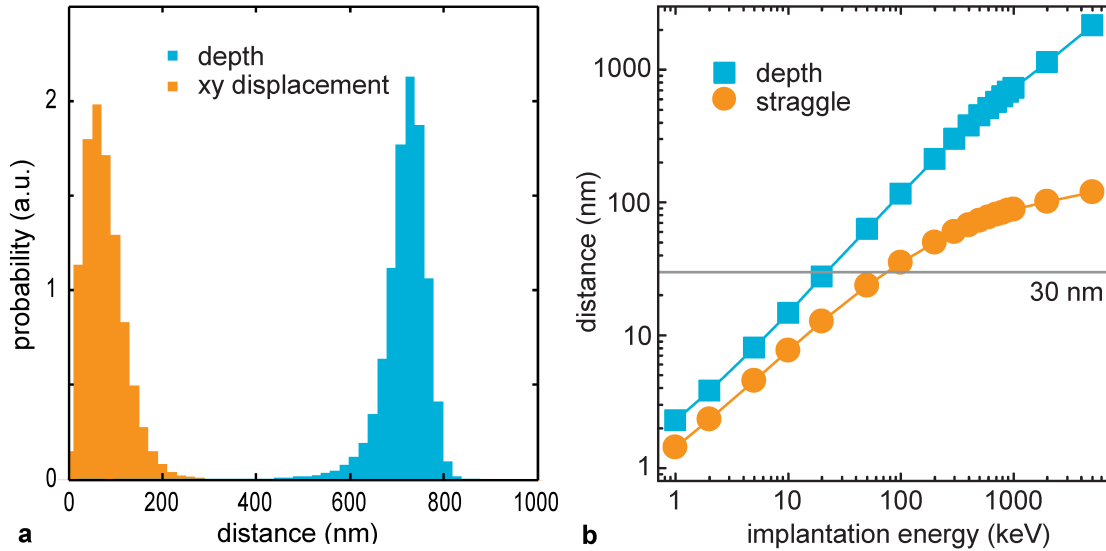
Figure 7.4.: SRIM simulation of ^{15}N-ion implantation in diamond. a. Histogram of the simulated penetration depth z as well as the displacement in xy for 1 MeV per ion implantation energy as used in sample creation. **b.** The straggle (standard deviation of the xyz distribution) of the implantation ion as well as the implantation depth are shown. 30 nm denotes a limit to the NV-NV distance given by the strong coupling limit. Therefore an implantation above 80 keV yields a straggle too large for deterministic NV pair creation

In order to create NV centers by implantation, nitrogen ions are accelerated and shot into diamond. They will then scatter inelastically from sequential carbons in the lattice and create a track of vacancies while decelerating. During a subsequent annealing step, the vacancies become mobile and diffuse through the diamond lattice. Eventually a vacancy diffuses close to a nitrogen replacing a carbon atom. This vacancy is then captured by the nitrogen forming the NV center. By prolonged annealing as well as annealing at high temperatures, vacancies in the lattice can be healed out almost completely reducing the spin and charge impurities next to the NV center allowing for long coherence times [143].

Since the deceleration of the high energy nitrogen ions is a statistical process, the possible end positions can be simulated by a Monte Carlo method. A open-source classical simulation package for this is Stopping and Range of Ions in Matter (SRIM [144]). The simulation of the average implantation depth and average deviation from a straight implantation path (straggle) for different implantation energies is shown in Fig. 7.4. An implantation energy of about 100 keV seems to be ideal to create NV-NV pairs. Unfortunately, the only available accelerators were the low energy implanter in Stuttgart (max. 10 keV) and the Tandem accelerator in Bochum (min

1 MeV.) Therefore implantations were carried out using 1 MeV ions in Bochum to harness the longer coherence times deeper in the diamond.

7.2.2. Mica mask implantation
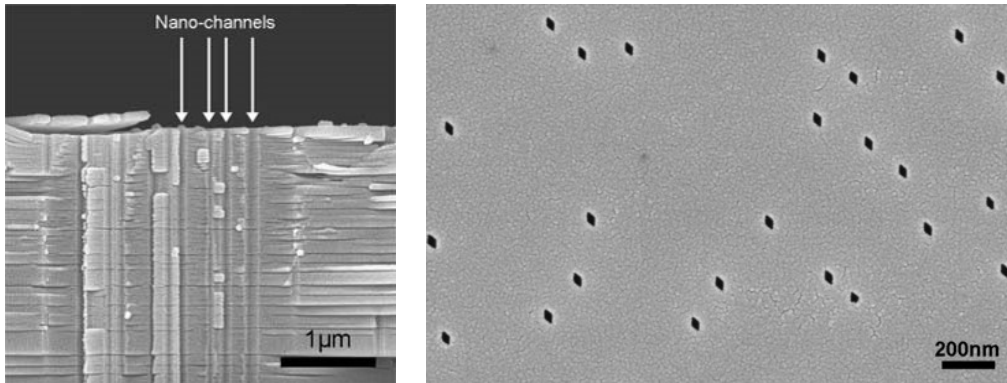
Figure 7.5.: Mica mask used for implantation. left cross-section electron microscopy image of a cleaved mica sheet with the etched ion channels. The straight channels were used for implantation. **right** Surface electron microscopy image of the mica sheet with ion holes. One can clearly see the individual etched ion holes. The rhomboid shape is due to the mica crystal lattice.

So far, mask implantation achieves high spatial implantation resolutions on the order of a few tens of nanometers [132, 145] but due to the thin mask material (masks were prepared using e-beam lithography allowing only for rather small aspect ratios in the order of 1:10) only allow for implantation energies in the keV range if high spatial resolution is necessary. Therefore a high aspect ratio micro channel mask in mica (aspect ratio > 1:160) was used for the ion implantation. The mask was created by bombardment of the mica layer with 1.7 GeV Samarium ions at the GSI in Darmstadt by Christina Trautman. Consecutive etching of the ion track in hydrofluoric acid resulting in 50 by 40 nm sized channels in an eight μm thick mica slab [136] (see Fig. 7.5). This thick mica layer with the outstanding aspect ratio allows for MeV implantation energies without losing spatial resolution due to the beam waist. 1 MeV ^{15}N ions were implanted through mica channels using the Tandem accelerator at the University of Bochum by Jan Meijer and Sébastien Pezzagna. By implanting ^{15}N with a natural abundance of 0.4% it was possible to confirm that the NV-centers stem from implanted nitrogen ions [59]. The implantation of the 1 MeV ^{15}N ions was simulated using the "SRIM" software package [144]. For that purpose the flux through the mica channel was assumed to be homogeneous. Ions originating from the mica channel (Fig. 7.6a) have a distribution with a straggle of 118.9 nm. The ratio of ion pairs with distances below 30 nm is 1.97%. Thus a reasonable ratio of implanted NV pairs is expected to show dipolar coupling while still having decent coherence times.

The implanted sample was then annealed at 800°C for 8 hours in vacuum. To increase the coherence times, a 99.9% ^{12}C sample was used allowing for coherence
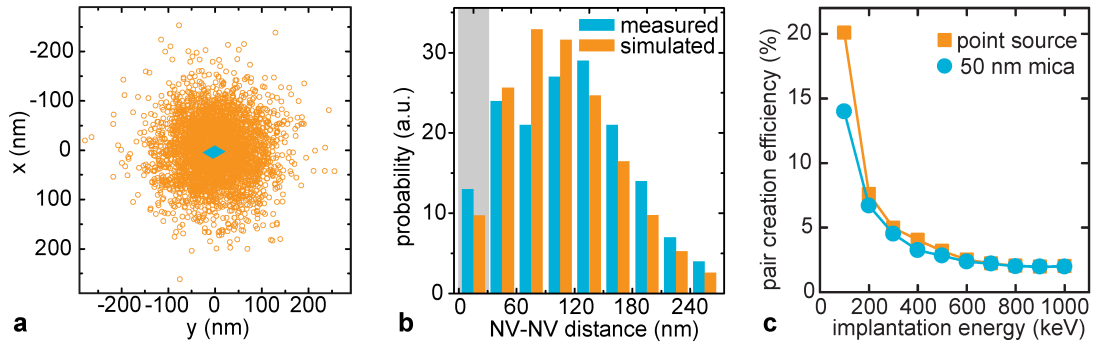
Figure 7.6.: 1MeV ^{15}N-ion implantation in diamond. a. lateral stopping positions (orange) of 5000 ions originating from a mica channel (blue). The flux through the 50 by 40 nm sized aperture is assumed to be homogeneous. The straggle is 118.9 nm. **b.** (blue) lateral distances of NV pairs measured by super resolution microscopy. (orange) distance histogram of simulated ion pairs. The gray area marks the NV centers close enough to allow for strong coupling. **c.** percentage of NV pairs created at a distance of 30 nm (strong coupling cut off) for a point source (blue data) and using a 50 nm mica nano-aperture simulated using SRIM.

times in the order of ms [78]. The NV distance correlation was measured using ground state depletion microscopy (GSD) [140, 141]. In Fig. 7.6b the NV-NV distance correlation in the surface plane is shown for the simulation and the measured results. The measured distance distribution is in good agreement with the simulation.

With a decrease of the implantation energy the pair creation efficiency can be increased even further. For the depth of a few 100 nm, coherence times in the order of a few hundred μs have been reported [146]. Here the approximation of the mica mask as a point source does not hold anymore. However with the mica masks used, creation efficiencies of 14% are possible (see Fig. 7.6c) and mask dimensions below 20 nm have been reported [136].

Recent progress has demonstrated that isotopically purified diamond allows for coherence times in the order of milliseconds close to the surface [147]. Additionally high temperature annealing [146] as well as overgrowing an additional diamond layer [133] have proven to prolong coherence times significantly. This opens the door for e-beam based mask creation [132, 148]. Also deterministic delta doping [142] with subsequent nano-structuring and overgrowth [133] yield potential for future sample fabrication. Additionally delta doping if grown on a (111) surface allows for the preferential alignment of the ingrown defect centers [68, 149, 150] which will become important for sensing as well as for high magnetic field applications.

7.3. NV-NV pair characteristics

7.3.1. NV-NV dipolar coupling strength and coherence properties
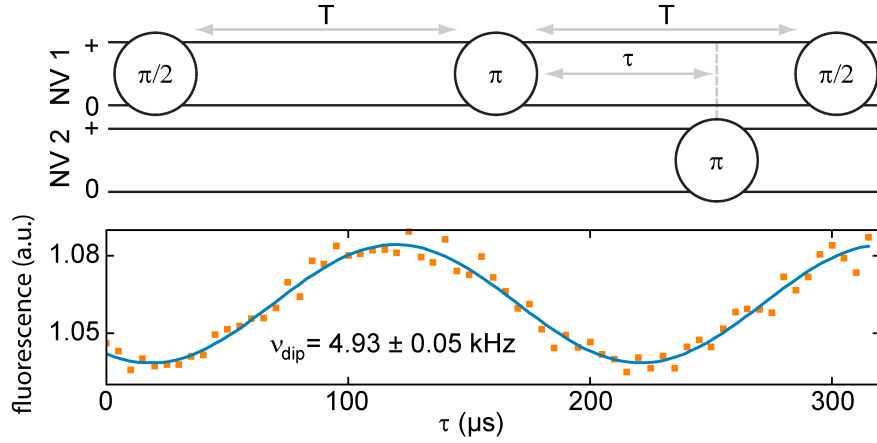
Figure 7.7.: Determination of ν_{dip}. top. The DEER measurement sequence is shown. **bottom.** The measured dipolar coupling ν_{dip} between the two NV centers is shown.

The coherence properties as well as the dipolar coupling strength are key parameters for a coherent evolution of the system and the creation of nonlocal states, e.g. entangled states. Therefore here the coherence times as well as the dipolar coupling ν_{dip} are given.

The coherence properties were measured using a Ramsey type of experiment, giving the phase memory time $T_{2\text{ DQ}}^*$. DQ denotes that the coherence time was measured for a double quantum coherence (coherence between $|+\rangle$ and $|-\rangle$, see Chapter A.8). With first order dynamical decoupling (Hahn echo) the coherence time decoupled from low frequency fluctuation was investigated giving $T_{2\text{ DQ}}$. The coherence properties measured for NV 1 were $T_{2\text{ DQ 1}}^* = 27.8 \pm 0.6 \ \mu s$ and $T_{2\text{ DQ 1}} = 150 \pm 17 \ \mu s$. For NV 2 coherence times were measured to be $T_{2\text{ DQ 2}}^* = 22.6 \pm 2.3 \ \mu s$ and $T_{2\text{ DQ 2}} = 514 \pm 50 \ \mu s$. Higher order dynamical decoupling did not increase the coherence properties of NV 1 indicating a fast fluctuating spin bath (i.e. an electron spin bath).

The dipolar coupling strength ν_{dip} is the key system parameter for coherent spin-spin interaction. In order to have strong coupling ($\nu_{\text{dip}} > 1/T_2$) between two NVs the interaction has to be stronger than the decoherence. Since the dipolar coupling between two distant electron spins is expected to be small in comparison to $1/T_2^*$, a direct measurement of the coupling via an ODMR spectrum is challenging. Therefore Double-Electron-Electron-Resonance (DEER, limited by T_2) experiments were utilized to measure ν_{dip} .

A DEER experiment consists of an Hahn echo on NV 1 and π pulse on NV 2 (see Fig. 7.7 top) and is described by:

$$\frac{\pi}{2}_{1+} \xrightarrow{\text{T}} \pi_{1+} \xrightarrow{\tau} \pi_{2+} \xrightarrow{\text{T}-\tau} \frac{\pi}{2}_{1+} \tag{7.1}$$

The Hahn echo refocuses all static detunings and only a phase $\phi_{\text{dip}} = 2\pi\nu_{\text{dip}}\tau$ is measured. The DEER measurement yields a dipolar coupling of $\nu_{\text{dip}} = 4.93 \pm 0.05$ kHz. This places the pair barely in the strong coupling regime if dynamical decoupling is used ($1/T_{2\text{ NV 1}} \approx 3.3$ kHz). However this will be enhanced using double quantum coherences as shown in Chapter 7.4.1

7.4. Electron spin entanglement

Creation of entanglement is a key resource in any quantum technology, especially in quantum information processing. The established procedure is to build an entanglement gate ENT using controlled ROT operations (CROT) in the strong coupling regime. Conventional implementations of controlled operations, such as the CNOT gates, by controlled addressing of microwave transition [27] require the inhomogeneous line width of the transition $(1/T_2^*)$ to be smaller than the line shift due to different spin states of the control.

For strong coupling $\nu_{\rm dip} < 1/T_2^*$ has to hold. Since $T_{2\,\rm NV1}^* = 55.6 \pm 1.2$ μs and $\nu_{\rm dip} = 4.93 \pm 0.05$ kHz, conventional CROT gates are not feasible.

But with the usage of dynamical decoupling the longer T_2 time scale becomes accessible. Here the controlled phase evolution due to the magnetic dipolar coupling is used to generate two CPHASE gates allowing for entanglement generation. Please note that a direct CNOT is hard to implement, therefore controlled rotation CROT gates were used.

7.4.1. Entanglement scheme

The inhomogeneous line width (time averaging) of the individual electron spin transitions is $\Delta\nu = 1/T_{2\,\rm NV1}^* \approx 1/0.056 \approx 18$ kHz. Since the dipolar coupling is only $\nu_{\rm dip} = 4.93 \pm 0.05$ kHz, controlled operations based on spectral addressing of spin states could not be implemented.

With dynamical decoupling the coherence time can be extended to $T_{2\,\rm DQ\,1} = 150 \pm 17$ μs allowing for strong coupling. In order to harness $T_{2\,\rm DQ}$, an entanglement sequence based on conditional phase accumulation (CPHASE) was developed. Here local operations (rotating one NV without, in the first order, affecting the other) and controlled phase evolutions are used to create an entangled state.

The entanglement circuit is shown in Fig. 7.8. It starts from the fully polarized state $|00\rangle$. With the first local operation U_1 a superposition between $|+\rangle$ and $|-\rangle$ is created on both NV centers. U_1 can be constructed by applying a $\frac{\pi}{2}_+$ pulse and then subsequently applying a π_- pulse on both NV centers. The resulting uncorrelated superposition state is given by $\frac{1}{2}\left(|++\rangle - |+-\rangle - |-+\rangle + |--\rangle\right)$. After a free evolution time τ a controlled phase (the phase is dependent on the spin state of the other NV) $\phi = 4\pi\nu_{\rm dip}\tau$ is accumulated according to $\frac{1}{2}\left(e^{+i\phi}|++\rangle - |+-\rangle - |-+\rangle + e^{+i\phi}|--\rangle\right)$. Please note that the effective dipolar coupling is enhanced by a factor of 4 as compared to two interacting spins with
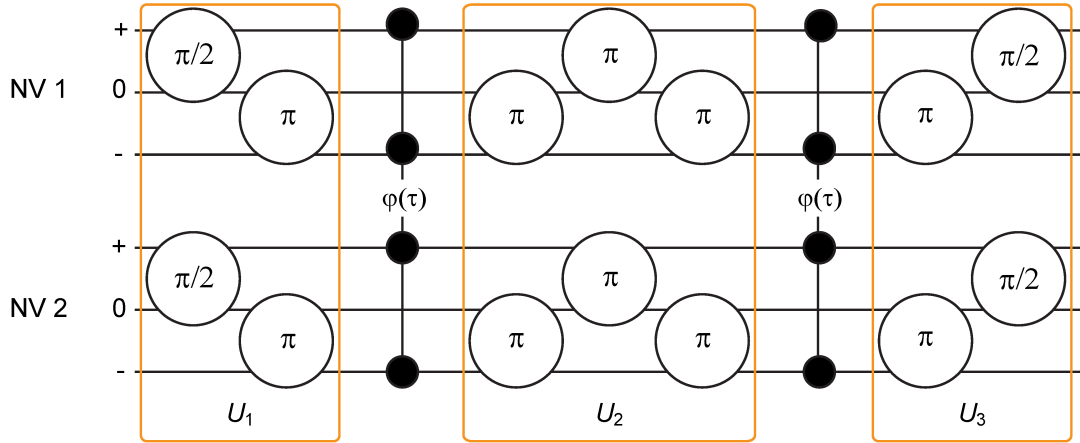
Figure 7.8.: Entanglement sequence - ENT gate. The entanglement sequence consists of two free evolution times τ and the unitary local operations $U_{1,2,3}$

S=1/2 due to "double quantum coherence" ($|-\rangle + |+\rangle$, see A.8 and reference [151]). In order to refocus any unwanted phases the local operation U_2, corresponding to a double quantum spin flip ($|-1\rangle \leftrightarrow |+1\rangle$), was implemented on both NV centers. U_2 can be emulated by the following pulses: $\pi_- - \pi_+ - \pi_-$, implemented on both NV centers simultaneously. After a second free evolution time the state is given by $\frac{1}{2}\left(e^{+2i\phi}|++\rangle - |+-\rangle - |-+\rangle + e^{+2i\phi}|--\rangle\right)$. With the local operation U_3 the control phase can be mapped into an entangled state. U_3 can be chosen to map the entangled state into any "qubit subspace" within the Hilbert space of the qutrit. With U_3 consisting of $\pi_- - \frac{\pi}{2}_+$ on both NV centers the resulting entangled state is given by $\psi(\tau) = \cos(\phi)|00\rangle - i\cos(\phi)|++\rangle$. However with the addition of a π_- pulse ($\pi_- - \frac{\pi}{2}_+ - \pi_-$) the state is mapped into $\psi(\tau) = \cos(\phi)|--\rangle + \sin(\phi)|++\rangle$. For $\tau = \frac{1}{16\nu_{\mathrm{dip}}}$ a fully entangled state is realized.

With the usage of a double quantum coherence a fourfold speed up of the entanglement sequence is achieved. This is due to the larger magnetic moment than for a spin 1/2 (indeed the magnetic moment is twice as large, the magnetic dipole-dipole interaction goes as μ^2) [152]. The coherence times are reduced by a factor of two as well due to the higher sensitivity to magnetic field noise. Given an empirical noise model for the decoherence, modeling decoherence as a Gaussian decay ($e^{-\left(\frac{\tau}{T_2}\right)^2}$), the fidelity, assuming perfect control and initialization for the single quantum evolution (e.g. using coherence between $|0\rangle$ and $|+\rangle$), is given by

$$F_{\mathrm{SQ}} = \frac{1}{4}\left(1 + \exp\left[\frac{-1}{8\ T_{2\ \mathrm{NV1}}^2 \nu_{\mathrm{dip}}^2}\right] + \exp\left[\frac{-1}{8\ T_{2\ \mathrm{NV2}}^2 \nu_{\mathrm{dip}}^2}\right] + \exp\left[\frac{-T_{2\ \mathrm{NV1}}^2 + T_{2\ \mathrm{NV2}}^2}{8\ T_{2\ \mathrm{NV1}}^2 T_{2\ \mathrm{NV2}}^2 \nu_{\mathrm{dip}}^2}\right]\right)$$

while the fidelity for the double quantum evolution (using coherence between $|-\rangle$

and $|+\rangle)$ is given by

$$F_{\mathrm{DQ}} = \frac{1}{4}\left(1+\exp\left[\frac{-1}{32T_{2\ \mathrm{NV1}}^2\nu_{\mathrm{dip}}^2}\right]+\exp\left[\frac{-1}{32T_{2\ \mathrm{NV2}}^2\nu_{\mathrm{dip}}^2}\right]+\exp\left[\frac{-T_{2\ \mathrm{NV1}}^2+T_{2\ \mathrm{NV2}}^2}{32T_{2\ \mathrm{NV1}}^2 T_{2\ \mathrm{NV2}}^2\nu_{\mathrm{dip}}^2}\right]\right).$$

The individual coherence times are reduced by a factor of two when switching to double quantum coherences, but the effective interaction is enhanced by a factor of four [152]. This leads, for a Gaussian decay, to an increase of the fidelity of the entangled state by usage of double quantum coherences.

Additionally with the choice of the use of a $|+\rangle \leftrightarrow |-\rangle$ coherence (double quantum subspace) any nontrivial dynamics of the ^{15}N nuclear spins (electron spin conditional rotations of the nuclear spin state) are suppressed allowing for an easier interpretation of the signal. In the double quantum subspace, the eigenbasis of the ^{15}N is independent on the electron spin state. Therefore no nuclear spin nutations are observable for $|\pm\rangle$ (see Chapter A.8 and Chapter 7.5.1).

7.4.2. Evolution of the entanglement scheme
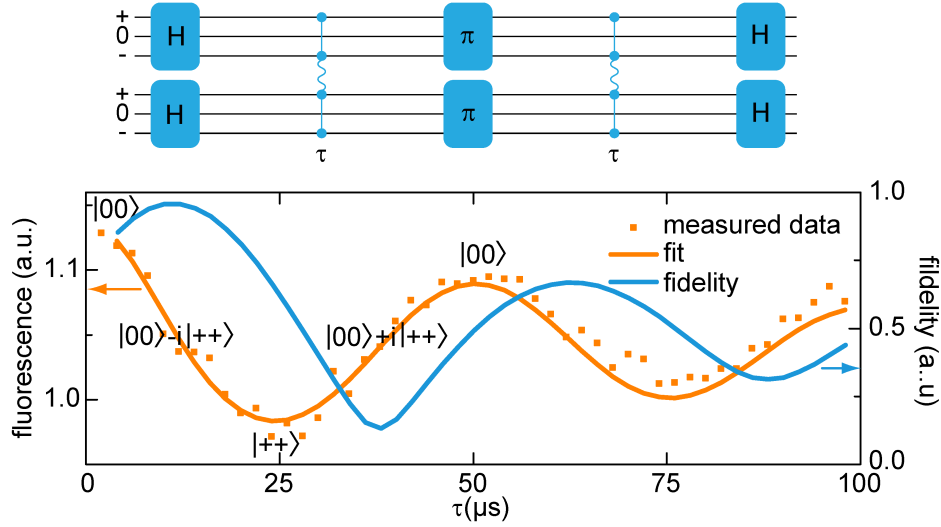
Figure 7.9.: Time evolution of the entanglement scheme. The evolution time τ was varied yielding a coherent correlated evolution of both NV centers resulting in entangled states for the appropriate waiting times.

In order to observe quantum state evolution during the entanglement scheme, U_3 was chosen to generate the entangled state $\frac{1}{\sqrt{2}}\left(|00\rangle - i\,|++\rangle\right)$ for the proper waiting time, yielding a time evolution given by $\psi(\tau) = \cos(\phi)\,|00\rangle - i\cos(\phi)\,|++\rangle$ (see Chapter 7.4.1).

In Fig. 7.9 the fluorescence measurement of the entanglement sequence while increasing τ is shown. Please note, that the fluorescence is correlated with the population of $|0\rangle$ (see Chapter 4.1).

The measured fluorescence signal was simulated using the measured coherence times $T_{2\,\mathrm{DQ}}$ and dipolar coupling strength ν_{dip} (see Chapter 7.3) and perfect quantum gates using a Gaussian noise model. The signal amplitude A and offset y_0 were used as fitting parameters.

The simulation of the time evolution yields several points of interest. For $\tau = 0$ both NV centers are in the polarized state $|00\rangle$. For $\tau = \frac{1}{16\nu_{\mathrm{dip}}}$ the simulation yields the entangled state $\frac{1}{\sqrt{2}}\left(|++\rangle - i\,|00\rangle\right)$. $\tau = \frac{1}{8\nu_{\mathrm{dip}}}$ yields a π rotation into the polarized $|++\rangle$ For $\tau = \frac{3}{16\nu_{\mathrm{dip}}}$ again an entangled state $\frac{1}{\sqrt{2}}\left(|00\rangle + i\,|++\rangle\right)$, with a π phase difference, is created. Finally $\tau = \frac{1}{4\nu_{\mathrm{dip}}}$ yields the polarized state $|00\rangle$ again.

The simulation yields a maximal fidelity of $F_{\mathrm{sim}} = 0.89$ with respect to $\frac{1}{\sqrt{2}}\left(|++\rangle - i\,|00\rangle\right)$. However the matching of simulation and experiment is only an indication for an entangled state, the proof for an entangled state via the observation of the non-local phase evolution as well as a full state tomography can be found in Chapter 7.4.3 and Chapter 7.4.4

The simulated signal amplitude is $A_{\text{sim}} = 0.16$ while the expected signal is $A_{\text{max}} \approx 0.3$ indicating an error source independent of the decoherence process. This error source can be identified as non perfect quantum gates due to hyperfine detuning as well as unwanted crosstalk between microwave transitions, diminishing the control fidelity of the local operations U_1, U_2 and U_3. To a small extent the limited polarization of the NV center (0.98 under weak orange excitation [153]) also affects the possible state fidelity. The diminished control fidelity will be addressed in Chapter 7.6.

7.4.3. Non-local phase measurements
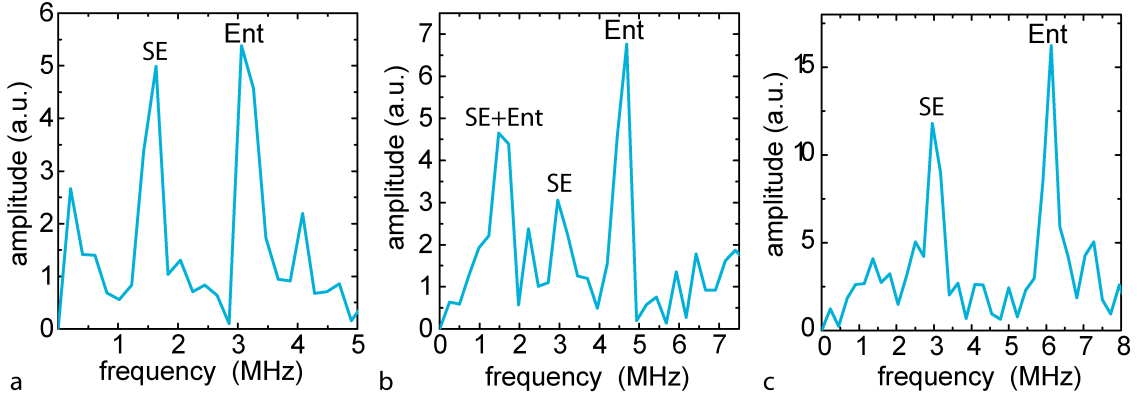
Figure 7.10.: FFT of Ramsey experiments with different entangled states. The phase evolution was investigated for a $\frac{1}{\sqrt{2}}(|++\rangle + |00\rangle)$ (**a.**), a $\frac{1}{\sqrt{2}}(|++\rangle + |0-\rangle)$ (**b.**) and a $\frac{1}{\sqrt{2}}(|++\rangle + |--\rangle)$ state (**c.**). SE indicates a single quantum evolution while Ent indicates a peak corresponding to an entanglement coherence.

Due to the non-local nature of the entangled state, the phase accumulated by it is a collective phase (i.e. it is influenced by the energy levels of both spins). Therefore the phase evolves proportional to either the sum or the difference of the local spin transitions / Larmor frequencies [154].

For the experiments conducted in this work, the microwave frequency was always chosen to be in the center of the hyperfine lines, generating a detuning of $\approx \pm 1.5$ MHz depending on the nuclear spin state. Since the nuclear spin is in a thermal state, no different signal for a Ψ or Φ could be observed. However as shown in Fig. 7.10, a different phase accumulation for different coherence types could be demonstrated. For single quantum coherences ($\Delta m_S = 1$) the detuning responsible for the phase accumulation is $\delta\nu_{\text{SQ}} \approx 1.5$ MHz. For a double quantum coherence ($\Delta m_S = 2$) it is $\delta\nu_{\text{DQ}} \approx 3.0$ MHz (see Chapter A.8). This allows for entanglement peaks at 0 MHz and 3 MHz for a $\frac{1}{\sqrt{2}}(|++\rangle + |00\rangle)$ state. For $\frac{1}{\sqrt{2}}(|++\rangle + |0-\rangle)$ the entanglement coherence peaks are at 1.5 MHz and 4.5 MHz. For the double quantum entangled state $\frac{1}{\sqrt{2}}(|++\rangle + |--\rangle)$ the peaks are at 0 MHz and 6 MHz.

In Fig. 7.10 also the local frequencies attributed to a single NV evolution are visible. This is due to pulse errors in combination with one NV being in the neutral charge state. Therefore the local phase evolution can be suppressed either with charge state preselection (see Fig. 7.11) or by suppressing pulse errors with e.g. optimal control (see Chapter 7.6.6).

The life time of an entangled state can also be determined using a phase evolution measurement. Fitting the long evolution measurement seen in Fig. 7.12 yields $T_{\Phi\,\text{DQ}} = 28.2 \pm 2.2$ μs and $T_{\Psi\,\text{DQ}} = 23.7 \pm 1.7$ μs.
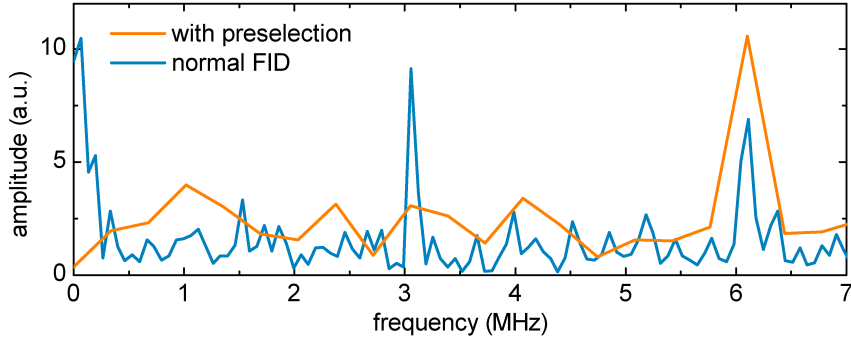
Figure 7.11.: Phase evolution of the $\frac{1}{\sqrt{2}}(|++\rangle + |--\rangle)$ state. The blue curve is a measurement without charge state detection with a peak at 3 MHz attributed to a single NV double quantum evolution with the other NV being in the neutral charge state. The peak at 6 MHz is due to the collective phase accumulation of the entangled state. The orange line is with charge state pre-selection, where only the collective phase peak at 6 MHz is observed.
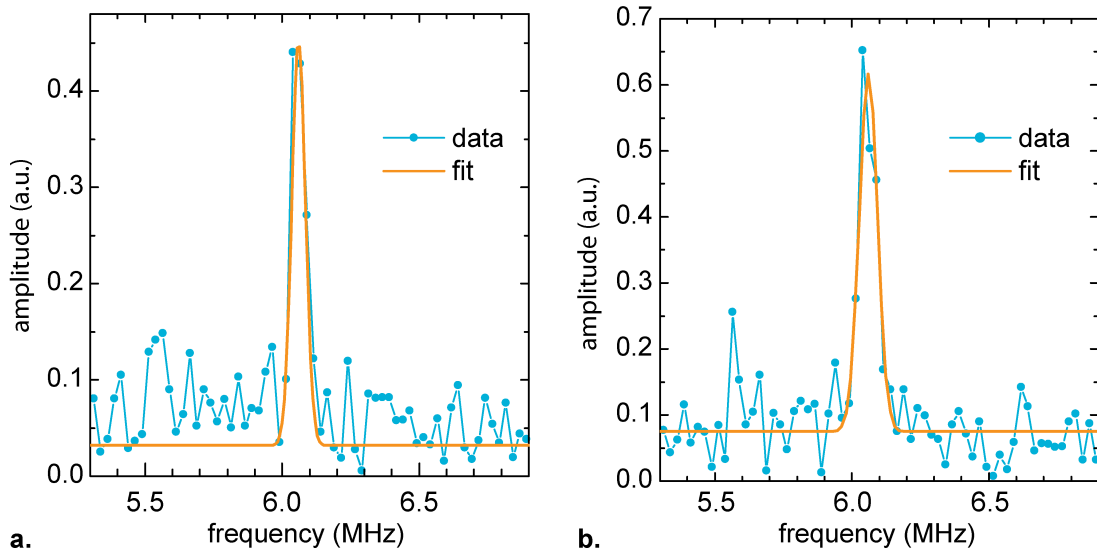

Figure 7.12.: Entanglement life time. a. FFT of a Ramsey experiment with $\Phi_{DQ} = \frac{1}{\sqrt{2}}(|++\rangle + |--\rangle)$ state. **b.** FFT of a Ramsey experiment with $\Psi_{DQ} = \frac{1}{\sqrt{2}}(|+-\rangle + |-+\rangle)$ state. The peak line width was fitted in order to determine the entanglement life time.

7.4.4. Tomography

In order to gain access to the density matrix of a system a state tomography has to be performed. Here a subset of measurements is used to determine the full density matrix. First the local density matrix populations $\hat{\rho}^{NV1}$ and $\hat{\rho}^{NV2}$ are determined. These are then correlated by a correlation measurement to reconstruct the main diagonal of the full density matrix ρ. In a last step, the NV-NV entanglement coherences are probed using non-local phase measurements (Chapter 7.4.3).

Reconstruction of the main diagonal
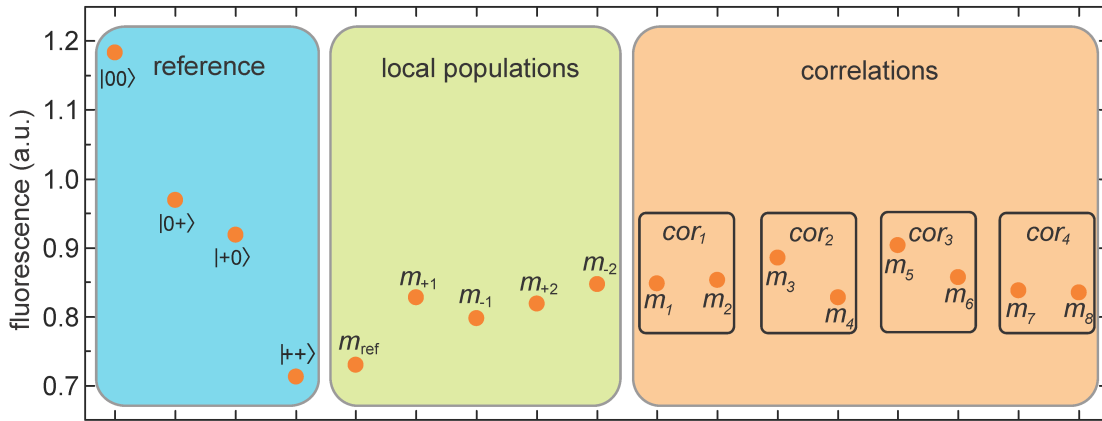
Figure 7.13.: Main diagonal tomography. The measurement can be broken down into 3 different measurement types. The blue data is the reference measurement used to determine the contrast of the individual NV centers. The green part corresponds to the local population measurements. m_{+1} indicates a measurement with an added π pulse on the $|0\rangle \leftrightarrow |+\rangle$ transition on NV 1. The orange part shows the correlation measurement data. Relative measurements are used to gain the correlation between local populations.

Please note that we can only distinguish state $|0\rangle$ from $|\pm\rangle$. The populations in states $|\pm\rangle$ cannot be discriminated directly; first they need to be swapped with the $|0\rangle$ population which can then be measured. In order to prevent any effects from the charge state of the NV center, measurements were performed with charge state pre-selection [50]. The complete measurement to reconstruct the main diagonal entries ρ_i (i.e. all entries $\rho_{i,j}$ with $i = j$ and $i,j \in \{--, -0, -+, 0-, 00, 0+, +-, +0, ++\}$) was conducted in one measurement run to be able to weight the different measurements against each other without possible drift effects in the detection optics. The measured data shown in Fig. 7.13 consists of the following subsets: first a reference measurement is performed to determine the fluorescence signal for $|00\rangle$, $|\pm0\rangle, |0\pm\rangle$ and $|\pm\pm\rangle$ (Fig. 7.13 blue inlay). This allows for proper normalization of the contrast of each NV center.
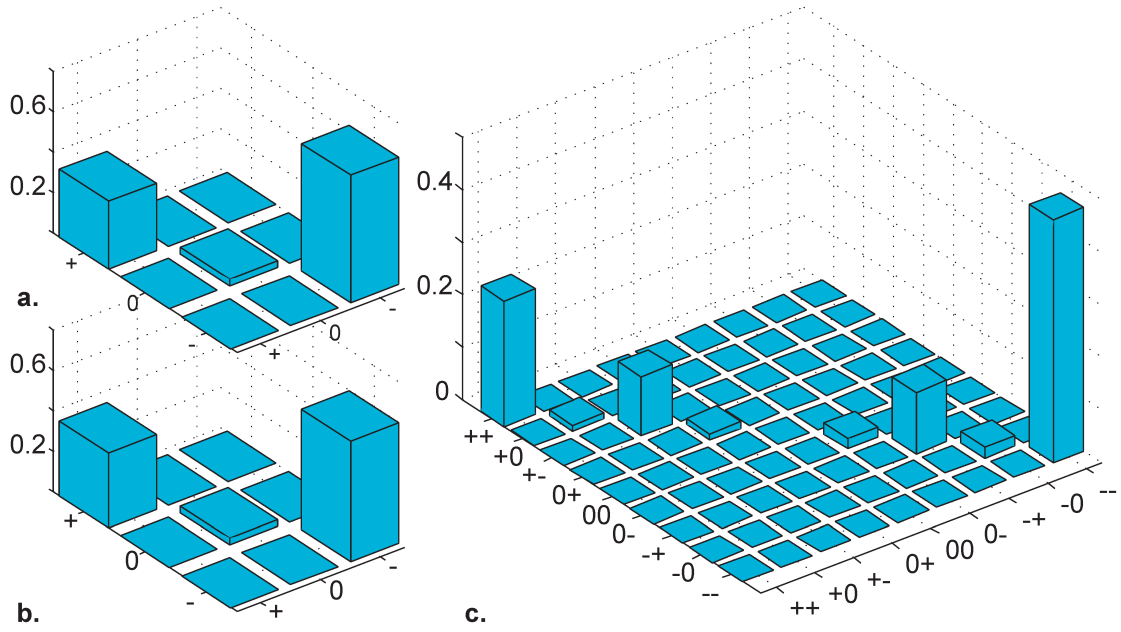
Figure 7.14.: Reconstructed populations. Reconstructed local populations of (**a.**) NV 1 $\hat{\rho}^{(\mathrm{NV1})}$ (**b.**) and NV 2 $\hat{\rho}^{(\mathrm{NV2})}$. **c.** Reconstructed populations for the global NV-NV system using local populations and correlation measurements

The local populations were then determined using local NOT gates interchanging the population $|0\rangle$ with $|\pm\rangle$ allowing them to be measured (Fig. 7.13 green inlay). These measurements allow the reconstruction of the local populations $\hat{\rho}_i^{(\mathrm{NV}k)}$ in the local density matrices $\hat{\rho}^{(\mathrm{NV1})} = \mathrm{Tr}_{\mathrm{NV2}}\,\rho$ and $\hat{\rho}^{(\mathrm{NV2})} = \mathrm{Tr}_{\mathrm{NV1}}\,\rho$, however no correlations between both NV center spin populations can be determined by this data set alone. In detail, the population of both NV centers in $|0\rangle$ is given by the measurement value

$$m_{\mathrm{ref}} = U_{\mathrm{Ent}},$$

with U_{Ent} being the entanglement gate, while the measured value

$$m_{+1} = U_{\mathrm{Ent}} - \pi_{1+}$$

$$m_{-1} = U_{\mathrm{Ent}} - \pi_{1-}$$

are related to the difference in population between $|0\rangle$ and $|\pm\rangle$. The local populations can then be calculated by

$$\hat{\rho}_+ = \frac{2\,m_{+1} - m_{-1} - m_{\mathrm{ref}} + 1}{3\,cont_1}$$

$$\hat{\rho}_- = \hat{\rho}_+ - \frac{m_{+1} - m_{-1}}{cont_1}$$

$$\hat{\rho}_0 = 1 - \hat{\rho}_+ - \hat{\rho}_-$$

where $cont_1$ is the contrast of NV 1 given by the reference measurement. The reconstructed local populations $\hat{\rho}_i^{(\text{NV}k)}$ in the local density matrices $\hat{\rho}^{(\text{NV1})} = \text{Tr}_{\text{NV2}}\,\rho$ and $\hat{\rho}^{(\text{NV2})} = \text{Tr}_{\text{NV1}}\,\rho$ are shown in Fig. 7.14 a/b.

In order to relate the local populations (shown in Fig. 7.14), the correlation between local populations $\hat{\rho}^{(\text{NV1})}$ and $\hat{\rho}^{(\text{NV2})}$ was measured. DEER type experiments were used to probe the correlation between the 2 NV centers. A correlation measurement consists of 8 measured values. They are given by

$$m_1 = U_{\text{Ent}} - \pi_{2+}/2 - \tau - \pi_{2+} - \pi_{1+} - \tau - \pi_{2+}/2, \tag{7.2}$$

$$m_2 = U_{\text{Ent}} - \pi_{2+}/2 - \tau - \pi_{2+} - \tau - \pi_{1+} - \pi_{2+}/2, \tag{7.3}$$

$$m_3 = U_{\text{Ent}} - \pi_{2+}/2 - \tau - \pi_{2+} - \pi_{1-} - \tau - \pi_{2+}/2, \tag{7.4}$$

$$m_4 = U_{\text{Ent}} - \pi_{2+}/2 - \tau - \pi_{2+} - \tau - \pi_{1-} - \pi_{2+}/2, \tag{7.5}$$

$$m_5 = U_{\text{Ent}} - \pi_{2-}/2 - \tau - \pi_{2-} - \pi_{1+} - \tau - \pi_{2-}/2, \tag{7.6}$$

$$m_6 = U_{\text{Ent}} - \pi_{2-}/2 - \tau - \pi_{2-} - \tau - \pi_{1+} - \pi_{2-}/2, \tag{7.7}$$

$$m_7 = U_{\text{Ent}} - \pi_{2-}/2 - \tau - \pi_{2-} - \pi_{1-} - \tau - \pi_{2-}/2, \tag{7.8}$$

$$m_8 = U_{\text{Ent}} - \pi_{2-}/2 - \tau - \pi_{2-} - \tau - \pi_{1-} - \pi_{2-}/2. \tag{7.9}$$

For $\tau = 100\,\mu$s the phase accumulation due to the other NV corresponds to π leading to maximal contrast. In order to cancel the effect of the nuclear spin, τ was adjusted to a revival of the nuclear spin induced modulation (see Chapter A.8). The even numbered measurements are reference measurements, where the π pulse on NV 1 is after the second evolution time. Taking into account the reference measurements, the correlation between the NV center populations can be calculated by:

$$cor_1 = m_1 - m_2$$

$$cor_2 = m_3 - m_4$$

$$cor_3 = m_5 - m_6$$

$$cor_4 = m_7 - m_8$$

In general, the correlation probes the population difference between $|0\rangle$ and $|\pm\rangle$ of NV2 and correlates it to the population difference of NV1 for $|0\rangle \leftrightarrow |+\rangle$ and $|0\rangle \leftrightarrow |-\rangle$. Since $|\pm\rangle$ were used as the qubit basis the population in $|0\rangle$ is almost zero. Therefore the measured correlation can, with only a small error, be attributed to the $|\pm\rangle$ population. This allows us to reconstruct the main diagonal of the density

matrix by weighting the local population of NV2 ($|+\rangle$ for this example) with cor_1 and cor_2. Since the evolution times and pulse performance was identical, the relative measure suppresses effects from decoherence and pulse errors. The reconstructed population correlation is shown in Fig. 7.14c.

Reconstruction of Coherence
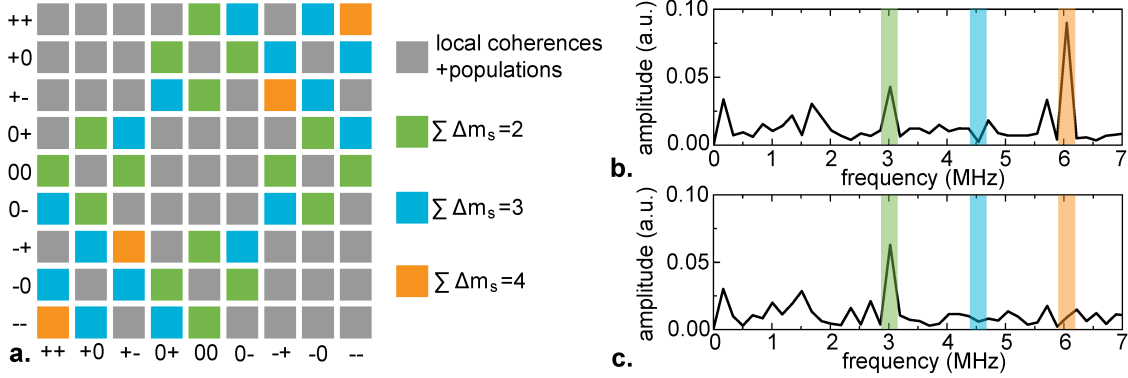
Figure 7.15.: Evolution of collective phase of entangled state. a, Density matrix of the NV-NV system color-coded to show the phase evolution frequencies. The NV-NV entanglement coherences are shown in green, orange and blue while the grey fields correspond to single NV coherences and populations. For all measurements, the detuning is chosen to be $\delta\nu = \pm 1.5$ MHz. The expected collective phase oscillation is given by $\sum \Delta m_S \cdot 1.5$ MHz. **b,** Fast Fourier transformed (FFT) phase evolution measurement of a $\Phi^+_{DQ} = \frac{1}{2}(|++\rangle + |--\rangle)$ entangled state. The peak at 6 MHz corresponds to the phase evolution of the entangled state ($\sum \Delta m_S = 4$). The peak at 3 MHz corresponds to the single spin evolution due to NV^0 and pulse errors. **c,** FFT of an evolution of desired initial entangled state $\Phi^+_{DQ} = \frac{1}{2}(|++\rangle + |--\rangle)$ altered to $\Phi^+_{DQ} = \frac{1}{\sqrt{2}}(|+0\rangle + |--\rangle)$. The back transformation was carried out using the reverse entanglement gate of the Φ^+_{DQ} state. The collective phase of the altered state should evolve at 4.5 MHz (blue line, ($\sum \Delta m_S = 3$) but we are only probing the 6 MHz phase frequency ($\sum \Delta m_S = 4$, orange line)). As expected for an ideal initial entangled state no peak at 4.5 MHz and 6 MHz is visible. The only peak visible is the 3 MHz peak due to charge state and pulses errors.

Local coherences were measured by Ramsey type experiments

$$U_{\text{Ent}} - \tau - \pi_{1+}/2$$

$$U_{\text{Ent}} - \tau - \pi_{1-}/2$$

$$U_{\text{Ent}} - \tau - \pi_{1-} - \pi_{1+}/2$$

$$U_{\text{Ent}} - \tau - \pi_{2+}/2$$

$$U_{\text{Ent}} - \tau - \pi_{2-}/2$$

$$U_{\text{Ent}} - \tau - \pi_{2-} - \pi_{2+}/2$$

Since the local coherences were smaller than the noise level, only an upper bound could be determined experimentally.

In order to measure the global NV-NV coherences, a free evolution measurement was used given by:

$$U_{\text{Ent}} - map - \tau - U_{\text{Ent}}^{-1}$$

where *map* are different mapping pulses to access all possible coherences. To reduce the measurement time, only the $|++\rangle + |--\rangle$ coherence was measured with charge state pre-selection (CS). The other measurements were weighted against the $|++\rangle + |--\rangle$ without CS allowing to relate their amplitude.

Fig. 7.15 shows the necessary measurements to determine all NV-NV coherences. To measure the other NV-NV coherences, the generated entangled state is altered by local quantum gates, after an evolution time, to shift the target coherence onto the $\sum \Delta m_S = 4$ phase (e.g. a π pulse on NV B on the $m_S = 0 \leftrightarrow -1$ transition to check for a possible $1/\sqrt{2}\,(|-0\rangle + |++\rangle)$coherence) allowing the reverse entanglement gate ENT^{-1} to map it into a population difference. The amplitude at the respective phase frequency depends on the probed NV-NV coherence (see Fig. 7.15a) and can be related to the target phase of the initial entangled state. The detuning of the microwave transitions was chosen to be ± 1.5 MHz (in the center of the hyperfine interaction of the ^{15}N). The measured peak intensity is shown in Fig. 7.16.
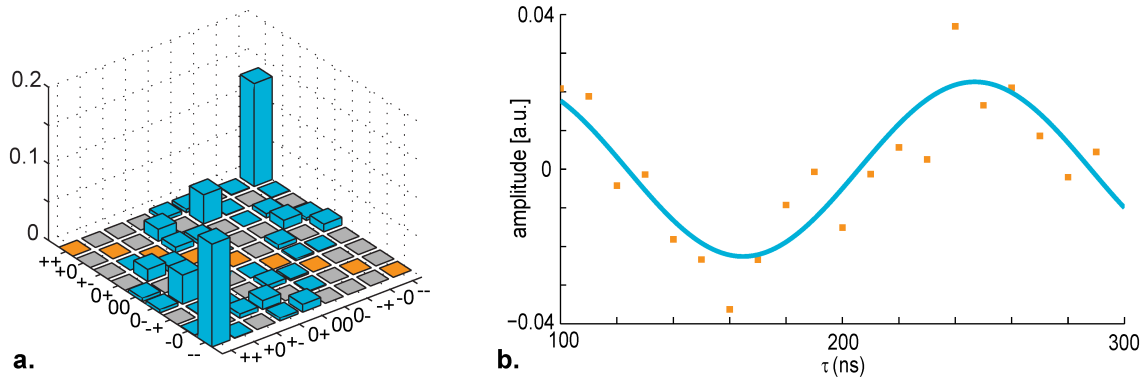
Figure 7.16.: Entanglement coherences tomography. a. The blue bars represent the measured oscillation amplitude at the frequency derived from Fig. 7.15. The gray bars are local coherences and the orange bars are the populations. **b.** measured collective phase evolution of the $\Phi_{DQ}^+ = 1/\sqrt{2}\,(|--\rangle + |++\rangle)$ state with charge state pre-selection.

Finding the closest physical state

The density matrix generated by the state tomography is due to measurement uncertainty not a physical state. In order to find the physical state closest to the measured density matrix, a scheme based on the maximum likelihood approach was

implemented. An error function is used which is given by

$$E\left(\rho_{\text{phys}}\right) = \sum_{i,j} \left|\left\{\rho_{\text{meas}}(i,j) - \rho_{\text{phys}}(i,j)\right\}\right|^2 \tag{7.10}$$

where ρ_{meas} is the density matrix reconstructed from measurement data and ρ_{phys} is the density matrix of a physically possible state. The error function $E\left(\rho_{\text{phys}}\right)$ is minimized numerically by varying ρ_{phys} to find the closest physical state.

Density matrix of the entangled state and entanglement measures
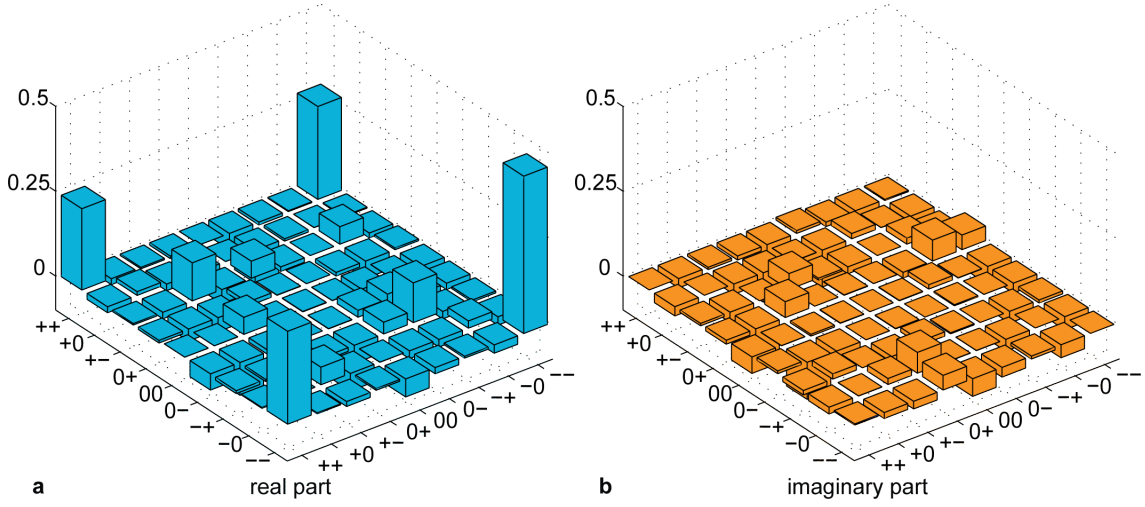
Figure 7.17.: Density matrix of $\Phi_{DQ}^+ = 1/\sqrt{2}\,(|--\rangle + |++\rangle)$. **a.** real and **b.** imaginary part of the measured density matrix.

With a tomography measurement (see Chapter 7.4.4) it is possible to reconstruct the density matrix of the generated $\Phi_{DQ}^+ = 1/\sqrt{2}\,(|--\rangle + |++\rangle)$ state. The fidelity of the entanglement generation is $F = 0.67 \pm 0.04$ (fidelity is defined as $F = \langle\Psi_{\text{target}}|\rho_{\text{meas}}|\Psi_{\text{target}}\rangle = \text{Tr}\,(\rho_{\text{meas}}\sigma_{\text{target}})$, with ρ_{meas} as the measured density matrix and Ψ_{target} as the target state e.g. $\Psi_{\text{target}} = \frac{1}{\sqrt{2}}(|++\rangle - i\,|--\rangle))$. In this case, a fidelity $F > 0.5$ is a sufficient condition for an entangled state.

A more direct measure introduced by Vedral et al. is based on von Neumann relative entropy introduced in reference [155]. Here the minimal relative entropy "distance" between the observed state (ρ_{meas}) and the closest separable state ($\sigma = \sum_i p_i \rho_{1,i} \otimes \rho_{2,i}$, where $\rho_{1/2}$ are reduced density matrices of NV 1 and NV 2) and p_i scalars between 0 and 1, is used as an entanglement measure. $E\,(\rho_{\text{meas}}||\sigma) = \min_{\sigma\in\text{separable}}\text{tr}\,(\rho_{\text{meas}}\ln(\rho_{\text{meas}}/\sigma)) \approx 0.16$ (0 for no entanglement, $\ln 2 \cong 0.69$ for a maximal entangled state) was observed (see A.3 for more details).

However assuming perfect polarization and no pulse errors, a simulation of the entanglement gate taking into account decoherence yields $F_{\text{sim}} = 0.89$. In the literature the electron spin polarization is reported to be > 0.95 [50] for green excitation and for orange excitation (no charge state pumping) a polarization of 0.98 is reported [153]. Since the measurements were conducted with charge state preselection the polarization (orange polarization) is expected to be 0.98. Therefore the main error source has to be pulse errors, which will be addressed in Chapter 7.6.

7.4.5. Photon correlations
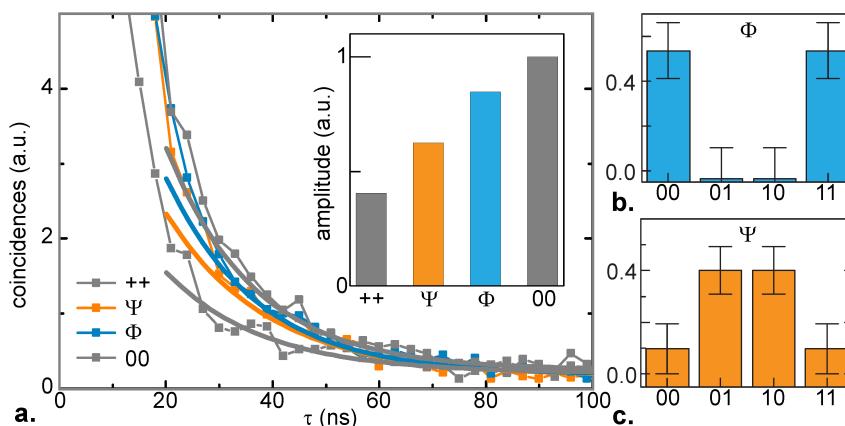
Figure 7.18.: Two-photon correlation measurements. a. Results of two-photon correlation measurement for entangled and mixed states. Photons close to the zero delay have been discarded. The inset shows the fitted two-photon probability amplitude omitting data for $\tau < 20$ ns to reduce the background. **b.** Reconstructed population correlation of a $\Phi = \frac{1}{\sqrt{2}}(|00\rangle - i|++\rangle)$ state in a reduced basis of $m_S = 0$ and $m_S = 1$. The fidelity of the main diagonal is $F(\Phi_{\text{class}}) = 1.07 \pm 0.19$. **c.** For $\Psi = \frac{1}{\sqrt{2}}(|+0\rangle - i|0+\rangle)$ the main diagonal fidelity is $F(\Psi_{\text{class}}) = 0.81 \pm 0.15$. The error bars are given by the fitting error of the photon correlation signal.

With fluorescence measurements one can only determine the mean population of both NVs. However no information about the population correlation is obtained. This changes drastically, when two photon events are considered. Here the classical correlation between the population of two NV centers can be analyzed. Please note, that the two photon correlation measurements are based on different photon emission properties for $|0\rangle$ and $|\pm\rangle$. Since $|+\rangle$ and $|-\rangle$ have identical photon emission possibilities, no correlation between these states without the use of spin manipulation is obtainable. Therefore we will only consider a state subset given by $|0\rangle$ and $|+\rangle$ (this is justified, since state preparation has well enough fidelity, see Chapter 7.4.4). When two photon events are considered, only the correlation between the populations is relevant, quantum mechanical phases have no influence.

The measurement principle is based on pulsed green excitation with a subsequent detection of two-photon-events. Two avalanche photodetectors in a Hanbury-Brown and Twiss configuration [156] one sending the start signal and the other the stop signal of the measurements. The start signal was gated to coincide with the laser pulse to reduce the signal from background fluorescence. By analyzing the start and stop events, it is possible to calculate the two photon emission probability in relation to one photon events (the two photon signal was normalized using the start events). In order to generate the requested spin state for analysis, a trigger signal coinciding

with the laser pulse was used to trigger state preparation. The states were generated using the standard polarization protocol (3 μs green cw laser (532 nm) followed by a waiting time of 1.5 μs) followed by spin state preparation.

Figure 7.19.: Two photon correlation sketch. Photon emission probabilities for different spin states are sketched. The bright bulb symbolizes a higher photon probability for {0} (k_0) and the dimmer bulb symbolizes a lower probability for {+} (k_+). The different photoemission pairings for ψ_{uncor}, Φ and Ψ are given.

To gain an understanding of two photon probabilities $p_{i,j}$ (i/j are the population of NV 1 and NV 2), they have to be analyzed in relation to the state dependent photon detection probabilities $k_{0/1}$ (see Fig. 7.19). For both NVs either being in {00} or {++} ({} indicating that only populations and no phases are considered, classical picture) and assuming identical photon emission rates for both NVs, they are given by:

$$p_{00} = \frac{k_0 k_0}{k_0 + k_0} = \frac{k_0}{2} \tag{7.11}$$

$$p_{++} = \frac{k_1 k_1}{k_1 + k_1} = \frac{k_1}{2}. \tag{7.12}$$

Therefore, measuring p_{00} and p_{++} allows us to extract the state dependent single photon detection efficiency. With

$$p_{0+} = p_{+0} = \frac{k_0 k_1}{k_0 + k_1} \tag{7.13}$$

all states can be analyzed into their two photon emission probabilities p_ψ For example a state with uncorrelated superpositions on both NV centers $\psi_{\mathrm{uncor}} = \frac{1}{4}(\{00\} + \{++\} + \{0+\} + \{+0\})$ is given by

$$p_{\psi_{\mathrm{uncor}}} = \frac{k_0 + k_1}{4} \tag{7.14}$$

whereas for a correlated state like $\Phi = \frac{1}{2}(\{00\} + \{++\})$ and $\Psi = \frac{1}{2}(\{0+\} + \{+0\})$ it is given by

$$p_\Phi = \frac{k_0^2 + k_1^2}{2(k_0 + k_1)} \tag{7.15}$$

and

$$p_\Psi = \frac{k_0 k_1}{k_0 + k_1}. \tag{7.16}$$

Any the populations of any classical state ϕ with the same single photon count rates

as ψ_{uncor} can be described by a superposition of the states Φ and Ψ by

$$\phi = \alpha\Phi + \beta\Psi \tag{7.17}$$

where $0 \leq |\alpha|, |\beta| \leq 1$ and $\alpha + \beta = 1$. For $\alpha = \beta = 1/2$, ϕ is uncorrelated. The values of α and β can be calculated with

$$\alpha = \frac{2(Sk_0 + Sk_1 - k_0k_1)}{(k_0 - k_1)^2} \tag{7.18}$$

$$\beta = \frac{-2Sk_0 + k_0^2 - 2Sk_1 + k_1^2}{(k_0 - k_1)^2} \tag{7.19}$$

where S is the measured signal for state $\{\phi\}$. Please note that the equation is only valid, as long as the same single photon detection efficiency is measured as for ψ_{uncor}. The fidelity of the classical state is given by

$$F(\{p_i\}\{q_i\}) = \sum_{i=1}^{n} \sqrt{p_iq_i} \tag{7.20}$$

Where p_i and q_i are probabilities of finding NV 1 and NV 2 in a certain state. This classical fidelity corresponds directly to the parameters α and β, where α is the fidelity in relation to Φ and β is the fidelity associated with Ψ.

This allows us to investigate any state with the same photon detection rate as ψ_{uncor} to be investigated for classical correlations. As a proof of principle we measured the classical correlations of the entangled states $\Phi = \frac{1}{\sqrt{2}} (|00\rangle - i |++\rangle)$ and $\Psi = \frac{1}{2} (|0+\rangle - i |+0\rangle)$ as well as $|00\rangle$, $|++\rangle$ and $\psi_{\mathrm{uncor}} = \frac{1}{2} (|00\rangle + |0+\rangle + |+0\rangle + |++\rangle)$. The fact that an uncorrelated state is supposed to have $\alpha^2 = \beta^2 = 1/2$ was used to determine the error in the measurement.

Using the different excited state lifetimes for the spin states ($\tau_0 = 23$ ns, $\tau_\pm = 12.7$ ns [55]) the signal can be further enhanced by only selecting two photon correlations with a delay larger than $\tau_\pm$. In Fig. 7.18 the time resolved photon correlation measurements are shown and the main diagonal is calculated. The rather large error bars are due to difficulties conduction the measurement (e.g. stabilization of pulsed laser, fiber coupling stabilities and background from the sample). This could in principle be prevented by using a diode based pulsed laser with a feedback power stabilization and working below the saturation power of the NV center. Additionally gating the starting photons with a time delay in relation to the pulsed laser would reduce the amount of background photons in the start signal.

As shown in Fig. 7.18, we have successfully demonstrated an all optical tomography of classical correlations of the NV center. Please note, that the measurement

of classical correlations is equivalent to the quantum mechanical detection of correlations along one measurement frame (S_z for the measured correlation). With local manipulation of the spins, the necessary correlations in S_x and S_y for a full state tomography can be mapped on a S_z correlations, accessible by the classical correlation measurement. This allows in principle for a full spin state tomography.

7.5. Entanglement storage
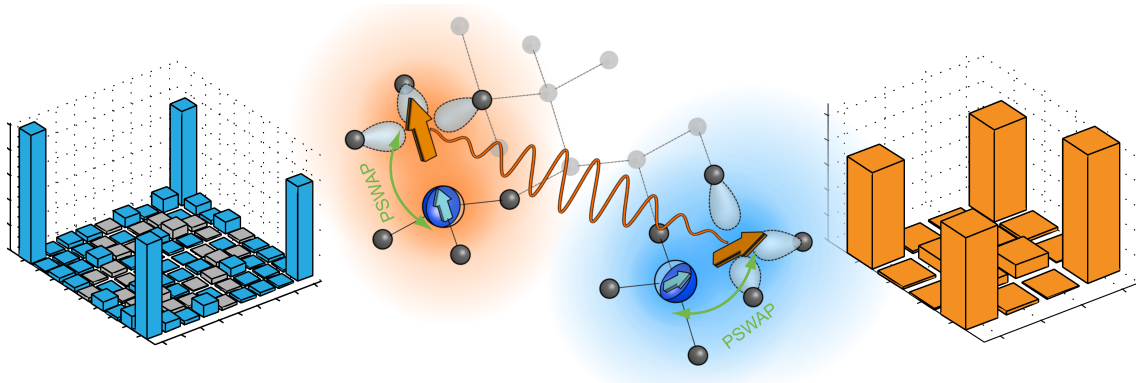
Figure 7.20.: Nuclear spin storage schematic. A PSWAP gate is used to store the electron spin entanglement in the ^{15}N nuclear spins.

The NV center has a built in quantum memory, namely the nuclear spin of the nitrogen atom. For our NV pair the nitrogen nucleus was ^{15}N with spin I=1/2. With the usage of the nuclear spin memory the entanglement life times can be enhanced to the ms time scale, only being limited by the electron spin lifetime T_1 (see Chapter 7.5.3). Recent demonstrations of decoupling experiments showed that coherence life times in the order of seconds are feasible [19]. Additionally, since the dipolar coupling between nuclear spins is in the order of a few Hz for the distance of our pair, a remote entangled state can be created by swapping the electron spin entanglement on the nuclear spins.

In order to harness the full potential of our quantum register, the $|\pm\rangle$ states of the electron spin were used as the electron spin qubit subspace. The $|0\rangle$ level is used as an ancilla level allowing for nuclear spin operations without the application of an radiofrequency driving field (see [13, 60] and Chapter 7.5.1). Additionally the use of optimal control pulses have proven to be key element to generate a high fidelity storage operation (see Chapter 7.6.5, Chapter 7.6.7 and reference [157]).

7.5.1. Nuclear spin control

In order to transfer the entanglement from the electrons to the ^{15}N nuclei intrinsic to NV centers, coherent manipulation of the nuclear spin depending on the state of the electron spin is necessary (C_eROT_n). The application of an RF field at the ^{15}N resonance frequency allows for such control. However in the setup configuration used for the experiments, it was not possible to generate a strong enough RF field at the position of the NV centers. But a combination of a magnetic field perpendicular to the NV center axis and selective pulses on the electron spin (C_nROT_e) allow for
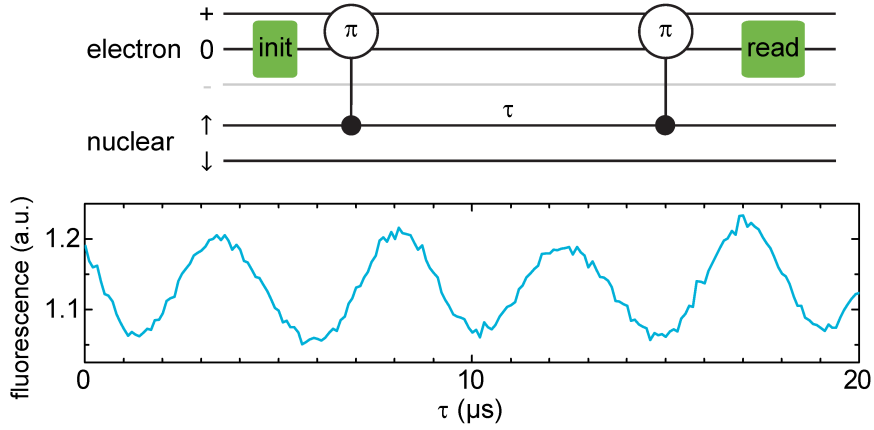
Figure 7.21.: Coherent nuclear spin state manipulation. upper panel. With the use of the $|0\rangle$ ancilla level coherent nuclear spin rotations are performed. After initializing the NV center in $|0\rangle$, the electron spin is transferred from the $|0\rangle$ to $|\pm\rangle$ conditional on the nuclear spin state by a weak microwave pulse (C_nROT_e). After the evolution time τ the nuclear spin evolution is probed by another C_nROT_e. Subsequent read out allows to detect the nuclear spin evolution. **lower panel.** Measured nuclear spin rotations facilitated by the $|0\rangle$ ancilla state.

coherent manipulation of the nuclear spin. The dynamics of the ^{15}N nuclear spin is governed by the following Hamiltonian, conditioned on the electron spin state $|0, \pm\rangle$ [13].

$$H_{^{15}N} = a_{zz}S_zI_z + \gamma_{^{15}N}\underline{\underline{B}}\underline{\underline{g}}(m_S)I \tag{7.21}$$

where $\underline{\underline{g}}(m_S)$ is the effective g-factor tensor

$$\underline{\underline{g}}(m_S) = \begin{pmatrix} 1 & 0 & 0 \\ 0 & 1 & 0 \\ 0 & 0 & 1 \end{pmatrix} - \frac{\gamma_e}{\gamma_{^{15}N}D}\left(2 - 3|m_S|\right)\begin{pmatrix} a_{xx} & a_{xy} & a_{xz} \\ a_{yx} & a_{yy} & a_{yz} \\ 0 & 0 & 0 \end{pmatrix} \tag{7.22}$$

with a_{ij} is the respective hyperfine tensor component. For ^{15}N the hyperfine interaction is given by $a_{xx} = a_{yy} = 3.65 \pm 0.03$, $a_{zz} = 3.05 \pm 0.03$ MHz and $a_{ij} = 0$ [52]. The second term of the g-factor tensor describes the enhancement effect due to the electron spin state mixing. For the electron spin in $|\pm\rangle$ states, the ^{15}N nuclear spin is well quantized along the NV-axis due to the strong hyperfine coupling to the electron spin (the first term in Eq. (7.21)). While for electron spins in the $|0\rangle$ state, the axial hyperfine coupling vanishes and the ^{15}N nuclear spin will precess about an effective field $\gamma_{^{15}N}\underline{\underline{B}}\underline{\underline{g}}(m_S = 0)$. Without loss of generality, the magnetic field can be defined to be in the x-z plane with a polar angle θ with respect to the z-axis (NV axis). In this case, the ^{15}N nuclear spin Hamiltonian reads in the eigenbasis for $|\pm\rangle$

($|\uparrow\downarrow\rangle$ pointing along z)

$$H_{^{15}N}(m_s = 0) = 1/2 \begin{pmatrix} \omega_z & \omega_x \\ \omega_x & -\omega_z \end{pmatrix} \qquad (7.23)$$

with $\omega_x = \gamma_N B \sin(\theta)(1 - \frac{2\gamma_e}{\gamma_{^{15}N}} \frac{a_{xx}}{D})$ and $\omega_z = \gamma_{^{15}N} B \cos(\theta)$. In the ideal case, where the angle θ approaches $\pi/2$, the nuclear spin exhibits perfect Rabi oscillations about the x-axis. In the realistic case, as long as the condition $|\omega_x| \gg |\omega_z|$ is satisfied, which is the case for our measurements, one will obtain a high-fidelity spin rotation. The population of $|0\downarrow\rangle$ state is given by

$$\rho_{0\downarrow} = \cos^2\left(\frac{\Omega\tau}{2}\right) + \frac{\omega_z^2}{\Omega^2}\sin^2\left(\frac{\Omega\tau}{2}\right) \qquad (7.24)$$

with $\Omega = \sqrt{\omega_x^2 + \omega_z^2}$ as the oscillation frequency as shown in Fig. 7.21.

7.5.2. PSWAP **gate**
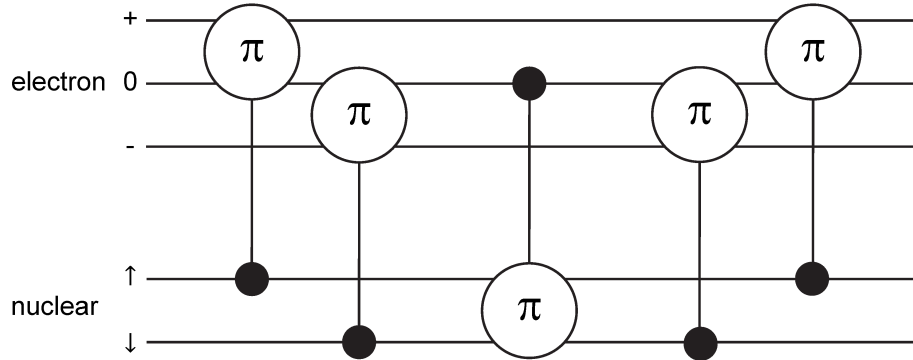
Figure 7.22.: PSWAP **gate between nuclear spin and electron spin.** The $|0\rangle$ state is used as ancilla state to facilitate controlled nuclear spin rotations. Therefore with CROT on the electron spin (nuclear spin selective π pulses) and an appropriate waiting time (nuclear spin CROT) a partial swap gate PSWAP can be implemented (swapping the states $|+,\uparrow\rangle$ and $|-,\downarrow\rangle$).

In order to store the electron spin entanglement in the nuclear spins, the quantum state has to be swapped between the electron and the nuclear spin. This is usually achieved by a swap gate ($C_e NOT_n$ - $C_n NOT_e$ - $C_e NOT_n$) with conditional π pulses (CROT, see Fig. 7.22). Since ^{15}N is a spin I=1/2 system and the NV has a spin S=1, only a partial SWAP gate PSWAP between the respective Hilbert spaces ($|\pm\rangle_S$ and $|\uparrow\uparrow\rangle_I$) can be implemented.

Without initializing, the nuclear spins are in a mixed state. For simplicity of the representation this is assumed to be a superposition state $\psi_I = \frac{1}{2}(|\uparrow\uparrow\rangle_I + |\uparrow\downarrow\rangle_I + |\downarrow\uparrow\rangle_I + |\downarrow\downarrow\rangle_I)$. Therefore for an entangled state $\Phi_{DQ}^+ = 1/\sqrt{2}\,(|--\rangle + |++\rangle)$ the inital state is given by:

$$\begin{aligned}
\psi = \Phi_{DQ}^+ \otimes \psi_I \quad &= \tfrac{1}{\sqrt{8}}[(|++\rangle_S + |--\rangle_S) \otimes |\uparrow\uparrow\rangle_I \\
&+ (|++\rangle_S + |--\rangle_S) \otimes |\uparrow\downarrow\rangle_I \\
&+ (|++\rangle_S + |--\rangle_S) \otimes |\downarrow\uparrow\rangle_I \\
&+ (|++\rangle_S + |--\rangle_S) \otimes |\downarrow\downarrow\rangle_I]
\end{aligned} \tag{7.25}$$

Applying the PSWAP gate as shown in Fig. 7.22, utilizing $|0\rangle$ to facilitate controlled

nuclear spin rotations, results in

$$
\psi = \qquad \tfrac{1}{8}[|00\rangle_S \otimes (|\downarrow\downarrow\rangle_I + |\uparrow\uparrow\rangle_I)
$$
$$
|-+\rangle_S \otimes (|\downarrow\downarrow\rangle_I + |\uparrow\uparrow\rangle_I)
$$
$$
|+-\rangle_S \otimes |\downarrow\downarrow\rangle_I + |\uparrow\uparrow\rangle_I)
$$
$$
|++\rangle_S \otimes |\downarrow\downarrow\rangle_I + |\uparrow\uparrow\rangle_I)]
$$
$$
= \tfrac{1}{2}(|--\rangle_S + |0+\rangle_S + |+0\rangle_S + |++\rangle_S) \otimes \tfrac{1}{\sqrt{2}}(|\downarrow\downarrow\rangle_I + |\uparrow\uparrow\rangle_I). \qquad (7.26)
$$

If the coherences related to the $|0\rangle$ are omitted, the electron spin coherences are fully stored in the nuclei and the electron spin wave function can be separated from the nuclear spin wave function. For perfect π pulses and no decoherence, the PSWAP efficiency is unity, however due to cross talk for the electron spin CROT and the non-perfect nuclear spin rotations, the storage efficiency is reduced. The nuclear spin state manipulation used in this work, has the best performance at a 90° angle between the NV axis and applied magnetic field. The electron spin T_2 is shortened at non-aligned magnetic fields [158] and the eigenstate polarization is reduced [66], therefore the fidelity of the entanglement creation becomes poor. As a compromise, an angle of 54.5° was chosen to demonstrate the entanglement storage leading to a reduced storage efficiency (see Chapter 7.5.1).

7.5.3. Storage of the entangled state
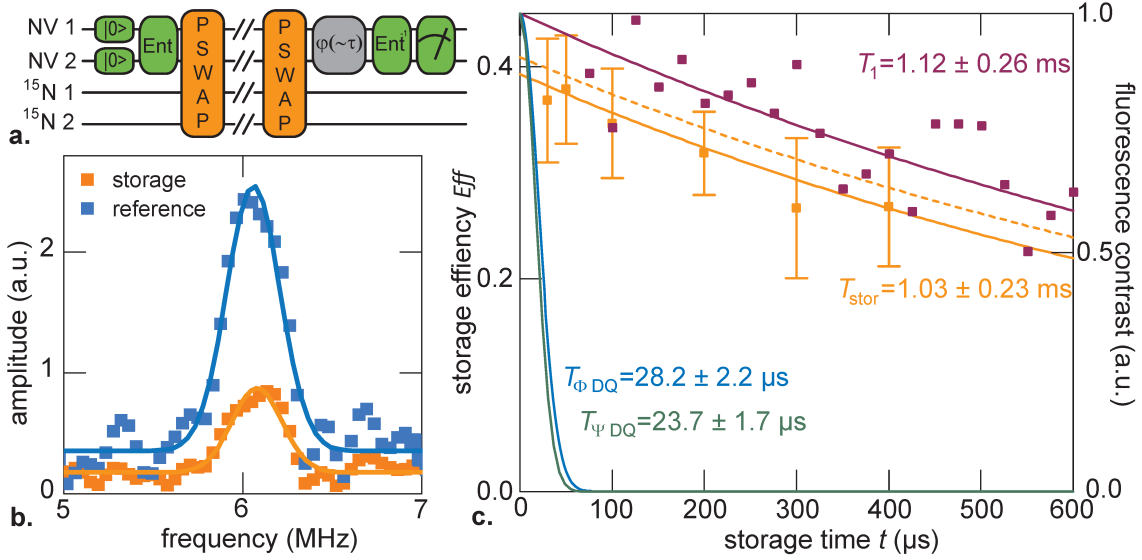
Figure 7.23.: Entanglement storage in ^{15}N. a. spin entanglement storage scheme. Selective π pulses creating a PSWAP operation store the electron spin entanglement in the nitrogen nuclear spins. **b.** FFT of a global phase evolution after storing the entanglement (orange) and a reference measurement without entanglement storage (blue). **c.** Entanglement recovery efficiency depending on the storage time is shown in orange. The thin orange line is the exponential fit of the storage efficiency. Magenta dots and line are the measurement and fit of T_1. The blue and green lines are entanglement lifetimes without storage.

The ^{15}N nuclear spins couple to magnetic fields much weaker than the NV electron spins, and consequently have much longer coherence times. Therefore they are ideal long-lived storage qubits [19], which are easily integrated into a register via their hyperfine coupling to the electron spin.

With the use of the PSWAP gate introduced in Chapter 7.5.2, entanglement storage was demonstrated. First a $\Phi_{\mathrm{DQ}} = 1/\sqrt{2}\,(|++\rangle + |--\rangle)$ was created on the electron spins. With a PSWAP the entangled state is then transferred to the nuclear spins. After a storage time t the entangled state is retrieved from the nuclear spins and transferred to electron spins again. After an evolution time τ, the inverse entanglement gate ENT^{-1} (see Fig. 7.8) mapped the entanglement coherence $\eta = |--\rangle\langle++|$, respectively $\eta = |++\rangle\langle--|$, to an electron spin population difference which is subsequently read out.

With an FFT of the observed non-local phase evolution during τ, the amplitude of the stored entanglement coherence $\eta_{\mathrm{stor}}(t)$ was determined (see Fig. 7.23). A reference measurement without entanglement storage was used to determine the storage efficiency $Eff_{\mathrm{stor}}(t) = \frac{\eta_{\mathrm{stor}}(t)}{\eta_{\mathrm{ref}}}$ and found to be $Eff_{\mathrm{stor}}(t=0) = 0.39 \pm 0.01$. The low Eff_{stor} can be mainly attributed to the low PSWAP gate fidelity $F_{\mathrm{std}} = 0.87$

(see Chapter 7.6.5). The PSWAP gate efficiency is addressed in Chapter 7.6.5 reaching a fidelity of $F_{\text{opt}} = 0.97 \pm 0.01$

The nuclear spin entanglement decay is shown in Fig. 7.23c. The nuclear spin entanglement life time is $T_{\text{stor}} = 1.02 \pm 0.23$ ms. The electron spin life time is $T_1 = 1.12 \pm 0.26$ ms. Therefore the assumption that T_{stor} is governed by the relaxation rate of the electron spin bare merit. Due to the strong coupling between nuclear and electron spin ($a_{zz} = 3.05$ MHz), a decay of the electron spin leads to dephasing of the nuclear spin coherence. However a recent demonstration of decoupling by strong laser radiation yielded life times in the order of seconds for nuclear spins coupled to the NV electron spin. This was achieved by motional narrowing of the hyperfine interaction by a fast dynamics between NV^- and NV^0 [19]. Similar approaches (like strong driving by microwave fields) promise to extend the storage scheme to storage times also in the seconds' regime.
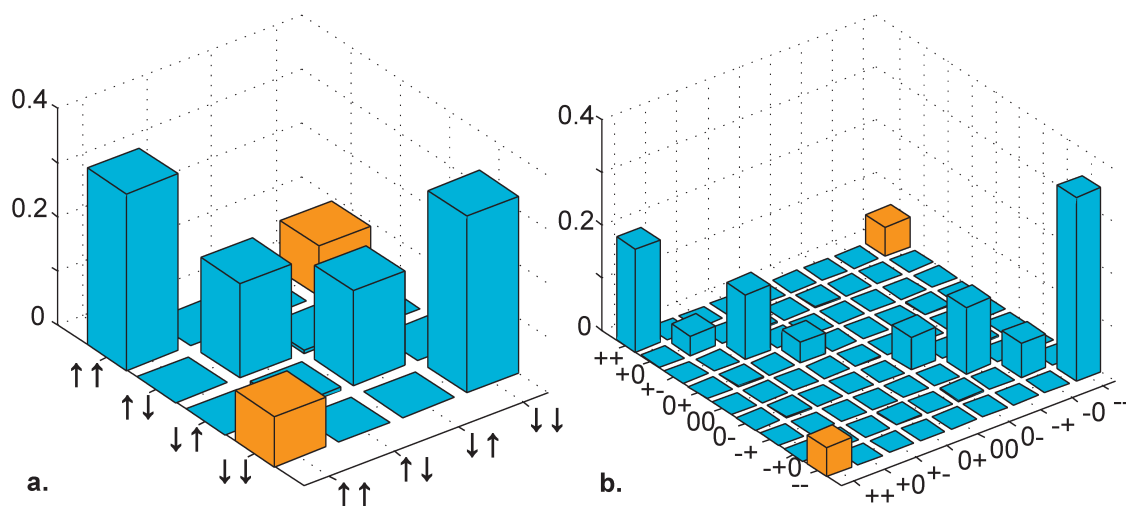
Figure 7.24.: Simulated density matrix of the stored entangled state. a. Simulated density matrix for the nuclear spin after the first PSWAP gate. **b.** simulated density matrix of the electron spin after the storage. The orange peak indicates the ^{15}N-^{15}N and the NV-NV coherence observed via the storage protocol.

In order to estimate fidelity of the nuclear spin entanglement the PSWAP gate performance was simulated. The simulations were carried out using the full NV spin Hamiltonian with the experimentally determined parameters such as coherence times as well as the limitations of the gate fidelity. The simulation of the nuclear spin and electron spin density matrix during and after storage is shown in Fig. 7.24. The simulated NV-NV coherences correspond well with the measured ones after storage (see Fig. 7.23b). Since the NV center is well understood and so far all experimental result could be reproduced by the Hamiltonian, simulations can be considered

for the evaluation of entanglement. The simulated nuclear spin entanglement fidelity is $F_{\mathrm{nuc\ sim}} = 0.42$. The calculated entanglement measure based on the simulations is $E_{\mathrm{nuc}}=0.03$ and $E_{\mathrm{retrieved}}=0.02$ (see A.3). The entanglement measure is arguably rather weak. However since they are not zero they are an indication of entanglement in the system. With the use of optimal control techniques the nuclear spin entanglement can be tremendously improved and convincing nuclear spin entanglement prepared (see Chapter 7.6.7).

7.6. High fidelity operations with optimal control

7.6.1. Introduction

As shown in Chapter 7.4 and Chapter 7.5 the achieved electron and nuclear spin gate fidelities are not limited by decoherence but by control errors. For example the entangled state generation fidelity was measured to be $F_{\Phi_{\mathrm{DQ\ stand}}} = 0.67 \pm 0.04$ with standard pulses while the best possible entangled state fidelity (limited by the coherence times (see Chapter 7.3) and the electron spin polarization (0.97 [153]) is $F_{\mathrm{max}} = 0.849$. Since high fidelity quantum operations, including gates, on-demand entangled state generation and coherent control in general, represent a fundamental prerequisite for all quantum information technologies such as error correction [18], quantum metrology [159] and of course quantum information processing [157]. Wherein the hardware and its control must satisfy the DiVincenzo criteria [25]. Therefore improving the gate fidelity is a fundamental milestone towards a scalable quantum register.

Optimal control, often seen as a central tool for turning principles of quantum theory into new technology [160], seems to be the only practical way to ensure functionality even in light of device imperfections, and to overcome several impactful features found when scaling up the register size, such as unwanted crosstalk between control fields designed for individual qubit control. It is gradually being exploited in many other experimental settings, including ion traps [161], optical lattices [162], solid-state devices [163–165], and NMR [166]. Therefore in this chapter optimal control methods for solid state spin registers are developed, to dramatically increase their utility. We implement optimal control on the NV pair introduced in Chapter 7.3 with its 36 levels to realize a fully functional 2-qubit 2-qutrit quantum register. High fidelity single- and multi-qubit operations are demonstrated. These include generating high fidelity entanglement between the electron spins and entanglement storage in nuclear spin memory. The numerical control optimization simultaneously cancels crosstalk and unwanted dipolar couplings to a high extent. This technique will find further applications in any high fidelity gate synthesis necessary for various scaling approaches devised so far (e.g [33, 167]).

Optimal control is implemented by splitting the control pulse into small sections which are numerically optimized using the gradient ascent pulse engineering algorithm (GRAPE). This allows for tailored pulses, in principle representing all possible unitary operations. This can not only be used for gate synthesis, but also to implement any possible unitary operation, as used in quantum simulation [168, 169]. The NV center can here be considered the prototype for any spin based qubits such

as phosphorus in silicon (Si:P) [170], rare earth ions in a solid state matrix [171], quantum dots [172] and other defects in diamond or silicon carbide [58, 173].

7.6.2. Challenges in control
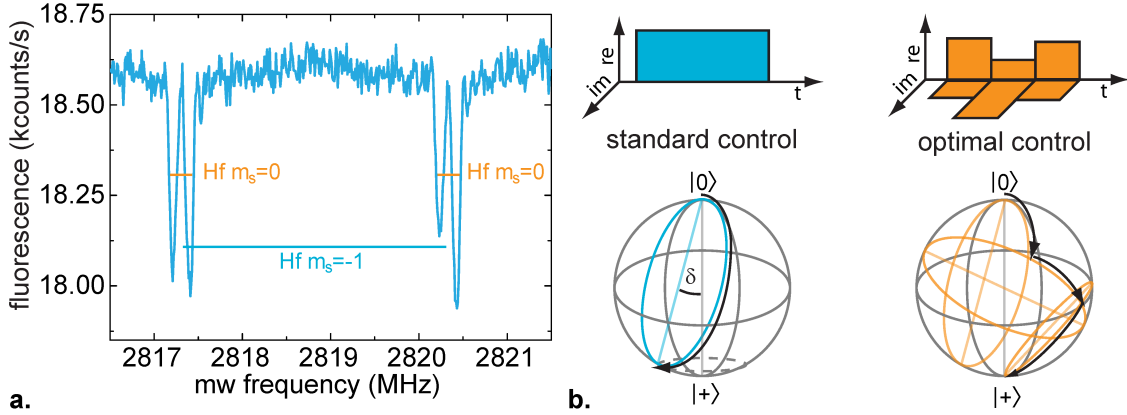
Figure 7.25.: Control challenges - detuning. a. Optically detected magnetic resonance (ODMR) spectrum of one electron spin transition split by the hyperfine interaction with ^{15}N. **b.** Schematic Bloch sphere representation of the action of standard control (blue) and optimal control (green) considering detuning effects shown for a ROT gate. Detuning leads to a tilt δ of the rotation axis . Regardless of the detuning by the hyperfine interaction, the electron spin should be inverted. Optimal control realizes this splitting the pulse into discrete time steps with different amplitude and phase as sketched in the upper part achieving a path on the Bloch sphere resulting in a full inversion of spin state.

Improving gate fidelity is a nontrivial task, the main reason for this being the high spectral density of individual qubit resonances. The interaction of a single microwave field with a spin can be described by the Rabi formula

$$p_{\text{target}}(t) = \frac{\Omega^2}{\Omega^2 + \Delta^2} \sin^2 \frac{\sqrt{\Omega^2 + \Delta^2}\, t}{2} \, , \tag{7.27}$$

giving the probability p_{target} for a spin flip into a target state. Here the Rabi frequency Ω is the strength of the applied mw field and Δ is the detuning of the mw frequency from the actual spin transition. While it seems that high fidelity control of a single transition (i.e. $p_{\text{target}} \approx 1$) can be achieved by a large ratio Ω/Δ, in the case of single-qubit gates on the electron spin (i.e. irrespective of the nuclear spin state), the hyperfine interaction sets a lower bound for the detuning Δ and the spectral density sets an upper bound for Rabi frequency Ω in order to avoid crosstalk (unwanted spin dynamics in the other spin). In our particular case the hyperfine interaction is $\approx 3\,\text{MHz}$ (see Fig. 7.25a) and the spectral separation of individual NV transitions is $\approx 30\,\text{MHz}$ (see Fig. 7.26). This limits the fidelity of a "standard" single-pulse single-qubit NOT gate to $F \approx 0.9$. These limitations can, however, be overcome using numerically optimized composite control sequences. Here a pulse consisting of sequential rotations will be used to compensate for detuning (see

Fig. 7.25b) while the overall microwave power is so low that cross talk is suppressed. In an additional step cross talk can be suppressed by designing the control sequence in a way, that the unwanted spin dynamics cancel out.
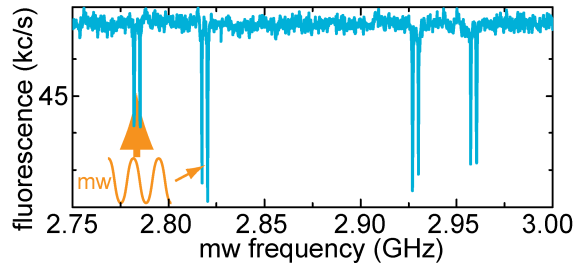
Figure 7.26.: Control challenges - crosstalk. ODMR spectrum of the full quantum register. The electron spin transitions are split by the hyperfine interaction and are roughly $\approx$ 30 MHz detuned. Due to the low separation of the resonance lines a microwave supposed to be selective to one spin transitions is also affecting others.

An additional error source is the nontrivial nuclear spin dynamics in $|0\rangle$. If the magnetic field is not aligned with the NV axis, the electron spin dependent change in the eigenbasis of the ^{15}N nuclear spin leads to coherent nuclear spin rotation for $|0\rangle$ (see Chapter 7.5.1). While this can be utilized for control of the nuclear spin, it degrades the local gate fidelity if the nuclear spin should stay constant. However with an accurate modeling of the system, the controlled rotations of the nuclear spin can be taken into account and disjoint gates only acting on one qubit can be constructed.

7.6.3. Designing optimal pulses with GRAPE

We use the gradient ascent pulse engineering algorithm (GRAPE [36]) optimization to generate optimal control pulses. In order to optimize the control pulse, it is split in N different segments. The time evolution under each segment can be described by the unitary operator

$$U_j = e^{-it_j\left(H_0 + \sum\limits_{k=1}^{m} u_k(t_j)H_k\right)}, \qquad (7.28)$$

with t_j the time length of the pulse segment U_j, H_0 the free evolution Hamiltonian, H_k the microwave (mw) corresponding Hamiltonians (one for each mw control frequency k) and $u_k(t)$ the complex control parameter of the

Figure 7.27.: GRAPE working principle. Sketch of the iterative gradient ascent pulse engineering algorithm (GRAPE) used to generate the optimal control pulses

mw field determining amplitude and phase. Please note that the microwave control fields are all real, the complex control parameter $u_k(t)$ is used to describe the amplitudes of two microwave fields at the same frequency but with a 90° phase shift (x and y microwave field). The state $\rho(T)$ after the application of the control pulse is then given by

$$\rho(T) = U_N...U_1\rho_0 U_1^\dagger....U_N^\dagger, \qquad (7.29)$$

with $T = \sum\limits_{j=1}^{N} t_j$ as the total pulse length. With the performance function ϕ

$$\phi = \langle C | \rho(T) | C \rangle, \qquad (7.30)$$

with $|C\rangle$ as the target state, the proximity of the control pulse to the target operator can be obtained. With the calculation of the derivative of the performance function ϕ with respect to the mw control parameter $u_k(t)$, the later can be improved by

$$u_k(j) \rightarrow u_k(j) + \epsilon\frac{\partial\phi}{\partial u_k(j)}, \qquad (7.31)$$

with ϵ as a small step size.

As shown in Fig. 7.27 the working principle is as follows: First start with an initial guess. Then by calculating the gradient of the performance function $\epsilon\frac{\delta\phi}{\delta u_k(j)}$ update the control parameters $u_k(t)$. This is repeated iteratively till ϕ is above an acceptable

threshold.

For this optimization method to work, the Hamiltonians have to be described as precisely as possible. To match the simulations with experimental realities, the magnetic field was determined precisely (see A.4) and the response of the NV center to different microwave fields (see A.5) was calibrated carefully to account for any non-linear response in microwave transmission and amplification.

7.6.4. Single qutrit control
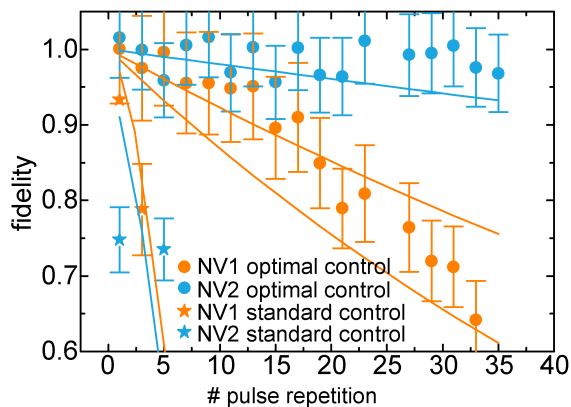
Figure 7.28.: Control of a single qutrit in a dense spectrum. Repeated application of a ROT gate targeted on the electron spin of NV 1, implemented using a standard π-pulse (stars) as compared to an optimized gate (filled circles). With an odd number of applications the effect should always be the same (spin flipped for NV 1, unchanged for NV 2). The fidelity with respect to these target states is displayed for both spins (orange and blue). Where optimal control pulses allow for at least 20 repetitions without a significant loss of fidelity and negligible crosstalk within our measurement error, standard π-pulses show low fidelity and strong crosstalk already after the first gate application. Error bars are given by the photon shot noise of the measurement used to calculate the fidelity.

As a first benchmark of the optimal control pulses created by GRAPE, a standard ROT operation in a dense spectrum is investigated. In order to be able to investigate small deviations in the pulse performance, the NOT gate to the electron spin of NV1 interrupted by a small free evolution time $\left(\left[\pi_{\text{optimal/standard}} - \tau_{\text{free evolution}} -\right]^{2k+1}\right)$ is applied repetitively. Only odd numbers of pulses are applied to simplify the interpretation of the measurement data. A state tomography identical to the local tomography described in Chapter 7.4.4 was used.

The NV centers are initialized into state $\left|m_S^{\text{NV1}}, m_S^{\text{NV2}}\right\rangle = |00\rangle$. If the applied gate is perfect, the state of NV 1 always results in $|+\rangle$ and that of NV 2 in $|0\rangle$, neglecting decoherence. However for standard control with rectangular time-domain pulses with $\Omega_{\text{Rabi}} = 10$ MHz, the experimental results show a fast decay of population in $|+\rangle$ for NV1 and a strong crosstalk effect on NV2 (i.e. decrease of population in $|0\rangle$) (Fig. 7.28). In contrast, for optimal control the decay is much slower and almost no crosstalk is observed for 35 applications of the NOT gate. A fidelity between 0.9851 and 0.9920 for the optimal NOT gate on NV1 and 0.9985 for the identity gate on NV2 are achieved by fitting the experimental results. This is with good agreement with the simulated gate fidelity of ≈ 0.99.

7.6.5. PSWAP **gate as an example for 2 qubit control**

a.

b.
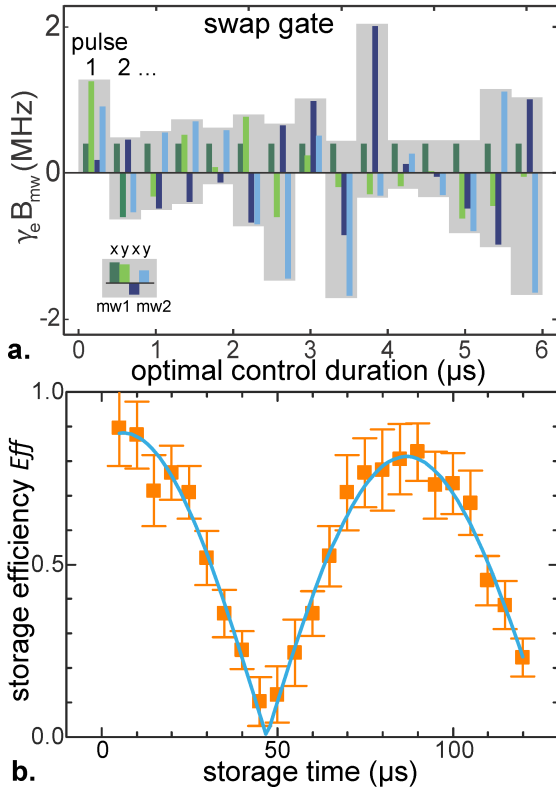
Figure 7.29.: PSWAP **gate between electron spin and nuclear spin. a.** Optimal control PSWAP gate consisting of 15 rectangular pulses (gray bars) each $0.4\,\mu$s long. Each pulse has two frequency components, corresponding to transitions $|0\rangle \leftrightarrow |+\rangle$ (mw1, green) and $|0\rangle \leftrightarrow |-\rangle$ (mw2, blue). In addition, each frequency component (mw1, mw2) has an in-phase and an out-of-phase amplitude (dark, bright). All four contributions to a single pulse are applied simultaneously during the whole pulse duration. **b.** The retrieved superposition state reveals the free evolution during quantum state storage. Here we show the $|\langle I_x \rangle|$ component of the stored coherence. The Larmor precession of the nuclear spin superposition state leads to a phase accumulation. Error bars are given by errors of the fit of the phase amplitude and the shot noise of the reference measurement.

In order to benchmark the performance of electron nuclear spin gates a PSWAP gate was implemented as described in Fig. 7.22. Again a nonperpendicular magnetic field in combination with the $|0\rangle$ ancilla level was used to implement controlled rotations on the ^{15}N spin (see Chapter 7.5.1). Due to a polarization of the spin for $|0\rangle$, in the current experiment the effective field responsible for the nuclear spin rotations is almost perpendicular to the NV axis allowing for high fidelity control. Having at hand controlled rotations for electron and nuclear spins, we can design a partial SWAP gate (PSWAP , exchanging the states $|+ \uparrow\rangle$ and $|- \downarrow\rangle$) for quantum information storage. The standard approach is a sequence of rectangular time-domain pulses (Fig. 7.22). However, the imperfections of each operation will accumulate and largely reduce the performance of the gate. The optimal control PSWAP was designed as one operation and is shown in Fig. 7.29a.

For the standard PSWAP gate, CROT operations on the electron spin were implemented by weak mw pulses (Ω_{crot} = 0.5 MHz, $a_{HF} \approx$ 3 MHz). However since the microwave strength Ω_{crot} is limited by the decoherence time T_2^*, it is not possible to construct CROT operations on the electron spin without a significant amount of crosstalk limiting the gate fidelity drastically. Therefore the storage efficiency was limited to $Eff_{std} = 0.50 \pm 0.07$. This corresponds to a PSWAP gate fidelity of $F_{std} = 0.87$

Optimal control allows for tailoring a PSWAP gate with a significantly better performance compared to the standard approach (Fig. 7.29b). A storage efficiency of $Eff_{\text{opt}} = 0.89 \pm 0.01$ was measured (corresponding to $F_{\text{opt}} = 0.97 \pm 0.01$). Eff_{opt} is limited by decoherence (T_2^*) during the PSWAP operation. In principle this can be compensated by implementing decoupling protocols into the PSWAP gate allowing for T_2 limited swap efficiencies. The oscillation of the storage efficiency shown in Fig. 7.29b reveals the Ramsey oscillation $e^{-i\omega_n t}$ of the nuclear spin due to the axial Zeeman shift with $\omega_n = \gamma_n B_{\parallel}$.

7.6.6. Improving the entanglement sequence with optimal control
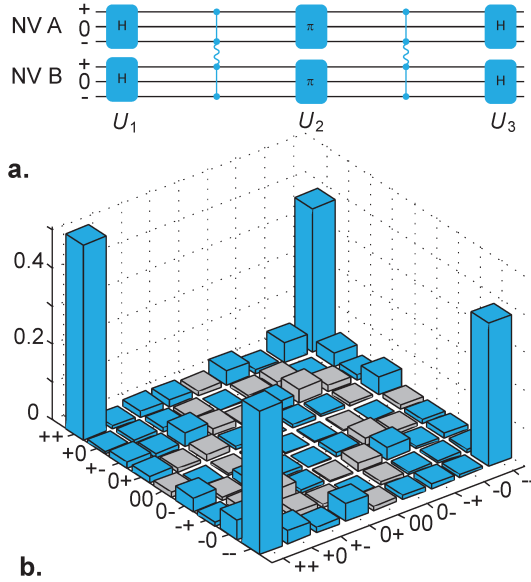
Figure 7.30.: Electron spin entanglement. a. Quantum wire diagram of the entanglement sequence. **b.** Density matrix of the created Bell state $|\Phi_{DQ}\rangle = |++\rangle + i |--\rangle$ (F=0.824 ± 0.015). The blue columns represent measured values. Please note that except for the main four columns representing the entangled state and the entries $|+-\rangle\langle+-|$ and $|-+\rangle\langle-+|$, all other values are given by the shot noise of the measurement process. The gray columns are upper bounds given by the measured main diagonal entries and the requirements for a physical state.

In order to improve the electron spin entanglement demonstrated in Chapter 7.4, the composite unitary operations U_1, U_2 and U_3 used in standard control (see Fig. 7.8) were replaced by three tailored optimal control operations. Thereby 16 imperfect local π pulses are replaced by 3 optimal control pulses. As shown in Chapter 7.6.4, the individual standard π pulse has a fidelity of about $F_{\text{stand}} = 0.95$ and a rather large cross talk component. Therefore the entanglement generation between two NV centers (see Chapter 7.4) is severely compromised reducing the fidelity down to $F_{\text{std}} = 0.67 \pm 0.04$.

Taking into account the modest coherence times (see Chapter 7.3) and the initial spin polarization (here 0.97 for each electron spin [153]), the theoretical upper bound for the gate fidelity is $F_{\text{lim}} \approx 0.849$.

By replacing the composite unitary operation with three numerically optimized local gates (16 rectangular mw pulses exchanged for 3 tailored pulses), it was possible to improve the fidelity up to $F_{\text{opt}} = 0.824 \pm 0.015$ which reaches the limit set by decoherence and initialization.

The entanglement was quantified using the von Neumann relative entropy based measure introduced by Vedral et al (see reference [155] and A.3) With the improved pulse fidelity, an entanglement of $E_{\text{electron}} \approx 0.37$ (out of the ideal $E(|\Phi_{\text{dq}}\rangle) = \ln 2$) was calculated. This demonstrates a significant improvement (a factor of about two) of the NV-NV electron spin quantum correlation in comparison with standard control (see Chapter 7.4), yielding only $E_{\text{std}} \approx 0.16$.

7.6.7. Nuclear spin entanglement with optimal control

Next entanglement storage on the nuclear spins using the PSWAP gate introduced in Chapter 7.6.5 is demonstrated. To this end, a control sequence was optimized to execute simultaneous PSWAP gates on both NV centers yielding a storage efficiency of $Eff_{\text{opt}} = 0.92 \pm 0.07$ (compared to $Eff_{\text{std}} = 0.39$ achieved with standard pulses in Chapter 7.5). The fidelity of the entangled state after storage and retrieval is $F_{\text{opt retrieved}} = 0.74 \pm 0.04$ and the density matrix shown in Fig. 7.32b. It is important to note that during the spin state storage the two remote nuclear spins are entangled. Using reconstructed electron spin density matrices before, during and after the entanglement storage (presented in Fig. 7.30b and Fig. 7.32) we can estimate the fidelity of the nuclear spin state to be $F_{\text{opt nuclear}} = 0.819$.

Figure 7.31.: Nuclear spin entanglement. Using optimal control we have swapped the entangled electron spin state onto the nuclear spins (F=0.819). The density matrix represents the entangled Bell state $|\Phi\rangle = |\uparrow\uparrow\rangle - i\,|\downarrow\downarrow\rangle$ of the two remote nuclear spins. Please note that since the entanglement was created on the electron spins and transferred to nuclear spins using PSWAP gates, no polarization or postselection is necessary to achieve nuclear spin entanglement.

The corresponding estimated density matrix of the entangled nuclear spins is shown in Fig. 7.31. During entanglement storage the nuclear spins are in a fairly pure entangled state, while the electron spins are in a mixed unentangled state due to the PSWAP gate between initialized electron spins and nuclear spins in a thermal state (see Fig. 7.32a). Therefore no post-selection is necessary. The entanglement $E(\rho)$ is again quantified by numerically minimizing the relative entropy yielding $E_{\text{nuclear}} \approx 0.23$. This is a clear indication of entanglement. Please note that the interaction between the individual nuclear spins is on the order of a few Hz, not allowing for any meaningful interaction during one measurement run, proving the feasibility of using the electron spins as a bus system while the nuclear spins can be harnessed as a long lived memory.

Tomography of the nuclear spin state

Although we can only directly measure the electron spins, it is possible to estimate the nuclear spin state via its hyperfine coupling to the electron spin, which generates the PSWAP gate we use for entanglement storage and retrieval. The electron state density matrices after the entangling sequence, entanglement storage, and retrieval are denoted by $\hat{\rho}_A$, $\hat{\rho}_B$ and $\hat{\rho}_C$, respectively. The tomographies are presented in Fig. 7.32.

According to simulations, the full-system state ρ_A is very close to being factorisable, with $F(\rho_A, \rho_A^{(e1,e2)} \otimes \rho_A^{(N1)} \otimes \rho_A^{(N2)}) = 0.984$, where $\rho_A^{(X)}$ is obtained by tracing out every subsystem except X. To obtain an estimate for the nuclear spin state after entanglement storage, we will set $\sigma_A := \hat{\rho}_A \otimes \rho_{N1} \otimes \rho_{N2}$, and minimize the error function

$$E = \left\| |S\sigma_A S^\dagger| - \hat{\rho}_B \right\|^2 + \left\| |S^2 \sigma_A S^{\dagger 2}| - \hat{\rho}_C \right\|^2 \tag{7.32}$$

over all possible nuclear states ρ_{N1} and ρ_{N2}. The S gate is the (imperfect) PSWAP gate obtained by simulating the PSWAP control sequence. The element-wise absolute value $|\cdot|$ is used because the upper limits in our tomographies contain no phase information.
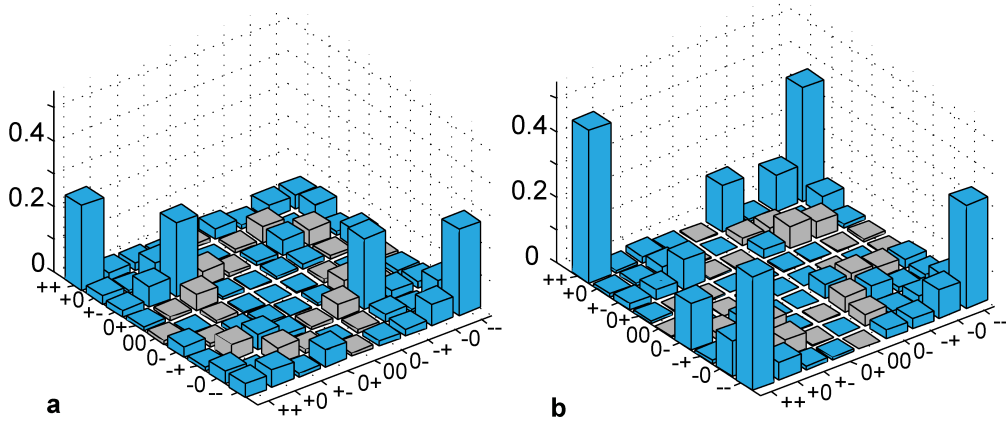
Figure 7.32.: Electron state tomography. Reconstructed electron spin density matrices. **a.** $\hat{\rho}_B$, after entanglement storage. **b.** $\hat{\rho}_C$, after entanglement retrieval.

7.7. Conclusion

Methods for improved sample fabrication were developed yielding an acceptable success rate ($\approx 2\%$). Here the implantation through nano channels in a thick mica sheet allows effectively for high energy implantation (1 MeV and higher) from a point source directly on diamond (Chapter 7.2.2). With recent progress in mask implantation techniques [132] as well in post processing (e.g. overgrowth of another diamond layer [133] and high temperature annealing [146]), low energy implantation techniques are on the verge of the capability of high yield quantum register production.

Deterministic on demand entanglement was demonstrated in a small quantum register, where two electron spins of two NV centers were entangled. To the knowledge of the author this is the first demonstration of entanglement of individual electron spins in a solid state matrix at ambient conditions. In order to exploit the best possible coherence times, a dynamical decoupling based entanglement sequence was developed. This sequence allows for entanglement of the NV centers on the order of milliseconds, potentially decreasing the necessary coupling for the strong coupling regime by two orders of magnitude.

In order to use the full register, the intrinsic nitrogen nuclear spin was used as a quantum memory storing the entangled state for milliseconds. With the usage of decoupling schemes this could be extended to the seconds range [19]. By storing the electron spin entanglement, a remote entangled state between the nuclear spin was created (the interaction strength between the nuclear spins (a few Hz) is significantly smaller as the time accessible to create the entangled state (35 μs))

fidelity for various control sequences	standard control	optimized control	calc. limit of current pair	calc. limit with optimum values*
NOT gate	0.94	0.99	> 0.99	> 0.999
entangling sequence	0.67 ± 0.04	0.824 ± 0.015	0.849	> 0.993
PSWAP gate	0.87	0.97 ± 0.01	0.97	> 0.999
^{15}N entanglement	0.42	0.819	0.823	> 0.993

Table 7.1.: Fidelity comparison. The upper limits are due to imperfect initialization and dephasing during the sequence. *Optimum values refer to the current record values for initialization fidelity (> 0.99), coherence lifetime ($T_2 = 4\,\mathrm{ms}$) and spin state eigenbasis.

Due to the dense control spectrum of the implemented quantum register (8 transitions, separated by 3 MHz respectively 30 MHz) the major limitation for high fidelity control is the limitations set by detuning as well as crosstalk. With the implementation of optimal control this key obstacle was overcome enabling full scalability of the high fidelity control.

The control methods, though tailored for NV centers, can easily be transferred to other types of experimental systems as well. Thus they are anticipated to find wide application. At the moment the performance is mainly limited by the coherence times of the electron spins. However, this is a material property and long coherence times for artificially created NV centers have been demonstrated in isotopically purified diamond [143]. Recent advances in implantation techniques (i.e. low energy mask implantations [132]) as well as coherence time extension by growing an additional layer of diamond over the implanted NVs [133] will pave the way for a high-yield chip size fabrication of NV arrays. The methods developed in this work will play a crucial role in making the control of such spin arrays feasible. The control fidelity could be further improved by robust control sequences which can automatically compensate for small magnetic field, temperature and control power fluctuations.

Since single shot read out of the electron spin is available at low temperature (4K) [29] and coherence times in isotropically pure samples have been reported to reach hundreds of milliseconds [174] , moving the experiments to a low temperature environment has the potential of a high fidelity quantum register with single shot read out [29].

The sample fabrication via mica mask implantation displayed in Chapter 7.2.2 were published in reference [58, 136]. While the entanglement generation and characterization shown in Chapter 7.3 and Chapter 7.4 as well as entanglement storage displayed in Chapter 7.5 were published in reference [58]. The improvements on control allowing for high fidelity controlled gates and decoherence limited entanglement generation described in Chapter 7.6 were published in reference [157].

A. Appendix

A.1. Measurement setup
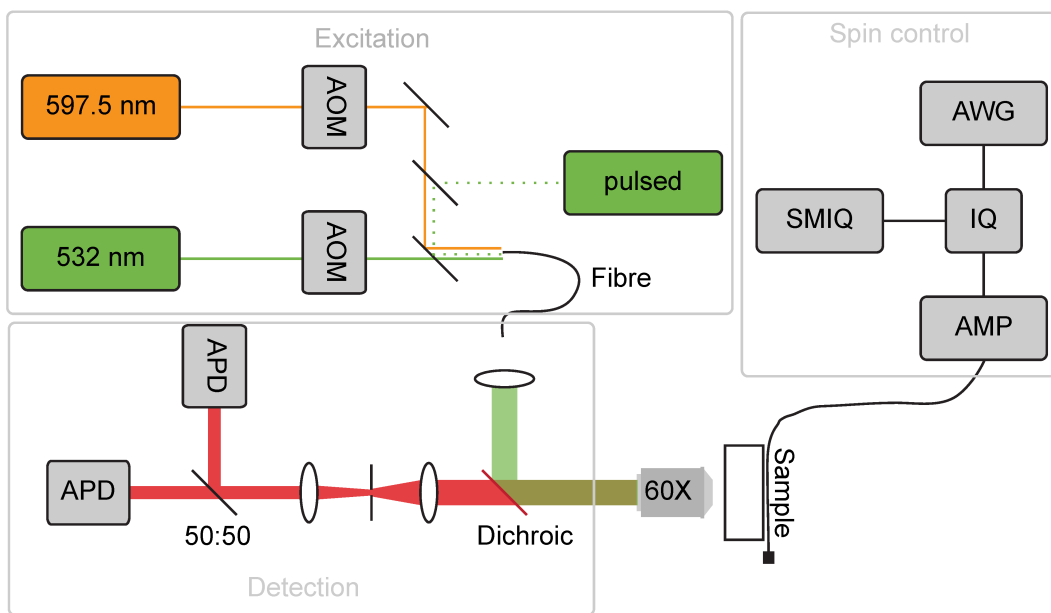
Figure A.1.: Schematic of the measurement setup.

A schematic of the measurement setup is shown in Fig. A.1. The setup can be decided in 3 parts: excitation, spin control and detection

Excitation

For most experiments, the NV is excited with a 532 nm green solid state laser with 200 mW. The laser signal can be controlled using an acousto-optical modulator (AOM) with a rise time of about 10-20 ns (depending on the focal width in the AOM). The light is then collected in a single mode polarization maintaining photonic crystal fiber to gain a Gaussian mode and to have the same excitation path for all lasers. The excitation light is coupled into the confocal microscope via a dichroic mirror, reflecting the shorter wavelength excitation light and transmitting the red fluorescence signal. Additional light sources (a 597.5 nm cw laser, a 532 pulsed laser

and a 638 nm cw laser) can be coupled into the same fiber with the use of either polarizing beam splitters or 50:50 beam splitters.

Detection

The signal detection consists of a home built confocal microscope, utilizing a spatially fixed high transmission microscope objective (Olympus UPLSAPO 60XO), while the sample is scanned using a piezo stage (Mad City Labs). The signal is detected through a 50 μm pinhole (100 mm achromatic lenses are used to focus the collimated light from the objective) with two avalanche photo-diodes (Exeltias SPCM) in a Hanbury-Brown and Twiss configuration. From a single NV center, a fluorescence ratio of $\approx 300\frac{\text{kcounts}}{\text{s}}$ could be detected.

Spin control

Spin control is realized using microwave radiation. As a microwave source a SMIQ 03B from Rhode&Schwarz is used. The microwave signal is either gated by a switch (mini circuits ZASWA-2-50DR+) or controlled by an IQ mixer (mini circuits ZX05-43+). An arbitrary wave form generator (Textronix AWG 5014C) was used in combination with the IQ mixer to realize arbitrary microwave phases, amplitudes and frequencies. The microwave signal was then amplified (mini circuits ZHL-16W-43-S+) and guides either into a wire or micro-structure on top of the diamond. Typical microwave frequencies in this work range from $2.75 - 3.00$ GHz with Rabi frequencies in the order of tens of MHz.

A.2. Micro structures

a. **b.**
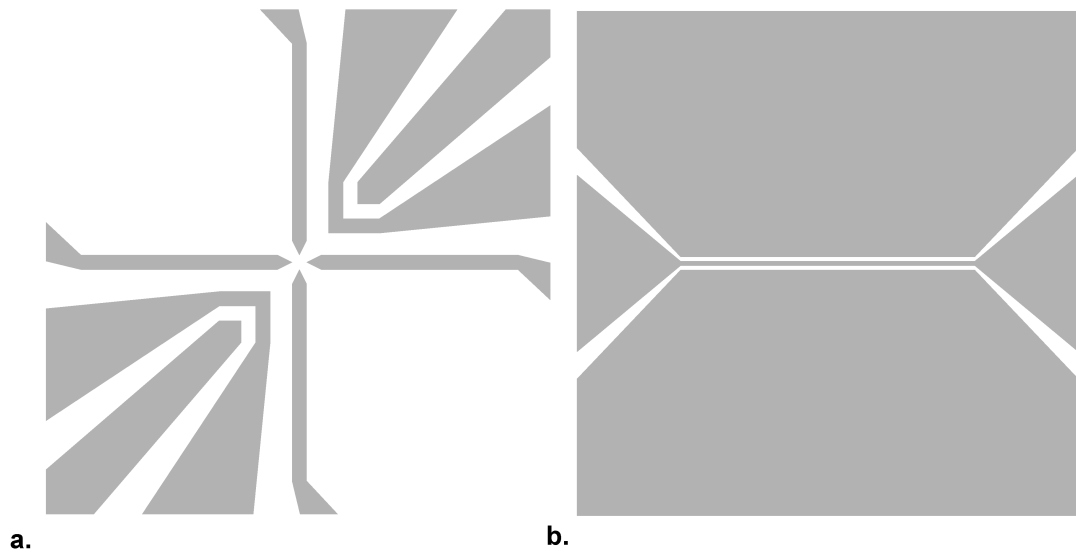
Figure A.2.: Micro-structure designs fabricated directly on the diamond substrate. a. With this structure electric fields can be applied between the four tips while microwaves are applied on the loop structures. The tips have a diameter of 10 μm and are seperated by 10 μm **b.** coplanar waveguide designed for high microwave fields at a NV center placed in the gap. The typical gap and waveguide thickness used was 50 μm, to allow for sufficient optical access.

A.3. Entanglement measure

To estimate the amount of entanglement in a given state ρ we use the entanglement measure by Plenio et al. introduced in reference [155], defined as

$$E(\rho) := \min_{\sigma \in \mathcal{D}} S(\rho \| \sigma), \tag{A.1}$$

where $\mathcal{D} \subset \mathcal{H}$ is the set of all separable states. The relative entropy $S(\rho \| \sigma)$ is given by

$$S(\rho \| \sigma) := \mathrm{Tr}\left(\rho(\log \rho - \log \sigma)\right). \tag{A.2}$$

Essentially $E(\rho)$ measures the relative-entropy "distance" of ρ from the set of separable states. (Strictly speaking, relative entropy is not a distance measure because it is not symmetric.) In practice it is estimated by starting with $\sigma_0 := \mathrm{diag}(\mathrm{diag}(\rho))$ and then generating a sequence of random separable states ζ_k, in each iteration setting $\sigma_k := (1 - s_k)\sigma_{k-1} + s_k \zeta_k$, where $s_k \in [0, 1]$ minimizes $S(\rho \| \sigma_k)$. This process yields a strict upper limit for $E(\rho)$.

For the ideal state $|\Phi_{\mathrm{dq}}\rangle = \frac{1}{\sqrt{2}}\left(|++\rangle + i\,|--\rangle\right)$ we may obtain analytically $E(|\Phi_{\mathrm{dq}}\rangle) = \ln 2$.

A.4. Magnetic field alignment

Two pairs of coil and one single coil were placed around the setup to allow precise control of the magnetic field. The magnetic field at the sample can be calibrated using a NV center as a magnetometer. As the symmetry axis has four possible alignments in a diamond crystal lattice, with the use of multiple NVs the magnetic fields can be determined precisely. The current through each coil assembly responsible for one magnetic field direction was swept and ODMR spectra recorded. With fitting of the spectra the current could be normalized to the applied magnetic field. This allowed the precise alignment and control of magnetic field strength and orientation in regard to the NV center.
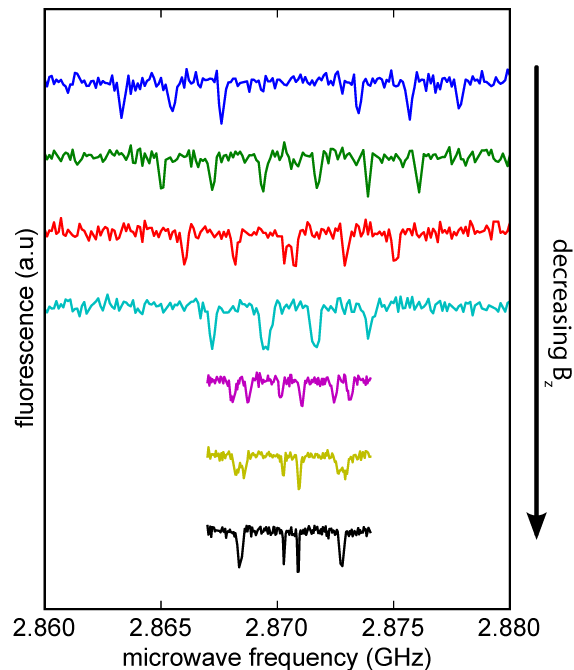
Figure A.3.: Low field alignment. ODMR spectra with decreasing B_z component of the applied B-field showing the hyperfine splitting due to the ^{14}N nucleus.

In order to have the necessary control precision for the electric field measurements (Chapter 6.4), high resolution ODMR spectra where utilized. Here the current through one coil was sweept and a hyperfine resolved ODMR spectrum recorded as shown in Fig. A.3. The occurrence of a strain splitting in the central lines ($m_I = 0$) was used to determine the absolute zero for B_z, while the outer peaks ($m_I = \pm 1$) were used to normalize the magnetic field to the applied current.

A.5. Microwave calibration
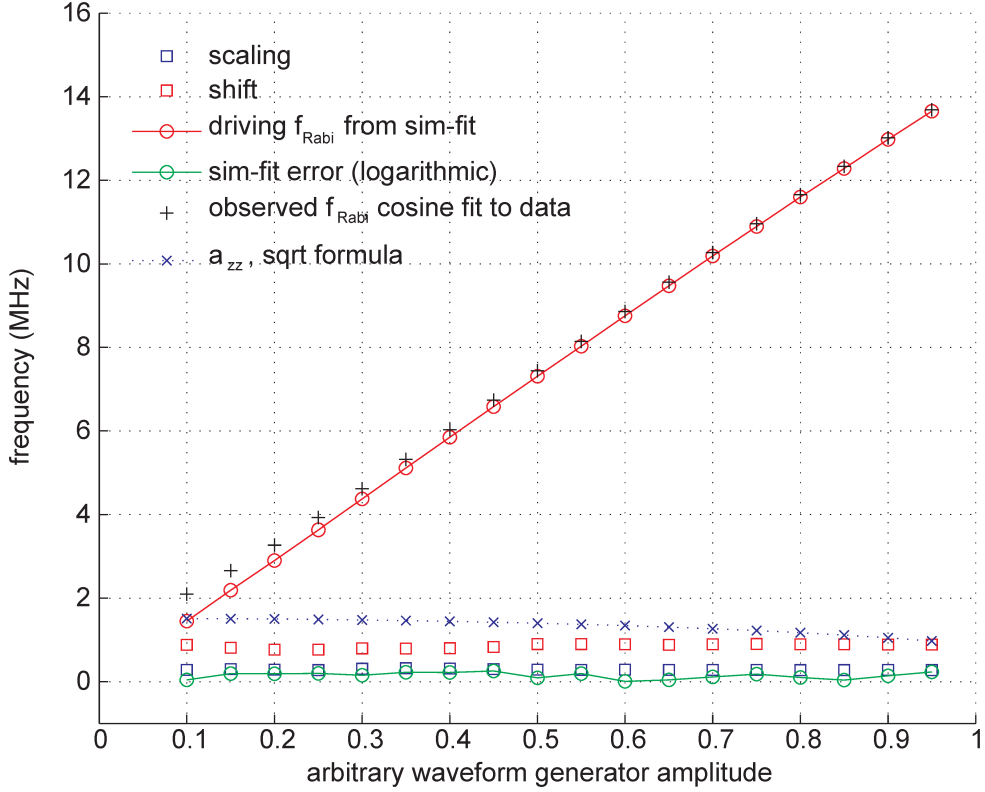
Figure A.4.: Microwave calibration. Here the result of the microwave calibration for one transition is shown. Slight nonlinearties in the amplifier response and the microwave transition properties are so compensated.

Once the Hamiltonian parameters are known (by fitting them to the measured hyperfine ODMR peaks such as the ones in Fig. 7.2) we determine the (in general nonlinear) dependence between the amplifier setting a and the corresponding driving Rabi frequency Ω_k for each carrier frequency $\tilde{\omega}_k$ separately (see Fig. A.4). This is done by finding, for a set of values of a, the Ω_k's that yield the best match between simulated and measured single driving data, and doing e.g. monotonous cubic spline interpolation between the points.

A.6. Charge state preselection

The NV center exists in at least two different charge states, NV^0 and NV^-. The ratio of these two states was measured to be 30:70 NV^0:NV^- [50, 65] for bulk diamond samples. ODMR and long spin coherence times have so far only be reported for NV^-. Therefore in this work, all experiments were carried out using NV^-. In order to distinguish between NV^0 and NV^-, their different excitation wavelengths can be exploited. The zero phonon line of the neutral charge state (575 nm) and the negative charge state (638 nm) are separated by approximately 60 nm, allowing us to address only the negative charge state with excitation light between 580 and 638 nm. However the main charge transfer mechanism is a two photon excitation process [64]. Therefore pumping with light between 580 nm and 638 nm will ultimately result in the neutral charge state NV^0, since the repumping rate is zero.

Figure A.5.: Charge state measurement. Histogram of detected counts under orange (597.5 nm) laser irradiation. The photon count time was 5 ms.

In order to investigate the charge state and ultimately selecting a charge state by a preselection measurement, only very low probing power can be used. In this work a probing power of $\approx 10\mu\text{W}$ at 597.5 nm was used. With a time binned measurement a photon count histogram was created (see Fig. A.5). A field programmable gate array (FPGA) counting device with a threshold dependent trigger was introduced to preselect only measurement sets where both NVs are negatively charged.

A.7. NV pair orientation
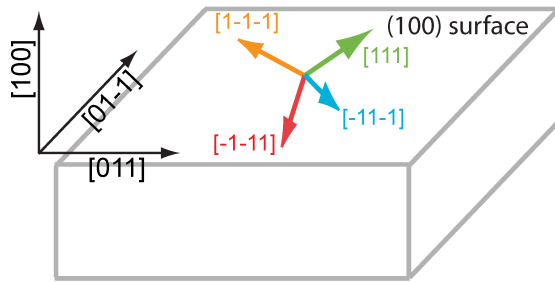
Figure A.6.: NV and crystal orientation. The possible NV orientation for a $[1\,0\,0]$ sample provided by element 6

There are 8 possible orientations of NV centers in diamond along the $\langle 1\,1\,1 \rangle$ axis [68]. In this work, electronic grade plates from Element 6 were used either as sample or as substrate for the ^{12}C enriched layer . The diamond surface was in $(1\,0\,0)$ direction and the edges where $\langle 1\,1\,0 \rangle$ [39].

Therefore the NV alignment can be determined simply by applying external magnetic fields. The alignment of the NV pair used in Chapter 6.5 and Chapter 7 was determined using knowledge of a $(1\,0\,0)$ surface and the $\langle 1\,1\,0 \rangle$ edges. With ODMR spectras and the knowledge of the applied field vectors the NV alignment were determined to be NV A/sensor $[1\,\bar{1}\,\bar{1}]$ and NV B/charge $[\bar{1}\,1\,\bar{1}]$. Please note that only the alignment can be determined by this method, the direction of the NV can only be derived by using additional known electric fields [68, 106].

A.8. Single and double quantum subspace

Since the NV center has a spin of S=1 there is threefold of eigenstates in the ground states can be denoted by the quantum numbers $m_S = 0, \pm 1$. If one limits oneself to two state coherences, there are three possibilities, two single quantum coherences ($|0\rangle \leftrightarrow |\pm\rangle$) and one double quantum coherence ($|+\rangle \leftrightarrow |-\rangle$). Since the direct transition for an aligned magnetic field is spin forbidden, composite pulses of the single quantum transitions $0 \leftrightarrow \pm 1$ have to be used to generate and control the double quantum subspace. E.g. a $|+\rangle + |-\rangle$ coherence can be generated from $|0\rangle$ by first applying a $\frac{\pi}{2}_+$ and then transporting the population in $|0\rangle$ to the $|-\rangle$ state by applying a π_- pulse.

Figure A.7.: Electron spin dipolar moments a, Spin vectors for NV 1 along $[\bar{1}1\bar{1}]$ direction. A magnetic field ($B = 4$ mT, the thick blue arrow) is aligned with the NV axis. Therefore, m_S is good quantum number. b, Spin vectors for NV 2 in the same field as in a. The spin vectors deviate from the NV axis (i.e. the $[\bar{1}1\bar{1}]$ direction) due to state mixing in a misaligned magnetic field. However, the tilt angle θ is small due to the weakness of the applied field. For $B = 4$mT, the spin magnitudes are +0.998, 0.0001, and -0.998 and $\theta = 1°$. Thus, the spin states are well-approximately denoted by $m_S = 0, \pm 1$.

The magnetic field interaction Hamiltonian is given by $H_B = \gamma_e \underline{S}\,\underline{B}$ and only the axial magnetic field contributes in first order. Therefore the magnetic field interaction can be approximated by $H_{B_z} = \gamma_e S_z B_z$. Since the $|+\rangle$ and the $|-\rangle$ states both shift their energy level under the application of a magnetic field B_z the phase collected by the coherent superposition state is doubled ($\nu_B = \delta m_s \cdot \gamma_e B_z \rightarrow \nu_{B\ SQ} = 1 \cdot \gamma_e B_z; \nu_{B\ DQ} = 2 \cdot \gamma_e B_z$). Since the main decoherence mechanism is magnetic field fluctuations, the enhancement in magnetic field sensitivity also leads to shorter coherence times. In most cases the double quantum (DQ) decoherence time is half of the single quantum (SQ) one ($T_{DQ} = T_{SQ}/2$). However it has been reported that for higher order dynamical decoupling the double quantum coherence times can exceed the single quantum ones.[175].

An additional feature of DQ coherences is the suppression of bath dynamics given by forbidden transitions [13]. Since the NV centers used in Chapter 6.5 and 7 were created by implantation of ^{15}N they are of spin I=1/2. Due to no quadrupolar interaction for I=1/2, there eigenstates are defined by the applied magnetic field. This leads to different nuclear spin eigenstate basis for $|0\rangle$ and $|\pm\rangle$, if the applied magnetic field is not along the NV axis. The dynamic of this coherent interaction

overshadows all electron spin coherent evolution.

The system of two NV centers is described by the Hamiltonian

$$H = H_A + H_B + H_{dip} \tag{A.3}$$

where H_A and H_B are the Hamiltonians of the two independent NV centers, NV A and NV B, respectively and H_{dip} describes the dipolar interaction between them. The two NV centers have different orientations. Their Hamiltonians (neglecting strain) are

$$H_A = \Delta \left(S_{zA}\right)^2 - \gamma_e B S_A + a_N S_A I_A \tag{A.4}$$

$$H_B = \Delta (S_{z'}^B)^2 - \gamma_e B S_B + a_N S_B I_B \tag{A.5}$$

where z $\|[111]$, z'$\|[1\bar{1}\bar{1}]$, and Δ=2.87 GHz is the zero field splitting of the NV center electron spin-1's (denoted by S_A and S_B). In the following the prime for the x,y,z directions of NV B are omitted (e.g. $S_{z'B} \to S_{zB}$). Each NV center contains a ^{15}N nuclear spin-1/2 (denoted by I_1 and I_2, respectively) with an isotropic hyperfine coupling constant a_N=3.05 MHz. The applied magnetic field B is aligned with NV 1. Thus the magnetic quantum number m_S^1 is a good quantum number. The Eigenstates of Hamiltonian (A.4) are denoted by $|\pm\rangle_1$ and $|0\rangle_1$. In this basis, the Hamiltonian is rewritten as

$$H_1 = \left(\omega_1^{(+)} + h_1^{(+)} I_1\right) |+\rangle_1 \langle+| + \left(\omega_1^{(-)} + h_1^{(-)} I_1\right) |-\rangle_1 \langle-| + \omega_1^{(0)} |0\rangle_1 \langle0| \tag{A.6}$$

where $h_1^{(\pm)} = \pm a_N \hat{z}$ is the effective hyperfine field seen by the ^{15}N nuclear spin conditioned on the electron spin $|\pm\rangle$ states. For the electron spin in the $|0\rangle$ state, the effective hyperfine field vanishes because $_1\langle0| S_1 |0\rangle_A = 0$. Please note that the electron nuclear spin flip-flop terms have been neglected in Eq. A.6, since the zero field splitting is much larger than the hyperfine coupling strength (i.e., $\Delta \gg a_N$).

Misalignment of the magnetic field to the symmetry axis of NV 2 causes state mixing. However, for the magnetic field strength (B$\approx$40 Gauss$\gg |\Delta/\gamma_e|$) applied in this experiments, the effect is small. We can still use the quantum number m_S^2 to (approximately) denote the eigenstates of Hamiltonian (A.5) (i.e. $|\pm\rangle_2$ and $|0\rangle_2$). Details of the state mixing effect are presented in Fig. A.7. Similar to Eq. A.6 with the electron nuclear spin flipflop terms and the offaxial magnetic field neglected, Hamiltonian (A.5) is written as

$$H_2 = \left(\omega_2^{(+)} + h_2^{(+)} I_2\right) |+\rangle_2 \langle+| + \left(\omega_2^{(-)} + h_2^{(-)} I_2\right) |-\rangle_2 \langle-| + \left(\omega_2^{(0)} + h_2^{(0)} I_2\right) |0\rangle_2 \langle0| \tag{A.7}$$

Note that electron spin state m_S^2=0 now has a small magnetic moment and thus

a hyperfine interaction $h_2^{(0)}$. Since the nuclear spin Zeeman interaction and the hyperfine interaction for $|\pm\rangle$ are not parallel for an nonaxial magnetic field, electron spin dependent eigenframes for the ^{15}N nuclear spin leads to a electron spin dependent rotation of the nuclear spin (see Chapter 7.5.1). Like for the ^{13}C spin bath [13], this leads to a complicated behavior of the NV coherences as shown in Fig. A.8.
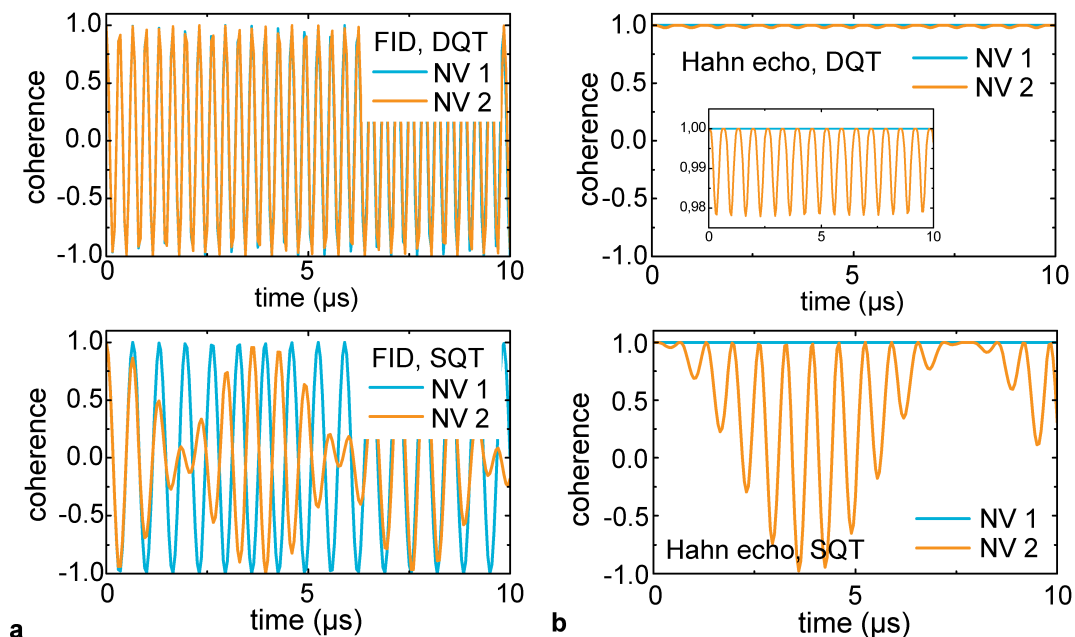
Figure A.8.: Effect of the nuclear spin dynamic a, FID modulation due to ^{15}N nuclear spin. Upper panel shows the ^{15}N induced modulation of double quantum transition (DQT), FID for aligned (NV 1) and misaligned (NV 2) NV centers. The two NV centers have a similar modulation effect. The lower panel shows the same modulation but for single quantum transition for the two NV centers. **b,** Hahn echo modulation due to ^{15}N nuclear spin. Upper panel shows the ^{15}N induced modulation of double quantum transition (DQT) Hahn echo signal for aligned (NV 1) and misaligned (NV 2) NV centers. The aligned NV center does not have modulations, and the misaligned NV center has a modulation with negligible amplitude. Lower panel shows the same modulation effect but for single quantum transition for the two NV centers.

Therefore it is preferable to work in the DQ subspace, since there are no additional nuclear spin dynamics complicating the measurement schemes.

A.9. Schemes to measure T_1, T_2^* and T_2 times
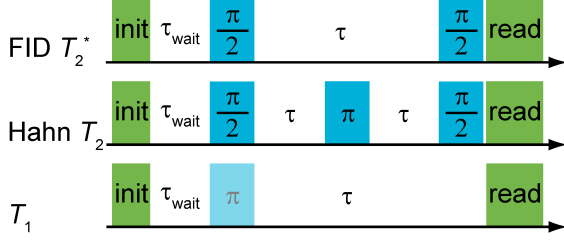
Figure A.9.: Measurement schemes Here different measurement schemes to measure the coherence properties are shown. The upper scheme is used to measure the inhomogeniuos line width T_2^*. The middle measurement is to determine the phase memory or pure dephasing time T_2. While the lower measurement is designed to detect the spin realxation time T_1. The faded π pulse is optional to investiage if there is a difference in relaxation rates for $|0\rangle$ or $|\pm\rangle$, e.g. due to laser polarization.

In order to measure the relevant life times of the NV center, the measurements sketched in Fig. A.9 were employed. In general the initialization and read out laser pulse had a length of $3\,\mu$s followed by a $\tau_{\mathrm{wait}} = 1.5\,\mu$s waiting time. Normally the read out pulse was used as the polarization pulse for the next measurement.

For the coherence measurement, the last $\frac{\pi}{2}$ pulse can be alternated with a $\frac{3\pi}{2}$ pulse, allowing to fit the difference between both measurements without an offset. For double quantum measurements, the $\frac{\pi}{2}$ pulse used to create the coherence is replaced by $\frac{\pi}{2}_+ - \pi_-$ or $\pi_- - \frac{\pi}{2}_+$ to map the coherence in a population difference.

The measurement of the spin relaxation time T_1 can also be conducted with and without a π pulse, allowing the investigation of spin state dependent decay rates. This, e.g. allows to determine if re-polarization due to leakage of the excitation laser is the main source for spin relaxation.

B. Bibliography

[1] Degen C. Microscopy with single spins. *Nature nanotechnology.* 2008;3:643.

[2] Shor PW. Polynomial-Time Algorithms for Prime Factorization and Discrete Logarithms on a Quantum Computer. *arXiv:quant-ph/9508027v2.* 1996;.

[3] Grover LK. A fast quantum mechanical algorithm for database search. In: *Proceedings of the twenty-eighth annual ACM symposium on Theory of computing.* 1996; p. 212–219.

[4] Ritter S, Nölleke C, Hahn C, Reiserer A, Neuzner A, Uphoff M, Mücke M, Figueroa E, Bochmann J, Rempe G. An elementary quantum network of single atoms in optical cavities. *Nature.* 2012;484(7393):195–200.

[5] Blatt R, Wineland D. Entangled states of trapped atomic ions. *Nature.* 2008; 453(7198):1008–1015.

[6] Simmons S, Brown RM, Riemann H, Abrosimov NV, Becker P, Pohl HJ, Thewalt ML, Itoh KM, Morton JJ. Entanglement in a solid-state spin ensemble. *Nature.* 2011;470(7332):69–72.

[7] Shulman MD, Dial OE, Harvey SP, Bluhm H, Umansky V, Yacoby A. Demonstration of entanglement of electrostatically coupled singlet-triplet qubits. *Science.* 2012;336(6078):202–205.

[8] Neeley M, Bialczak RC, Lenander M, Lucero E, Mariantoni M, OConnell A, Sank D, Wang H, Weides M, Wenner J, et al. Generation of three-qubit entangled states using superconducting phase qubits. *Nature.* 2010; 467(7315):570–573.

[9] DiCarlo L, Reed M, Sun L, Johnson B, Chow J, Gambetta J, Frunzio L, Girvin S, Devoret M, Schoelkopf R. Preparation and measurement of three-qubit entanglement in a superconducting circuit. *Nature.* 2010;467(7315):574–578.

[10] Lee K, Sprague M, Sussman B, Nunn J, Langford N, Jin XM, Champion T, Michelberger P, Reim K, England D, et al. Entangling macroscopic diamonds at room temperature. *Science.* 2011;334(6060):1253–1256.

[11] Ladd TD, Jelezko F, Laflamme R, Nakamura Y, Monroe C, OBrien JL. Quantum computers. *Nature.* 2010;464(7285):45–53.

[12] Gruber A, Drabenstedt A, Tietz C, Fleury L, Wrachtrup J, vonBorczyskowski C. Scanning confocal optical microscopy and magnetic resonance on single defect centers. *Science.* 1997;276(5321):2012–2014.

[13] Childress L, Gurudev Dutt MV, Taylor JM, Zibrov AS, Jelezko F, Wrachtrup J, Hemmer PR, Lukin MD. Coherent Dynamics of Coupled Electron and Nuclear Spin Qubits in Diamond. *Science.* 2006;314(5797):281–285.

[14] Tisler J, Balasubramanian G, Naydenov B, Kolesov R, Grotz B, Reuter R, Boudou JP, Curmi PA, Sennour M, Thorel A, Bòˆrsch M, Aulenbacher K, Erdmann R, Hemmer PR, Jelezko F, Wrachtrup J. Fluorescence and

Spin Properties of Defects in Single Digit Nanodiamonds. *ACS Nano*. 2009; 3(7):1959–1965.

[15] Balasubramanian G, Neumann P, Twitchen D, Markham M, Kolesov R, Mizuochi N, Isoya J, Achard J, Beck J, Tissler J, Jacques V, Hemmer PR, Jelezko F, Wrachtrup J. Ultralong spin coherence time in isotopically engineered diamond. *Nature Materials*. 2009;8(5):383–387.

[16] Carr HY, Purcell EM. Effects of Diffusion on Free Precession in Nuclear Magnetic Resonance Experiments. *Phys Rev*. 1954;94(3):630–638.

[17] Meiboom S, Gill D. Modified Spin-Echo Method for Measuring Nuclear Relaxation Times. *Review of Scientific Instruments*. 1958;29(8):688–691.

[18] Waldherr G, Wang Y, Zaiser S, Jamali M, Schulte-Herbrüggen T, Abe H, Ohshima T, Isoya J, Du J, Neumann P, et al. Quantum error correction in a solid-state hybrid spin register. *Nature*. 2014;.

[19] Maurer PC, Kucsko G, Latta C, Jiang L, Yao NY, Bennett SD, Pastawski F, Hunger D, Chisholm N, Markham M, Twitchen DJ, Cirac JI, Lukin MD. Room-Temperature Quantum Bit Memory Exceeding One Second. *Science*. 2012;336(6086):1283–1286.

[20] Maze JR, Stanwix PL, Hodges JS, Hong S, Taylor JM, Cappellaro P, Jiang L, Dutt MVG, Togan E, Zibrov AS, Yacoby A, Walsworth RL, Lukin MD. Nanoscale magnetic sensing with an individual electronic spin in diamond. *Nature*. 2008;455(7213):644–647.

[21] van Oort E, Glasbeek M. Electric-Field-Induced Modulation of Spin Echoes of N-V Centers in Diamond. *Chemical Physics Letters*. 1990;168(6):529–532.

[22] Acosta VM, Bauch E, Ledbetter MP, Waxman A, Bouchard LS, Budker D. Temperature Dependence of the Nitrogen-Vacancy Magnetic Resonance in Diamond. *Physical Review Letters*. 2010;104(7):070801.

[23] Taylor JM, Cappellaro P, Childress L, Jiang L, Budker D, Hemmer PR, Yacoby A, Walsworth R, Lukin MD. High-sensitivity diamond magnetometer with nanoscale resolution. *Nature Physics*. 2008;4(10):810–816.

[24] Jelezko F, Gaebel T, Popa I, Gruber A, Wrachtrup J. Observation of coherent oscillations in a single electron spin. *Physical Review Letters*. 2004; 92(7):076401.

[25] DiVincenzo DP, et al. The physical implementation of quantum computation. *arXiv preprint quant-ph/0002077*. 2000;.

[26] Fuchs GD, Dobrovitski VV, Toyli DM, Heremans FJ, Awschalom DD. Gigahertz Dynamics of a Strongly Driven Single Quantum Spin. *Science*. 2009;326(5959):1520–1522.

[27] Jelezko F, Gaebel T, Popa I, Domhan M, Gruber A, Wrachtrup J. Observation of coherent oscillation of a single nuclear spin and realization of a two-qubit conditional quantum gate. *Physical Review Letters*. 2004;93(13):130501.

[28] Neumann P, Beck J, Steiner M, Rempp F, Fedder H, Hemmer PR, Wrachtrup J, Jelezko F. Single-Shot Readout of a Single Nuclear Spin. *Science*. 2010; 329(5991):542–544.

[29] Robledo L, Childress L, Bernien H, Hensen B, Alkemade PF, Hanson R. High-fidelity projective read-out of a solid-state spin quantum register. *Nature*.

2011;477(7366):574–578.

[30] Neumann P, Mizuochi N, Rempp F, Hemmer P, Watanabe H, Yamasaki S, Jacques V, Gaebel T, Jelezko F, Wrachtrup J. Multipartite Entanglement Among Single Spins in Diamond. *Science*. 2008;320(5881):1326–1329.

[31] Dutt MVG, Childress L, Jiang L, Togan E, Maze J, Jelezko F, Zibrov AS, Hemmer PR, Lukin MD. Quantum register based on individual electronic and nuclear spin qubits in diamond. *Science*. 2007;316(5829):1312–1316.

[32] Shi F, Rong X, Xu N, Wang Y, Wu J, Chong B, Peng X, Kniepert J, Schoenfeld RS, Harneit W, Feng M, Du J. Room-Temperature Implementation of the Deutsch-Jozsa Algorithm with a Single Electronic Spin in Diamond. *Physical Review Letters*. 2010;105(4):040504.

[33] Yao NY, Jiang L, Gorshkov AV, Maurer PC, Giedke G, Cirac JI, Lukin MD. Scalable architecture for a room temperature solid-state quantum information processor. *Nat Commun*. 2012;3:800.

[34] Rabl P, Kolkowitz SJ, Koppens FHL, Harris JGE, Zoller P, Lukin MD. A quantum spin transducer based on nanoelectromechanical resonator arrays. *Nature Physics*. 2010;6(8):602–608.

[35] Bernien H, Hensen B, Pfaff W, Koolstra G, Blok MS, Robledo L, Taminiau TH, Markham M, Twitchen DJ, Childress L, Hanson R. Heralded entanglement between solid-state qubits separated by three metres. *Nature*. 2013; 497(7447):86–90.

[36] Khaneja N, Reiss T, Kehlet C, Schulte-Herbrggen T, Glaser SJ. Optimal control of coupled spin dynamics: design of {NMR} pulse sequences by gradient ascent algorithms. *J Magn Reson*. 2005;172:296–305.

[37] Cappellaro P, Emerson J, Boulant N, Ramanathan C, Lloyd S, Cory DG. Entanglement assisted metrology. *Physical review letters*. 2005;94(2):020502.

[38] Cappellaro P, Lukin M. Quantum correlation in disordered spin systems: Applications to magnetic sensing. *Physical Review A*. 2009;80(3):032311.

[39] Element 6 webpage. `http://www.e6cvd.com/cvd/page.jsp?pageid=415`. 2014.

[40] Harris CB, Schlupp RL, Schuch H. Optically Detected Electron Spin Locking and Rotary Echo Trains in Molecular Excited States. *Phys Rev Lett*. 1973; 30(21):1019–1022.

[41] Tamarat P, Gaebel T, Rabeau J, Khan M, Greentree A, Wilson H, Hollenberg L, Prawer S, Hemmer P, Jelezko F, Wrachtrup J. Stark Shift Control of Single Optical Centers in Diamond. *Physical Review Letters*. 2006;97(8):083002.

[42] Dolde F, Doherty MW, Michl J, Jakobi I, Naydenov B, Pezzagna S, Meijer J, Neumann P, Jelezko F, Manson NB, et al. Nanoscale Detection of a Single Fundamental Charge in Ambient Conditions Using the NV- Center in Diamond. *Phys Rev Lett*. 2014;112:097603.

[43] Meijer J, Burchard B, Domhan M, Wittmann C, Gaebel T, Popa I, Jelezko F, Wrachtrup J. Generation of single color centers by focused nitrogen implantation. *Applied Physics Letters*. 2005;87(26):261909 –261909–3.

[44] Staudacher T, Shi F, Pezzagna S, Meijer J, Du J, Meriles CA, Reinhard F, Wrachtrup J. Nuclear Magnetic Resonance Spectroscopy on a (5-Nanometer)3

Sample Volume. *Science*. 2013;339(6119):561–563.

[45] Grinolds MS, Hong S, Maletinsky P, Luan L, Lukin MD, Walsworth RL, Yacoby A. Nanoscale magnetic imaging of a single electron spin under ambient conditions. *Nature Physics*. 2013;9(4):215–219.

[46] Naydenov B. Detection of a few silicon nuclear spins outside of diamond. 2014. Private communication.

[47] Yu SJ, Kang MW, Chang HC, Chen KM, Yu YC. Bright fluorescent nanodiamonds: no photobleaching and low cytotoxicity. *Journal of the American Chemical Society*. 2005;127(50):17604–17605.

[48] McGuinness LP, Yan Y, Stacey A, Simpson DA, Hall LT, Maclaurin D, Prawer S, Mulvaney P, Wrachtrup J, Caruso F, Scholten RE, Hollenberg LCL. Quantum measurement and orientation tracking of fluorescent nanodiamonds inside living cells. *Nature Nanotechnology*. 2011;6(6):358–363.

[49] Kucsko G, Maurer PC, Yao NY, Kubo M, Noh HJ, Lo PK, Park H, Lukin MD. Nanometre-scale thermometry in a living cell. *Nature*. 2013;500:54–58.

[50] Waldherr G, Beck J, Steiner M, Neumann P, Gali A, Frauenheim T, Jelezko F, Wrachtrup J. Dark States of Single Nitrogen-Vacancy Centers in Diamond Unraveled by Single Shot NMR. *Physical Review Letters*. 2011;106(15):157601.

[51] Doherty MW, Manson NB, Delaney P, Jelezko F, Wrachtrup J, Hollenberg LC. The nitrogen-vacancy colour centre in diamond. *Physics Reports*. 2013; 528(1):1–45.

[52] Felton S, Edmonds AM, Newton ME, Martineau PM, Fisher D, Twitchen DJ, Baker JM. Hyperfine interaction in the ground state of the negatively charged nitrogen vacancy center in diamond. *Phys Rev B*. 2009;79:075203.

[53] Larsson J, Delaney P. Electronic structure of the nitrogen-vacancy center in diamond from first-principles theory. *Physical Review B*. 2008;77(16):165201.

[54] Gali A, Fyta M, Kaxiras E. Ab initio supercell calculations on nitrogen-vacancy center in diamond: Electronic structure and hyperfine tensors. *Physical Review B*. 2008;77(15):155206.

[55] Neumann P, Kolesov R, Jacques V, Beck J, Tisler J, Batalov A, Rogers L, Manson NB, Balasubramanian G, Jelezko F, Wrachtrup J. Excited-state spectroscopy of single NV defects in diamond using optically detected magnetic resonance. *New Journal of Physics*. 2009;11:013017.

[56] Rogers L, Armstrong S, Sellars M, Manson N. Infrared emission of the NV centre in diamond: Zeeman and uniaxial stress studies. *New Journal of Physics*. 2008;10(10):103024.

[57] Doherty MW, Dolde F, Fedder H, Jelezko F, Wrachtrup J, Manson NB, Hollenberg LCL. Theory of the ground-state spin of the NVˆ{-} center in diamond. *Physical Review B*. 2012;85(20):205203.

[58] Dolde F, Jakobi I, Naydenov B, Zhao N, Pezzagna S, Trautmann C, Meijer J, Neumann P, Jelezko F, Wrachtrup J. Room-temperature entanglement between single defect spins in diamond. *Nature Physics*. 2013;9(3):139–143.

[59] Rabeau JR, Reichart P, Tamanyan G, Jamieson DN, Prawer S, Jelezko F, Gaebel T, Popa I, Domhan M, Wrachtrup J. Implantation of labelled single nitrogen vacancy centers in diamond using N-15. *Applied Physics Letters*.

2006;88(2):023113.

[60] Hodges JS, Yang JC, Ramanathan C, Cory DG. Universal control of nuclear spins via anisotropic hyperfine interactions. *Physical Review A*. 2008; 78(1):010303.

[61] Naydenov B, Dolde F, Hall LT, Shin C, Fedder H, Hollenberg LCL, Jelezko F, Wrachtrup J. Dynamical decoupling of a single-electron spin at room temperature. *Phys Rev B*. 2011;83:081201.

[62] De Lange G, Wang Z, Riste D, Dobrovitski V, Hanson R. Universal dynamical decoupling of a single solid-state spin from a spin bath. *Science*. 2010; 330(6000):60–63.

[63] Steiner M, Neumann P, Beck J, Jelezko F, Wrachtrup J. Universal enhancement of the optical readout fidelity of single electron spins at nitrogen-vacancy centers in diamond. *Physical Review B*. 2010;81(3):035205.

[64] Aslam N, Waldherr G, Neumann P, Jelezko F, Wrachtrup J. Photo-induced ionization dynamics of the nitrogen vacancy defect in diamond investigated by single-shot charge state detection. *New Journal of Physics*. 2013;15(1):013064.

[65] Waldherr G, Neumann P, Huelga SF, Jelezko F, Wrachtrup J. Violation of a Temporal Bell Inequality for Single Spins in a Diamond Defect Center. *Physical Review Letters*. 2011;107(9):090401.

[66] Neumann P. Towards a room temperature solid state quantum processor - the Nitrogen-Vacancy-Center in diamond. Ph.D. thesis, 3. Physikailsche Institut, Universitt Stuttgart. 2012.

[67] Slichter C. *Principles of magnetic resonance*. Springer Verlag. 1989.

[68] Michl J, Teraji T, Zaiser S, Jakobi I, Waldherr G, Dolde F, Neumann P, Doherty MW, Manson NB, Isoya J, et al. Perfect alignment and preferential orientation of nitrogen-vacancy centers during chemical vapor deposition diamond growth on (111) surfaces. *Applied Physics Letters*. 2014; 104(10):102407.

[69] Maze J, Taylor J, Lukin M. Electron spin decoherence of single nitrogen-vacancy defects in diamond. *Physical Review B*. 2008;78(9).

[70] Hahn EL. Spin echoes. *Physical review*. 1950;80(4):580.

[71] Mizuochi N, Neumann P, Rempp F, Beck J, Jacques V, Siyushev P, Nakamura K, Twitchen D, Watanabe H, Yamasaki S, et al. Coherence of single spins coupled to a nuclear spin bath of varying density. *Physical review B*. 2009; 80(4):041201.

[72] Wang ZH, Zhang W, Tyryshkin A, Lyon S, Ager J, Haller E, Dobrovitski V. Effect of pulse error accumulation on dynamical decoupling of the electron spins of phosphorus donors in silicon. *Physical Review B*. 2012;85(8):085206.

[73] Mizuochi N, Neumann P, Rempp F, Beck J, Jacques V, Siyushev P, Nakamura K, Twitchen DJ, Watanabe H, Yamasaki S, Jelezko F, Wrachtrup J. Coherence of single spins coupled to a nuclear spin bath of varying density. *PHYSICAL REVIEW B*. 2009;80.

[74] Zhao N, Hu JL, Ho SW, Wan JT, Liu R. Atomic-scale magnetometry of distant nuclear spin clusters via nitrogen-vacancy spin in diamond. *Nature nanotechnology*. 2011;6(4):242–246.

[75] Zhao N, Honert J, Schmid B, Klas M, Isoya J, Markham M, Twitchen D, Jelezko F, Liu RB, Fedder H, et al. Sensing single remote nuclear spins. *Nature nanotechnology*. 2012;7(10):657–662.

[76] Maze JR, Taylor JM, Lukin MD. Electron spin decoherence of single nitrogen-vacancy defects in diamond. *Phys Rev B*. 2008;78:094303.

[77] Jacques V, Neumann P, Beck J, Markham M, Twitchen D, Meijer J, Kaiser F, Balasubramanian G, Jelezko F, Wrachtrup J. Dynamic Polarization of Single Nuclear Spins by Optical Pumping of Nitrogen-Vacancy Color Centers in Diamond at Room Temperature. *Physical Review Letters*. 2009;102(5):057403.

[78] Balasubramanian G, Neumann P, Twitchen D, Markham M, Kolesov R, Mizuochi N, Isoya J, Achard J, Beck J, Tissler J, Jacques V, Hemmer PR, Jelezko F, Wrachtrup J. Ultralong spin coherence time in isotopically engineered diamond. *Nature materials*. 2009;8:383–387.

[79] Balasubramanian G, I Y Chan RK, Al-Hmoud M, Tisler J, Shin C, Kim C, Wojcik A, Hemmer PR, Krueger A, Hanke T, Leitenstorfer A, Bratschitsch R, Jelezko F, Wrachtrup J. Nanoscale imaging magnetometry with diamond spins under ambient conditions. *Nature*. 2008;455:648–651.

[80] Rondin L, Tetienne JP, Rohart S, Thiaville A, Hingant T, Spinicelli P, Roch JF, Jacques V. Stray-field imaging of magnetic vortices with a single diamond spin. *Nature communications*. 2013;4.

[81] Maletinsky P, Hong S, Grinolds MS, Hausmann B, Lukin MD, Walsworth RL, Loncar M, Yacoby A. A robust scanning diamond sensor for nanoscale imaging with single nitrogen-vacancy centres. *Nature Nanotechnology*. 2012; 7(5):320–324.

[82] Häberle T, Schmid-Lorch D, Karrai K, Reinhard F, Wrachtrup J. High-dynamic-range imaging of nanoscale magnetic fields using optimal control of a single qubit. *Physical review letters*. 2013;111(17):170801.

[83] Acosta VM, Bauch E, Jarmola A, Zipp LJ, Ledbetter MP, Budker D. Broadband magnetometry by infrared-absorption detection of nitrogen-vacancy ensembles in diamond. *arXiv:10094747v2*. 2010;.

[84] Steinert S, Dolde F, Neumann P, Aird A, Naydenov B, Balasubramanian G, Jelezko F, Wrachtrup J. High sensitivity magnetic imaging using an array of spins in diamond. *Review of Scientific Instruments*. 2010;81(4).

[85] Steinert S, Ziem F, Hall LT, Zappe A, Schweikert M, Götz N, Aird A, Balasubramanian G, Hollenberg L, Wrachtrup J. Magnetic spin imaging under ambient conditions with sub-cellular resolution. *Nature Communications*. 2013;4:1607.

[86] Waldherr G, Beck J, Neumann P, Said RS, Nitsche M, Markham ML, Twitchen DJ, Twamley J, Jelezko F, Wrachtrup J. High-dynamic-range magnetometry with a single nuclear spin in diamond. *Nature Nanotechnology*. 2011;7(2):105–108.

[87] Schoenfeld RS, Harneit W. Real time magnetic field sensing and imaging using a single spin in diamond. *Physical review letters*. 2011;106(3):030802.

[88] Kotler S, Akerman N, Glickman Y, Keselman A, Ozeri R. Single-ion quantum lock-in amplifier. *Nature*. 2011;473(7345):61–65.

[89] Mamin HJ, Kim M, Sherwood MH, Rettner CT, Ohno K, Awschalom DD, Rugar D. Nanoscale Nuclear Magnetic Resonance with a Nitrogen-Vacancy Spin Sensor. *Science*. 2013;339(6119):557–560.

[90] Marseglia L, Hadden JP, Stanley-Clarke AC, Harrison JP, Patton B, Ho YLD, Naydenov B, Jelezko F, Meijer J, Dolan PR, Smith JM, Rarity JG, O'Brien JL. Nanofabricated solid immersion lenses registered to single emitters in diamond. *Applied Physics Letters*. 2011;98(13):133107–133107–3.

[91] Mamin H, Sherwood M, Kim M, Rettner C, Ohno K, Awschalom D, Rugar D. Multipulse Double-Quantum Magnetometry With Near-Surface Nitrogen Vacancy Centers. *arXiv preprint arXiv:14047480*. 2014;.

[92] Goldstein G, Cappellaro P, Maze J, Hodges J, Jiang L, Sørensen AS, Lukin M. Environment-assisted precision measurement. *Physical review letters*. 2011; 106(14):140502.

[93] Dréau A, Lesik M, Rondin L, Spinicelli P, Arcizet O, Roch JF, Jacques V. Avoiding power broadening in optically detected magnetic resonance of single NV defects for enhanced dc magnetic field sensitivity. *Physical Review B*. 2011;84(19):195204.

[94] Yoo M, Fulton T, Hess H, Willett R, Dunkleberger L, Chichester R, Pfeiffer L, West K. Scanning single-electron transistor microscopy: Imaging individual charges. *Science*. 1997;276(5312):579–582.

[95] Martin J, Akerman N, Ulbricht G, Lohmann T, Smet J, Von Klitzing K, Yacoby A. Observation of electron–hole puddles in graphene using a scanning single-electron transistor. *Nature Physics*. 2008;4(2):144–148.

[96] Devoret MH, Schoelkopf RJ. Amplifying quantum signals with the single-electron transistor. *Nature*. 2000;406(6799):1039–1046.

[97] Schönenberger C, Alvarado S. Observation of single charge carriers by force microscopy. *Physical review letters*. 1990;65(25):3162–3164.

[98] Henning AK, Hochwitz T, Slinkman J, Never J, Hoffmann S, Kaszuba P, Daghlian C. Two-dimensional surface dopant profiling in silicon using scanning Kelvin probe microscopy. *Journal of applied physics*. 1995;77(5):1888–1896.

[99] Cleland AN, Roukes ML. A nanometre-scale mechanical electrometer. *Nature*. 1998;392(6672):160–162.

[100] Schönenberger C. Charge flow during metal-insulator contact. *Physical Review B*. 1992;45(7):3861.

[101] Balasubramanian G, Chan IY, Kolesov R, Al-Hmoud M, Tisler J, Shin C, Kim C, Wojcik A, Hemmer PR, Krueger A, Hanke T, Leitenstorfer A, Bratschitsch R, Jelezko F, Wrachtrup J. Nanoscale imaging magnetometry with diamond spins under ambient conditions. *Nature*. 2008;455(7213):648–651.

[102] Toyli DM, Casas CFdl, Christle DJ, Dobrovitski VV, Awschalom DD. Fluorescence thermometry enhanced by the quantum coherence of single spins in diamond. *Proceedings of the National Academy of Sciences*. 2013; 110(21):8417–8421. PMID: 23650364.

[103] Neumann P, Jakobi I, Dolde F, Burk C, Reuter R, Waldherr G, Honert J, Wolf T, Brunner A, Shim JH, Suter D, Sumiya H, Isoya J, Wrachtrup J. High-Precision Nanoscale Temperature Sensing Using Single Defects in

Diamond. *Nano Letters.* 2013;.

[104] Mims WB. *The linear Stark effect in paramagnetic resonance.* Clarendon press. 1976.

[105] Doherty MW, Dolde F, Fedder H, Jelezko F, Wrachtrup J, Manson NB, Hollenberg LCL. Theory of the ground-state spin of the NV$^-$ center in diamond. *Phys Rev B.* 2012;85:205203.

[106] Doherty MW, Michl J, Dolde F, Jakobi I, Neumann P, Manson NB, Wrachtrup J. Measuring the defect structure orientation of a single NV-centre in diamond. *arXiv preprint arXiv:14024789.* 2014;.

[107] Elzerman J, Hanson R, Van Beveren LW, Witkamp B, Vandersypen L, Kouwenhoven LP. Single-shot read-out of an individual electron spin in a quantum dot. *Nature.* 2004;430(6998):431–435.

[108] Patolsky F, Zheng G, Lieber CM. Fabrication of silicon nanowire devices for ultrasensitive, label-free, real-time detection of biological and chemical species. *Nature Protocols.* 2006;1(4):1711–1724.

[109] Cui Y, Wei Q, Park H, Lieber CM. Nanowire nanosensors for highly sensitive and selective detection of biological and chemical species. *Science.* 2001; 293(5533):1289–1292.

[110] Williams C, Slinkman J, Hough W, Wickramasinghe H. Lateral dopant profiling with 200 nm resolution by scanning capacitance microscopy. *Applied Physics Letters.* 1989;55(16):1662–1664.

[111] Martin Y, Abraham DW, Wickramasinghe HK. High-resolution capacitance measurement and potentiometry by force microscopy. *Applied Physics Letters.* 1988;52(13):1103–1105.

[112] Bunch JS, Van Der Zande AM, Verbridge SS, Frank IW, Tanenbaum DM, Parpia JM, Craighead HG, McEuen PL. Electromechanical resonators from graphene sheets. *Science.* 2007;315(5811):490–493.

[113] Salfi J, Savelyev I, Blumin M, Nair S, Ruda H. Direct observation of single-charge-detection capability of nanowire field-effect transistors. *Nature nanotechnology.* 2010;5(10):737–741.

[114] Lee J, Zhu Y, Seshia A. Room temperature electrometry with SUB-10 electron charge resolution. *Journal of Micromechanics and Microengineering.* 2008; 18(2):025033.

[115] Han KY, Kim SK, Eggeling C, Hell SW. Metastable Dark States Enable Ground State Depletion Microscopy of Nitrogen Vacancy Centers in Diamond with Diffraction-Unlimited Resolution. *Nano Letters.* 2010;10(8):3199–3203.

[116] Chu Z, Zhang S, Zhang B, Zhang C, Fang CY, Rehor I, Cigler P, Chang HC, Lin G, Liu R, et al. Unambiguous observation of shape effects on cellular fate of nanoparticles. *Scientific reports.* 2014;4.

[117] Zurbuchen MA, Lake MP, Kohan SA, Leung B, Bouchard LS. Nanodiamond Landmarks for Subcellular Multimodal Optical and Electron Imaging. *Scientific reports.* 2013;3.

[118] Hall LT, Hill CD, Cole JH, Städler B, Caruso F, Mulvaney P, Wrachtrup J, Hollenberg LC. Monitoring ion-channel function in real time through quantum decoherence. *Proceedings of the National Academy of Sciences.* 2010;

107(44):18777–18782.

[119] Einstein A, Podolsky B, Rosen N. Can Quantum-Mechanical Description of Physical Reality Be Considered Complete? *Physical Review*. 1935; 47(10):777–780.

[120] Lanyon BP, Whitfield JD, Gillett G, Goggin ME, Almeida MP, Kassal I, Biamonte JD, Mohseni M, Powell BJ, Barbieri M, et al. Towards quantum chemistry on a quantum computer. *Nature Chemistry*. 2010;2(2):106–111.

[121] Aspect A, Grangier P, Roger G. Experimental Tests of Realistic Local Theories via Bell's Theorem. *Physical Review Letters*. 1981;47(7):460–463.

[122] Bar-Gill N, Pham LM, Jarmola A, Budker D, Walsworth RL. Solid-state electronic spin coherence time approaching one second. *Nature communications*. 2013;4:1743.

[123] Mehring M, Mende J. Spin-bus concept of spin quantum computing. *Physical Review A*. 2006;73(5):052303.

[124] Rabl P, Cappellaro P, Dutt MVG, Jiang L, Maze JR, Lukin MD. Strong magnetic coupling between an electronic spin qubit and a mechanical resonator. *Physical Review B*. 2009;79(4):041302.

[125] Bennett S, Yao N, Otterbach J, Zoller P, Rabl P, Lukin M. Phonon-induced spin-spin interactions in diamond nanostructures: application to spin squeezing. *Physical Review Letters*. 2013;110(15):156402.

[126] Twamley J, Barrett SD. Superconducting cavity bus for single nitrogen-vacancy defect centers in diamond. *Physical Review B*. 2010; 81(24):241202.

[127] Kubo Y, Ong FR, Bertet P, Vion D, Jacques V, Zheng D, Dréau A, Roch JF, Auffeves A, Jelezko F, Wrachtrup J, Barthe MF, Bergonzo P, Esteve D. Strong Coupling of a Spin Ensemble to a Superconducting Resonator. *Physical Review Letters*. 2010;105(14):140502.

[128] Kubo Y, Grezes C, Dewes A, Umeda T, Isoya J, Sumiya H, Morishita N, Abe H, Onoda S, Ohshima T, et al. Hybrid quantum circuit with a superconducting qubit coupled to a spin ensemble. *Physical review letters*. 2011;107(22):220501.

[129] Togan E, Chu Y, Trifonov A, Jiang L, Maze J, Childress L, Dutt MG, Sørensen AS, Hemmer P, Zibrov A, et al. Quantum entanglement between an optical photon and a solid-state spin qubit. *Nature*. 2010;466(7307):730–734.

[130] Englund D, Shields B, Rivoire K, Hatami F, Vuckovic J, Park H, Lukin MD. Deterministic coupling of a single nitrogen vacancy center to a photonic crystal cavity. *Nano letters*. 2010;10(10):3922–3926.

[131] Faraon A, Santori C, Huang Z, Acosta VM, Beausoleil RG. Coupling of nitrogen-vacancy centers to photonic crystal cavities in monocrystalline diamond. *Physical review letters*. 2012;109(3):033604.

[132] Toyli DM, Weis CD, Fuchs GD, Schenkel T, Awschalom DD. Chip-scale nanofabrication of single spins and spin arrays in diamond. *Nano Letters*. 2010;10(8):3168–3172.

[133] Staudacher T, Ziem F, Häussler L, Stöhr R, Steinert S, Reinhard F, Scharpf J, Denisenko A, Wrachtrup J. Enhancing the spin properties of shallow implanted nitrogen vacancy centers in diamond by epitaxial overgrowth. *Applied Physics*

Letters. 2012;101(21):212401.

[134] Wildanger D, Maze JR, Hell SW. Diffraction Unlimited All-Optical Recording of Electron Spin Resonances. *Phys Rev Lett.* 2011;107(1):017601.

[135] Meijer J, Burchard B, Domhan M, CWittmann, TGaebel, IPopa, Jelezko F, Wrachtrup J. Generation of single colour centers by focussed nitrogen implantation. *Appl Phys Lett.* 2005;87.

[136] Pezzagna S, Rogalla D, Becker HW, Jakobi I, Dolde F, Naydenov B, Wrachtrup J, Jelezko F, Trautmann C, Meijer J. Creation of colour centres in diamond by collimated ion-implantation through nano-channels in mica. *Phys Status Solidi A.* 2011;208(9):2017–2022.

[137] Ofori-Okai BK, Pezzagna S, Chang K, Loretz M, Schirhagl R, Tao Y, Moores B, Groot-Berning K, Meijer J, Degen C. Spin properties of very shallow nitrogen vacancy defects in diamond. *Physical Review B.* 2012;86(8):081406.

[138] Singer K. Deterministic ion implantation using an ion trap. 2011. Private communication.

[139] Rosskopf T, Dussaux A, Ohashi K, Loretz M, Schirhagl R, Watanabe H, Shikata S, Itoh K, Degen C. Investigation of Surface Magnetic Noise by Shallow Spins in Diamond. *Physical Review Letters.* 2014;112(14):147602.

[140] Rittweger E, Wildanger D, Hell SW. Far-field fluorescence nanoscopy of diamond color centers by ground state depletion. *EPL.* 2009;86(1).

[141] Jakobi I. The nitrogen-vacancy defect center in internal and external fields. Master's thesis, 3. Physikailsche Institut, Universitt Stuttgart. 2012.

[142] Ohno K, Joseph Heremans F, Bassett LC, Myers BA, Toyli DM, Bleszynski Jayich AC, Palmstrøm CJ, Awschalom DD. Engineering shallow spins in diamond with nitrogen delta-doping. *Applied Physics Letters.* 2012; 101(8):082413–082413–5.

[143] Yamamoto T, Umeda T, Watanabe K, Onoda S, Markham ML, Twitchen DJ, Naydenov B, McGuinness LP, Teraji T, Koizumi S, Dolde F, Fedder H, Honert J, Wrachtrup J, Ohshima T, Jelezko F, Isoya J. Extending spin coherence times of diamond qubits by high-temperature annealing. *Physical Review B.* 2013;88(7):075206.

[144] Zeigler JF. *Stopping range of ions in matter.* 2008. `http://www.srim.org/`.

[145] Pezzagna S, Wildanger D, Mazarov P, Wieck AD, Sarov Y, Rangelow I, Naydenov B, Jelezko F, Hell SW, Meijer J. Nanoscale Engineering and Optical Addressing of Single Spins in Diamond. *Small.* 2010;6(19):2117–2121.

[146] Naydenov B, Reinhard F, Lämmle A, Richter V, Kalish R, D'Haenens-Johansson UFS, Newton M, Jelezko F, Wrachtrup J. Increasing the coherence time of single electron spins in diamond by high temperature annealing. *Applied Physics Letters.* 2010;97(24):242511.

[147] Yamamoto T, Müller C, McGuinness LP, Teraji T, Naydenov B, Onoda S, Ohshima T, Wrachtrup J, Jelezko F, Isoya J. Strongly coupled diamond spin qubits by molecular nitrogen implantation. *Physical Review B.* 2013; 88(20):201201.

[148] Dolde F. Functional micro structures to control single spins. diploma thesis, Universität Stuttgart; 3. Physikalisches Institut. 2009.

[149] Fukui T, Doi Y, Miyazaki T, Miyamoto Y, Kato H, Matsumoto T, Makino T, Yamasaki S, Morimoto R, Tokuda N, et al. Perfect selective alignment of nitrogen-vacancy centers in diamond. *Applied Physics Express*. 2014; 7(5):055201.

[150] Lesik M, Tetienne JP, Tallaire A, Achard J, Mille V, Gicquel A, Roch JF, Jacques V. Perfect preferential orientation of nitrogen-vacancy defects in a synthetic diamond sample. *arXiv preprint arXiv:14012795*. 2014;.

[151] Neumann P, Kolesov R, Naydenov B, Beck J, Rempp F, Steiner M, Jacques V, Balasubramanian G, Markham ML, Twitchen DJ, Pezzagna S, Meijer J, Twamley J, Jelezko F, Wrachtrup J. Quantum register based on coupled electron spins in a room-temperature solid. *NATURE PHYSICS*. 2010; 6(4):249–253.

[152] Neumann P, Kolesov R, Naydenov B, Beck J, Rempp F, Steiner M, Jacques V, Balasubramanian G, Markham ML, Twitchen DJ, Pezzagna S, Meijer J, Twamley J, Jelezko F, Wrachtrup J. Quantum register based on coupled electron spins in a room-temperature solid. *Nature Physics*. 2010;6(4):249–253.

[153] Zaiser S. Robust storage of quantum information using single nuclear spins. Master's thesis, 3. Physikailsche Institut, Universitt Stuttgart. 2012.

[154] Mehring M, Mende J, Scherer W. Entanglement between an electron and a nuclear spin 1/2. *Physical Review Letters*. 2003;90(15):153001.

[155] Vedral V, Plenio MB, Rippin MA, Knight PL. Quantifying Entanglement. *Phys Rev Lett*. 1997;78:2275–2279.

[156] Brown RH, Twiss R. Correlation between photons in two coherent beams of light. *Nature*. 1956;177(4497):27–29.

[157] Dolde F, Bergholm V, Wang Y, Jakobi I, Pezzagna S, Meijer J, Neumann P, Schulte-Herbrueggen T, Biamonte J, Wrachtrup J. High fidelity spin entanglement using optimal control. 2013.

[158] Stanwix PL, Pham LM, Maze JR, Le Sage D, Yeung TK, Cappellaro P, Hemmer PR, Yacoby A, Lukin MD, Walsworth RL. Coherence of nitrogen-vacancy electronic spin ensembles in diamond. *Phys Rev B*. 2010; 82(20):201201.

[159] Schirhagl R, Chang K, Loretz M, Degen CL. Nitrogen-Vacancy Centers in Diamond: Nanoscale Sensors for Physics and Biology. *Annual review of physical chemistry*. 2013;.

[160] Vandersypen LMK, Chuang IL. NMR techniques for quantum control and computation. *Rev Mod Phys*. 2005;76:1037–1069.

[161] Blatt R, Wineland D. Entangled States of Trapped Atomic Ions. *Nature*. 2008;453:1008–1015.

[162] Bloch I, Dalibard J, Zwerger W. Many-body physics with ultracold gases. *Rev Mod Phys*. 2008;80:885–964.

[163] Yamamoto T, Pashkin YA, Astafiev O, Nakamura Y, Tsai JS. Demonstration of Conditional Gate Operation Using Superconducting Charge Qubits. *Nature*. 2003;425:941–944.

[164] DiCarlo L, Chow JM, Gambetta JM, Bishop LS, Johnson BR, Schuster DI, Majer J, Blais A, Frunzio L, Girvin SM, Schoelkopf RJ. Demonstration of

Two-Qubit Algorithms with a Superconducting Quantum Processor. *Nature*. 2009;460:240–244.

[165] Clarke J, Wilhelm FK. Superconducting quantum bits. *Nature (London)*. 2008;453:1031–1042.

[166] Nielsen NC, Kehlet C, Glaser SJ, Khaneja N. *Encyclopedia of Nuclear Magnetic Resonance*, chap. Optimal Control Methods in NMR Spectroscopy. Wiley. 2010;.

[167] Cappellaro P, Viola L, Ramanathan C. Coherent-state transfer via highly mixed quantum spin chains. *Phys Rev A*. 2011;83:032304.

[168] Du J, Xu N, Peng X, Wang P, Wu S, Lu D. NMR implementation of a molecular hydrogen quantum simulation with adiabatic state preparation. *Physical review letters*. 2010;104(3):030502.

[169] Wang Y, Dolde F, Babbush R, Whitfield J, Bergholm V, Yang S, Jakobi I, Neumann P, Aspuru-Guzik A, Biamonte J, Jörg W. Quantum Simulation of Helium Hydride in a Solid-State Spin Register. *submited*. 2014;.

[170] Pla JJ, Tan KY, Dehollain JP, Lim WH, Morton JJL, Zwanenburg FA, Jamieson DN, Dzurak AS, Morello A. High-fidelity readout and control of a nuclear spin qubit in silicon. *Nature*. 2013;496(7445):334–338.

[171] Yin C, Rancic M, de Boo GG, Stavrias N, McCallum JC, Sellars MJ, Rogge S. Optical addressing of an individual erbium ion in silicon. *Nature*. 2013; 497(7447):91–94.

[172] Le Gall C, Brunetti A, Boukari H, Besombes L. Optical Stark Effect and Dressed Exciton States in a Mn-Doped CdTe Quantum Dot. *Physical Review Letters*. 2011;107(5):057401.

[173] Weber JR, Koehl WF, Varley JB, Janotti A, Buckley BB, Walle CGVd, Awschalom DD. Defects in SiC for quantum computing. *Applied Physics Letters*. 2011;109(10):102417.

[174] Yang S. Long T_2 at 4K. 2014. Private communication.

[175] Huang P, Kong X, Zhao N, Shi F, Wang P, Rong X, Liu RB, Du J. Observation of an anomalous decoherence effect in a quantum bath at room temperature. *NATURE COMMUNICATIONS*. 2011;2.

List of Figures

Publications relevant to this work

Parts of this work has been published in the following articles:

- Dolde, F, Doherty, MW, Michl, J, Jakobi, I, Naydenov, B, Pezzagna, S, Meijer, J, Neumann, P, Jelezko, F, Manson, NB and Wrachtrup, J.
  Nanoscale Detection of a Single Fundamental Charge in Ambient Conditions Using the NV- Center in Diamond
  PHYSICAL REVIEW LETTERS **112** 9 097603 (2014)
  DOI:10.1103/PhysRevLett.112.097603

- Dolde, F, Bergholm, V, Wang, Y, Jakobi, I, Naydenov, B, Pezzagna, S, Meijer, J, Jelezko, F, Neumann, P, Schulte-Herbruggen, T, Biamonte, J and Wrachtrup, J.
  High-fidelity spin entanglement using optimal control
  NATURE COMMUNICATIONS **5** 3371 (2014)
  DOI:10.1038/ncomms4371

- Laraoui, A, Dolde, F, Burk, C, Reinhard, F, Wrachtrup, J and Meriles, CA.
  High-resolution correlation spectroscopy of C-13 spins near a nitrogen-vacancy centre in diamond
  NATURE COMMUNICATIONS **4** 1651 (2013)
  DOI:10.1038/ncomms2685

- Dolde, F, Jakobi, I, Naydenov, B, Zhao, N, Pezzagna, S, Trautmann, C, Meijer, J, Neumann, P, Jelezko, F and Wrachtrup, J.
  Room-temperature entanglement between single defect spins in diamond
  NATURE PHYSICS **9** 139-143 (2013)
  DOI:10.1038/nphys2545

- Pezzagna, S, Rogalla, D, Becker, HW, Jakobi, I, Dolde, F, Naydenov, B, Wrachtrup, J, Jelezko, F, Trautmann, C and Meijer, J.
  Creation of colour centres in diamond by collimated ion-implantation through nano-channels in mica
  PHYSICA STATUS SOLIDI A-APPLICATIONS AND MATERIALS SCIENCE **208** 2017-2022 (2011)
  DOI:10.1002/pssa.201100455

- Dolde, F, Fedder, H, Doherty, MW, Noebauer, T, Rempp, F, Balasubramanian, G, Wolf, T, Reinhard, F, Hollenberg, LCL, Jelezko, F and Wrachtrup, J.
  Electric-field sensing using single diamond spins
  NATURE PHYSICS **7** 459-463 (2011)
  DOI:10.1038/NPHYS1969

- Naydenov, B, <u>Dolde, F</u>, Hall, LT, Shin, C, Fedder, H, Hollenberg, LCL, Jelezko, F and Wrachtrup, J.
  Dynamical decoupling of a single-electron spin at room temperature
  PHYSICAL REVIEW B **83** 081201 (2011)
  DOI:10.1103/PhysRevB.83.081201

Acknowledgments

I want to thank Prof. Jörg Wrachtrup for giving me this amazing opportunity to work at this wonderful institute and topic.

Prof. Harald Giessen I would like to acknowledge for being my co-examinor for this thesis and Prof. Günter Wunner for chairing my defense.

Thanks to every member of the 3. Institut for the excellent working atmosphere. Especially for all the useful discussion and their support I want to acknowledge Philipp Neumann, Ingmar Jacobi, Julia Michl, Christian Burk, Gerald Waldherr, Thorsten Rendler, Sebastian Zaiser, Roman Kolesov, Rainer Stöhr and Claudia Unger. Without them, this work could never have succeeded.

This work was a team effort, therefore I would like to thank not only all the members of the 3. Institute, but also all the external collaborators who made this work possible.

Foremost I would like to thank Boris Naydenov and Fedor Jelezko for all their support and discussion while they were still in Stuttgart and continuing to support and inspire me after starting their exciting work in Ulm.

For their help in theory and helping me to gain an understand of sensing, dynamical decoupling and the electric field Hamiltonian, I am indebted to the Australian connection, namely Marcus Doherty and Liam Hall. Without their help, support and patience, this work would not be what it is now.

For their support in sample preparation and the implantation of NV centers, I would like to acknowledge Jan Meijer, Sébastien Pezzagna and Christina Trautmann. Without them, there would be no samples and therefore no new and exciting experiments.

Thanks to Tobias Nöbauer for conduction the electric field measurements with me.

I want to thank Phil Hemmer for support, ideas and small tricks he showed me making my work way easier. Although the discussions with him were always productive and helped me expand my understanding of physics.